A Miniature Mobile Robot for Precise and Stable Access to the Beating Heart

Nicholas A. Patronik

CMU-RI-TR-08-13

Submitted in partial fulfillment of the requirements for the degree of Doctor of Philosophy in Robotics.

The Robotics Institute
Carnegie Mellon University
Pittsburgh, Pennsylvania 15213

May 8, 2008

Thesis Committee:
Cameron Riviere, Chair
Marco Zenati
Metin Sitti
Russell Taylor, Johns Hopkins University

Abstract

For a wide array of procedures, cardiologists and cardiac surgeons currently compete with one another to provide minimally invasive therapy with the goal of decreasing associated morbidity while providing quality treatment. Although the thoracoscopic techniques used by cardiac surgeons greatly reduce morbidity compared to open surgery, the percutaneous transvenous approaches favored by cardiologists are less invasive and can be performed on an out-patient basis. In light of this convergence, it is reasonable to consider the development of hybrid instrumentation and techniques that address the goals of both cardiologists and cardiac surgeons.

In this thesis, we propose that the development of a miniature mobile robot (HeartLander) that adheres to and traverses the epicardium will provide a tool for precise and stable interaction with the beating heart. The ability of the robot to adhere to the epicardium obviates the need for cardiopulmonary bypass or mechanical stabilization, while the mobility overcomes access limitations that currently limit thoracoscopic techniques. Additionally, the ability of HeartLander to be deployed to the apex of the heart through a percutaneous subxiphoid approach may enable cardiac surgeons to provide out-patient procedures.

To demonstrate the utility of HeartLander, we focus on a subset three intrapericardial therapies that require precise and stable treatments at multiple sites on the surface of the heart: myocardial injection of regenerative materials, epicardial lead placement, and epicardial ablation. To facilitate these clinical tasks, HeartLander must provide access over the entire epicardium, demonstrate precise positioning to selected targets, and ensure safe and stable interaction with the surface of the beating heart. To minimize the associated morbidity, the robot must achieve these goals with the chest closed, the pericardium intact, and the heart beating. Through a series of closed-chest, beating-heart porcine studies, HeartLander demonstrated navigation over the entire circumference of the heart, the acquisition of targets within 1.0 mm, and stability with residual motion less than 1.0 mm.

The novel HeartLander paradigm combines the tracking techniques, anatomical models, and minimal access morbidity of transvenous procedures with the epicardial access and fine control of thoracoscopic techniques. A hybrid device of this nature may provide advantages over current approaches within the field of cardiac care for certain procedures.

Acknowledgements

First and foremost, I would like to thank my advisor Cameron Riviere for his guidance and support throughout the completion of my dissertation. I have enjoyed bringing his vision of HeartLander to life over the past six years. I would also like to thank my committee members: Marco Zenati, for his direction of the project and visionary clinical perspective; Metin Sitti, for his expertise in micro-scale sensors and actuators; and Russ Taylor, for his grand vision of computer integrated surgery that has had a global impact. I would like to thank several individuals from the Medical Instrumentation Lab: Wei Tech Ang, for his mentoring during the early years of my thesis; David Choi, for his collaboration as a fellow student; Rob McLauglin, for his technical guidance; Eric Haas, Ye Gang, Si Yi Khoo, Chee Kiat Ng, Faezeh Razjouyan, Harsha Tummala, and Peter Allen, for their outstanding technical contributions to the HeartLander project as undergraduate students. I also thank Takeyoshi Ota from the University of Pittsburgh Medical Center, who devoted many hours to the preclinical animal testing of the HeartLander system and provided valuable feedback to enhance its usability.

For funding support, I thank the U.S. National Institutes of Health (grant R01 HL078839), the National Science Foundation Engineering Research Center for Computer-Integrated Surgical Systems (grant EEC-9731748), and the NASA Graduate Student Researchers Program (fellowship NNG05GL63H).

I would like to thank all of my friends from the Robotics Institute, particularly the residents and honorary residents of 517 St. James Place, who helped me to make the right decision to enroll in the RI doctoral program. I also thank my family, particularly my parents Nick and Colleen, my brothers Matt and Greg, and my grandparents. Lastly, I thank Kate, for her incredible support, patience, and cheerfulness throughout multiple rounds of document revisions, practice talks, and all manner of difficulties.

Contents

List of Figures

List of Tables

Chapter 1

Introduction

1.1 The Convergence of Cardiac Care

Over the past 30 years, the field of cardiac care has progressed along two distinct paths in the exploration of decreasing associated morbidity while providing quality treatment. The main challenges presented by this goal are to access the heart without opening the chest, and to operate upon the heart while it remains beating. In the fields of cardiology, electrophysiology, and interventional radiology, physicians access the internal (endocardial) structures of the heart using thin catheter-based tools that are inserted into the systemic vasculature through small percutaneous incisions. In the absence of direct visualization, the physicians rely on tracked tools, anatomical models, and non-invasive imaging modalities to reason about their interactions with the heart during these transvenous procedures. The field of cardiac surgery has moved toward thoracoscopic procedures, in which conventional surgery on the external structures of the heart is achieved with the chest closed using long cylindrical tools that are inserted into the body through small intercostal incisions. Similar to open procedures, surgeons rely on visualization of the operative site and surgical instruments using 3-D thoracoscopic cameras inserted into the body.

For a wide array of procedures, cardiologists and cardiac surgeons currently compete with one another to provide minimally invasive therapy using alternative transvenous and thoracoscopic techniques. Although thoracoscopic techniques greatly reduce the procedural morbidity as compared to open surgery, transvenous approaches incur even less morbidity and can be performed on an out-patient basis. Accordingly, transvenous procedures have become the preferred technique for many cardiac therapies [1], [2], [3]. As the popularity of transvenous procedures has increased, the surgical community has begun to question the quality of transvenous outcomes as compared to surgical alternatives [4], [5], [6]. For any given procedure, a patient must consider both the quality of the outcome and the associated morbidity in comparing the transvenous and thoracoscopic alternatives. To complicate matters, the fields of cardiology and cardiac surgery often do not reach a consensus on the evaluation of outcomes from alternative techniques. While the financial structure of the healthcare industry in the United States is such that cardiologists and cardiac surgeons view one another as rivals, their goals of improving cardiac care while reducing associated morbidity using new technologies are similar. In light of this emerging convergence, it is reasonable to consider the development of hybrid instrumentation and techniques that address the goals of both cardiologists and cardiac surgeons [7], [8].

1.2 Thesis Statement

In this thesis, we propose that the development of a miniature mobile robot (HeartLander) that adheres to and traverses the epicardium will provide a tool for precise and stable interaction with the beating heart. The ability of the robot to adhere to the epicardial surface of the heart obviates the need for cardiopulmonary bypass or mechanical stabilization, while the mobility overcomes access limitations that currently limit thoracoscopic techniques. Additionally, the ability of HeartLander to be deployed to the apex of the heart through a percutaneous subxiphoid approach may enable cardiac surgeons to provide out-patient procedures. The novel HeartLander paradigm combines the tracking techniques, anatomical models, and minimal access morbidity of transvenous procedures with the epicardial access and fine control of thoracoscopic techniques. A hybrid device of this nature may provide advantages over current approaches within the field of cardiac care for certain procedures.

To demonstrate the utility of HeartLander, we focus on a subset three intrapericardial therapies that require precise and stable treatments at multiple sites on the surface of the heart: myocardial injection of regenerative materials, epicardial lead placement, and epicardial ablation. To facilitate these clinical tasks, HeartLander must provide access over the entire epicardium,

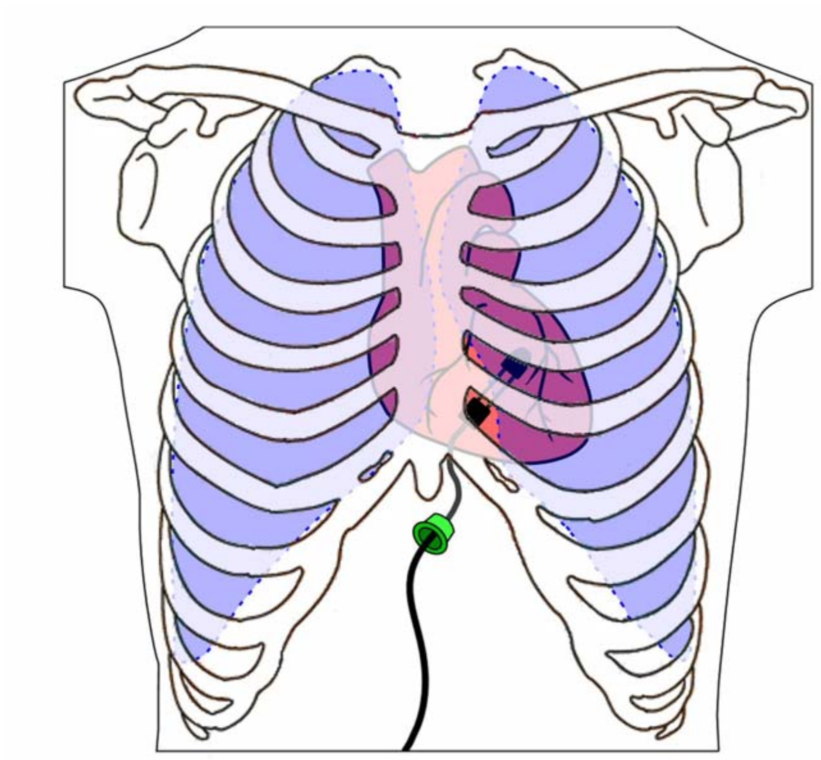

Figure 1.1: Illustration of HeartLander concept (the ribs and lungs are shown transparent, while the skin and pericardium are not shown). The robot is inserted through an incision below the sternum, adheres to the epicardial surface of the heart using suction, and provides access to any specified region on the heart surface.

demonstrate precise positioning to selected targets, and ensure safe and stable interaction with the surface of the beating heart. To minimize the associated morbidity, the robot must achieve these goals with the chest closed, the pericardium intact, and the heart beating. Through a series of closed-chest, beating-heart porcine studies, HeartLander demonstrated navigation over the entire circumference of the heart, the acquisition of targets within 1.0 mm, and stability with residual motion less than 1.0 mm.

1.3 The HeartLander Concept

The organ-mounted paradigm of HeartLander addresses three limitations that currently hinder the adoption of thoracoscopic techniques for cardiac procedure. An illustration of the HeartLander approach can be seen in Figure 1.1. The robot adheres to the epicardial surface of the heart using vacuum pressure, which has been demonstrated to be safe in the case of mechanical cardiac stabilizers [9], [10]. By attaching directly to the epicardium, the robot is located in the moving reference frame of the beating heart, thus passively compensating for both heartbeat and respiratory motion. The robot is also equipped with actuators and a tracking sensor for semi-autonomous navigation to specified targets. Locomotion enables HeartLander to reach areas of the epicardium that are difficult to access using conventional intercostal thoracoscopy, such as the posterior wall of the left ventricle [11]. Mobility also allows the surgeon to radically change operative fields from a single insertion.

The locomotive capabilities of HeartLander also allow the insertion site of the robot to be independent of the operative site for the procedure. Accordingly, HeartLander is deployed though a percutaneous incision below the xiphoid process of the sternum. Unlike an intercostal approach, this subxiphoid approach provides access to the heart without breaching the space occupied by the lungs (shown in light gray in Figure 1.1), thus obviating differential ventilation and lung deflation [12], [13]. Therefore, the insertion of HeartLander does not require general anesthesia, and in principle could be performed on an outpatient basis.

Like an endoscope, HeartLander has a working channel through which a flexible therapeutic device can be inserted and applied to the heart. We have used HeartLander to successfully deploy several commercial therapeutic devices to beating porcine (pig) hearts, including pacing leads, myocardial injection needles, and ablation catheters [14], [15], [16].

1.4 Contributions

- **Development of a mobile robot to access the entire epicardium**. The miniature size of the HeartLander crawler permits it to travel beneath the intact pericardium to reach any location on the surface of the beating heart through a small subxiphoid percutaneous and pericardial incisions. The navigation system has demonstrated locomotion to points around the entire circumference of the heart. Thus, HeartLander provides total epicardial access thorough a minimally invasive approach.
- **Development of a positioning system with high accuracy on the beating heart**. The drive-wire mechanism, suction-based prehension, and real-time filtering allow HeartLander to act as a manipulator for reaching a series of target locations in distal regions on the beating heart.

The accuracy of the positioning system has demonstrated positioning errors less than 1.0 mm on the beating heart with the chest closed.

- **Platform stability beyond the current capabilities of mechanical stabilizers**. The miniature size and prehension capabilities of HeartLander allow the robot to remain fixed on the surface of the heart without being displaced by the shearing motion of the pericardium relative to the heart. The robot has demonstrated resultant maximum 3-D displacement of less than 1.0 mm over a period of 30 s around the entire circumference of the heart. This resultant drift is less than that provided by commercial mechanical stabilizers currently used in beating-heart surgery.
- **Application of pure pursuit to a new mobile robot domain**. The pure pursuit path tracking algorithm has been adapted from use in wheeled mobile robots to the wire-driven HeartLander crawler traveling on the beating heart. The incremental goal steps generated by the tracking algorithm were fed to the inverse kinematics of the wire actuation for step planning to the target location along the desired path.
- **Development of a novel method for generating a registered surface mode**l. A surface tracing methodology was developed to provide a still 3-D reconstruction of the beating heart surface through a subxiphoid incision. This model was automatically registered within the tracking system used by the robot during navigation. The technique takes the surgeon and engineer less than 30 minutes to complete, and required no preoperative or intraoperative radiation-based imaging.
- **The design and construction of three generations of crawlers**. Three distinct generations of crawlers have been developed and tested in vivo. Each crawler was built to overcome difficulties encountered by its predecessor, improving epicardial access and requiring less invasive approaches. The third generation crawler is capable of accessing the entire epicardial surface of the beating heart through a subxiphoid percutaneous incision.
- **Demonstration of sample therapy administration from robot platform**. The remote injection system permitted the surgeon to inject dye into the myocardium through the working channel of the robot. Dye was used to simulate regenerative material injection, and to validate the location of the robot on the heart during target acquisition trials. Additionally, a commercial pacing lead and ablation catheter designed for transvenous application were successfully applied to the epicardium using HeartLander through a subxiphoid percutaneous incision. In combination with the navigation capabilities of HeartLander, this represents a highly accurate therapeutic system.

1.5 Organization

Chapter 2 provides background for the thesis by describing the state of the art in minimally invasive cardiac surgery, and providing a literature review on miniature mobile robots related to HeartLander. Chapter 3 describes in detail the intrapericardial environment and therapies that are initially envisioned for administration from HeartLander. In Chapters 4 and 5, the design of the robot and control system are motivated and described. Chapter 6 presents the experimental results from a series of porcine studies used to evaluate the HeartLander system. Chapter 7 describes the preclinical testing of three intrapericardial therapeutic end effectors and two diagnostic sensors deployed from HeartLander in preclinical feasibility testing. Finally, Chapter 8 concludes this thesis and suggests future work.

Chapter 2

Background

The state of the art in thoracoscopic technology is the teleoperated robotic system, a commercial version of which is gaining acceptance throughout the surgical community. Although robotic assistance greatly improves upon conventional endoscopy, there exist three main limitations with regard to cardiac surgery: required stabilization, access limitations, and associated morbidity. HeartLander was designed specifically to address these limitations. This chapter describes in greater detail the current solutions to stabilize the interaction between the surgical tools and the beating heart. Lastly, a literature review of two classes of mobile robots that are related to HeartLander is presented.

2.1 Teleoperated Robotic Surgery

The morbidity associated with general surgery can be greatly reduced using endoscopic surgery, in which long thin tools are passed through a set of incisions to gain access to an operative worksite without requiring an open procedure. Figure 2.1 shows a typical intercostal tool insertion configuration for thoracic endoscopy, known as thoracoscopy. In cardiac surgery, thoracoscopy avoids the trauma of full median sternotomy – cutting the sternum and expanding the ribcage to expose the thoracic cavity – by inserting the tools between the ribs. The state of the art in endo

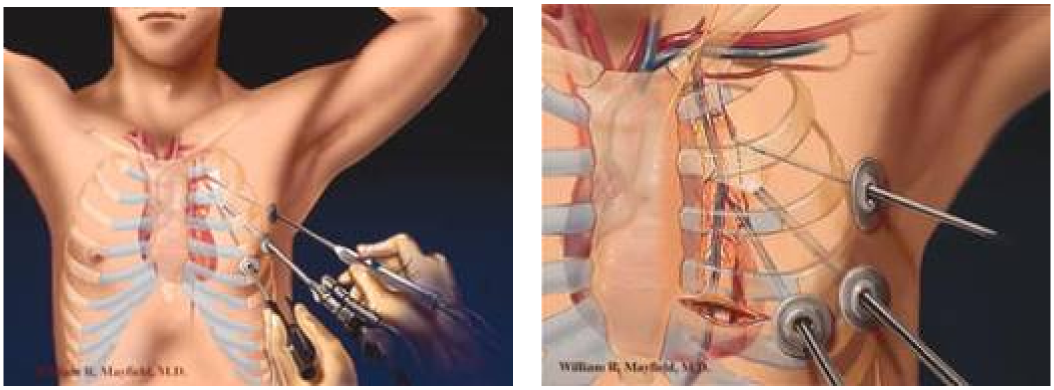

Figure 2.1: (left) Illustration of thoracoscopic cardiac surgery using handheld instrumentation. The two outer shafts – held by the surgeon – are the laparoscopic tools, while the center shaft is the scope. (right) Close up of the access ports and instrumentation. Image reproduced from William R. Mayfield, M.D.

Figure 2.2: The Da Vinci teleoperated robotic manipulator system. Insets show close ups of the input handles (lower right) and the surgical robotic manipulators (upper right). Image reproduced from Medtronic, Minneapolis, MN.

scopy is teleoperated robotic surgery, through which the motions of the surgeon's hands on a set of input devices are mimicked by a set of robotically actuated tools located inside the patient. The surgeon views the motions of the robotic tools through a 3D endoscopic camera, with the view angle displayed as though the surgeon were viewing his or her own hands. In this manner, the surgeon is able to control the robotic tools intuitively. The commercially available da Vinci System (Intuitive Surgical, Mountain View, CA) can be seen in Figure 2.2. These robotic systems improve upon conventional endoscopy by increasing dexterity, restoring hand-eye coordination, and reducing fatigue. Recently, the da Vinci System has been adopted in several surgical procedures, including laparoscopic cholecystectomy and prostatectomy [17], [18]. As compared to urological and general surgery, the adoption of this robotic system in the field of cardiac surgery has fallen behind. I propose that there are three main limitations with the teleoperated endoscopic paradigm that have hindered its adoption in cardiac surgery: required stabilization, access limitations, and associated morbidity. All of these limitations result from the fact that teleoperated robots are an extension of the same endoscopic concept that has existed for almost one hundred years, which is not particularly well suited for operation on the beating heart.

Surgery on the beating heart is highly desirable because research suggests that cardiopulmonary bypass can lead to serious complications [19], [20]. Teleoperated robotic systems require the stabilization of the physical interaction between the surgical tools and the heart surface for safety and accuracy. Although endoscopic mechanical stabilizers can be used to immobilize a small region of the epicardial surface, they add clutter to an already confined workspace, can impair heart function, and exhibit residual motion. Taking a different approach, some researchers are exploring the potential of actuating the surgical tools to move in synchronization with the beating heart surface, thus actively compensating for the physiological motion. Both of these stabilization techniques have drawbacks, which are explored in greater detail in Section 2.2. It has been suggested in the literature that the lack of wider acceptance in cardiac surgery is due to the fact that the system fails to address adequately the issue of organ motion compensation for beating-heart surgery [21].

Additionally, there are several access limitations inherent to robotic thoracoscopy. In order to successfully access the full operative site for a procedure, the surgeon must be sure that tool incisions are appropriately located and that the external arms of the robotic system are positioned such that they will not contact one another during the actuation of the tools. If either of these preparations are not correctly managed, the tools must be retracted from the patient and the problem rectified. Even with a correct initial setup of the robotic system, significantly changing the location of the operative site during the procedure may require additional incisions and reinsertion of the thoracoscopic tools. Meanwhile, distal regions of the heart such as the posterior left ventricle remain difficult to reach at all using this intercostal approach [11].

Lastly, the intercostal approach for the robotic tool insertions requires general anesthesia and the deflation of the left lung in order to access the heart. As can be seen in Figure 1.1, the left lung surrounds the heart and must be bypassed when the endoscopic tools are inserted between the ribs. To avoid accidentally puncturing the lungs with the endoscopic tools, the left lung is deflated so that it lies passively in the posterior of the thoracic cavity. In this manner, the anterior and left-lateral aspects of the heart can be safely accessed through intercostal incisions. The deflation of the left lung requires general endotracheal anesthesia and differential ventilation, which add to the overall morbidity of the procedure and can lead to complications unrelated to the cardiac procedure [22], [23].

2.2 Cardiac Stabilization

Surgery on the beating heart is a major objective in the field because research suggests that cardiopulmonary bypass, which allows the heart to be stopped, may be as harmful as full median sternotomy [19], [20]. Additionally, it has been shown to be highly related with postoperative stroke [24].

The obvious complication in beating heart surgery is that the stationary tools of the surgeon must interact with the moving structures of the heart in a manner that is safe and effective. Accordingly, two methods are being developed to compensate for heartbeat motion during surgical procedures: locally immobilizing the heart surface, and actuating the tools to move with the beating heart surface. These techniques are described in greater detail in the following subsections.

2.2.1 Mechanical Stabilizers

Local mechanical immobilization of the epicardial surface of the heart is the clinical approach generally followed today for beating-heart surgery. Suction-based positioners and stabilizers, such as the Medtronic Starfish™ and Octopus™ (Minneapolis, MN) shown in Figure 2.3, were first developed for open surgical procedures and mounted to retractors. Due to the increasing popularity of thoracoscopy, endoscopic stabilizers such as the Endosmart Endostab™ (Stutensee, Germany) and Medtronic Octopus TE™ (Minneapolis, MN) have been developed that operate with positive pressure or suction, respectively [25], [26]. The resulting forces exerted on the heart, however, can adversely affect its electrophysiological and mechanical performance [27], [28]. Care must be taken in order to avoid hemodynamic impairment or life-threatening arrhythmia [11]. In addition to the clutter and potential adverse side effects, mechanical stabilizers do not completely immobilize the epicardial surface. Lemma et al. found that the residual motion of the coronary arteries ranged from 1.5 to 2.4 mm following stabilization with three commercial suc

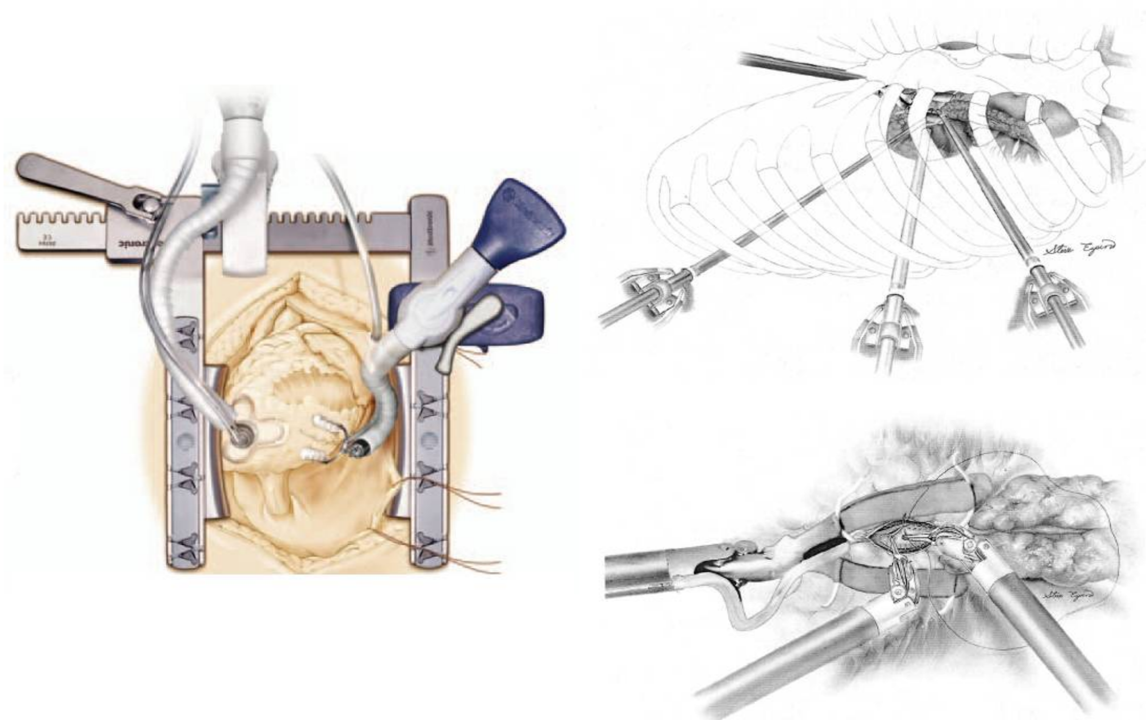

Figure 2.3: Illustration of an open-chest beating-heart surgical field using a Medtronic Starfish™ heart positioner and Medtronic Octopus™ tissue stabilizer to expose and stabilize the operative site on the lateral wall. Image reproduced from Medtronic, Minneapolis, MN.

tion-based mechanical stabilizers from Medtronic, Genzyme, and CTS-Guidant [29]. These authors expressed their concerns that this persistent motion may result in less surgical precision and adversely affect the quality of outcomes. A similar study found that positive pressure stabilizers also exhibit significant residual motions and velocities [30].

In addition to safety and residual motion concerns, it is difficult to expose and stabilize certain regions of the heart. For example, the posterior aspect of the heart is difficult to access, even during open-chest procedures. Typically, the surgeon will grab the apex of the heart with a positioner, and lift the body of the heart out of the mediastinum to expose the posterior aspect. It is often necessary to access this region of the heart because the left ventricle is most severely affected by myocardial infarct and congestive heart failure (Buja and Krueger 2005). More convenient access to the posterior aspect of the heart is certainly one of the major benefits of the HeartLander paradigm.

2.2.2 Active Motion Compensation

As an alternative, several researchers in robot-assisted thoracoscopic surgery are investigating active compensation of heartbeat motion by visually tracking the epicardium and moving the tool tips accordingly [31], [32], [33], but this research problem remains open. The motion of the beating heart is complex. In addition to the challenges of modeling or tracking the heart surface, active compensation requires considerable cost for high-bandwidth actuation to manipulate in at least 3 degrees-of-freedom (DOFs) over a relatively large workspace [31].

2.3 Related Work

Mobile robots have been studied extensively for the last several decades, thus I will limit my discussion herein to mobile robots that are considered to be miniature. One classification scheme for miniature mobile robots is based on the media in which they travel. There has been an abundance of research into miniature mobile robots designed to travel in the air [34], through liquid [35], [36], and on the ground [37], [38]. The two subsets of ground-based miniature mobile robots that are the most akin to HeartLander are those that climb in vertical environments and those that operate within the human body.

2.3.1 Climbing Mobile Robots

There has been relatively little research into the design of miniature climbing robots, as compared to the more traditional environments mentioned above. This may be due to the fact that climbing robots require the miniaturization of the prehension source in addition to the sensors, actuators, and power supply. The most common forms of prehension in larger size climbing mobile robots are magnetism [39], suction [40], [41], [42], and claws or spines [43], [44]. Of these systems, only the tethered robot by Tummala et al. has a relatively small size. Alternatively, the smallest examples of climbing mobile robots all use conventional dry adhesives for prehension. Menon et al. developed two miniature climbing robots that use dry adhesives to adhere to smooth vertical environments [45]. One of these robots uses rotating “legged wheels” with sticky pads, while the other uses sticky treads. Another group of researchers developed a similar miniature climbing robot that also uses wheel-legs with compliant adhesive feet, is self-contained, and can transition between orthogonal surfaces [46]. As the development of gecko-inspired dry adhesives advances, these robots may be able to climb wet or biological surfaces as well as the smooth, dry surfaces on which they are currently tested [47]. HeartLander is unique as compared to these climbing robots in that it travels on a moving biological surface with extreme spatial constraints. In addition to overcoming the environmental difficulties associated with traveling in the human body, the robot must not damage the heart or surrounding structures. The design of HeartLander addresses the traversal of a new substrate material and set of operating constraints within the field of climbing mobile robots.

2.3.2 Medical Mobile Robots

Although there has been some research into mobile robotics for medical applications, the targeted physiological environments are relatively stable. The majority of this research has been focused on navigating through the large intestine using inchworm-like robots [40, 48, 49]. These mobile robots advance the diagnostic scope though the intestine using the active front section, as opposed to the physician pushing the scope from behind. It is hypothesized that this self-propulsion will avoid distending the bowel and creating discomfort, which can happen in conventional colonoscopy. These tubular robots are driven by shape memory alloys [43], pneumatics [48], or cables [40]. They generate traction with the surrounding luminal wall of the intestine using suction [48], graspers [48], spines [43]; and recently there has been some attention toward using microstructures for improving traction [50]. The majority of these robots are tethered, which naturally supplies an access channel for treatment, although some researchers are exploring with wireless options [43]. Although the technical development of these robots has advanced considerably, it has yet to be seen if the clinical advantages will make them a viable alternative in practice.

Another novel application within the digestive system is the diagnostic exploration of the small intestine with miniature passive pill cameras [51], [52]. These wireless devices are propelled through the small intestine by natural peristalsis, and broadcast images to a receiver worn by the patient. Prior to the advent of these devices, visualization of the small intestine was only possible through open surgical techniques, as access using traditional endoscopy is not possible. Although the commercialized products sold today are passive, there is active research into using onboard radio frequency coils and battery powered legs to control the descent of these devices [53], [54].

Recently, a wheeled mobile robot to travel over the abdominal organs has also been developed [55]. This work is unique in that it concentrates on a non-luminal organ, and applies the wheeled robot paradigm in vivo. This group modified a traditional mechanical model for the wheel-soil interaction of passenger vehicles for application to the tissues in the abdomen. This model was used to influence design parameters to generate traction.

Compared to these works, HeartLander has the additional burden of overcoming the motion of the heart and lungs while traveling in an extremely confined space. HeartLander will also integrate the navigation techniques used by traditional autonomous mobile robots in order to effectively position itself the beating heart. The active and passive devices that travel through luminal organs may avoid such considerations, because they are effectively traveling in an environment with one degree of freedom. Within the field of medial mobile robots, HeartLander will introduce the traversal of a new organ with the added task of overcoming and thus passively compensating for considerable organ motion. HeartLander will also apply the traditional navigation paradigm used by autonomous mobile robots to this field.

Chapter 3

The Intrapericardial Environment

The ultimate goal of the HeartLander robotic system is to provide minimally invasive access to the epicardium in a precise and stable manner that will accommodate the administration of a variety of intrapericardial therapies. In order to minimize the associated morbidity, HeartLander must operate with the chest closed, the pericardium intact, and the heart beating. This results in a challenging environment for a mobile robot. The pericardium and surrounding organs create static spatial constraints, while the heartbeat and respiratory motions generate high dynamic forces. This chapter gives a brief description of the physiology of the intrapericardial cavity, and several potential therapies envisioned for administration from HeartLander.

3.1 Intrapericardial Physiology

3.1.1 Cardiac Anatomy

The heart lies at an oblique angle within the central lower section of the thoracic cavity known as the mediastinum, and is enclosed by the pericardium. Although the heart moves within the mediastinum during beating, it is surrounded by structures on all sides. In the coronal plane of the human body the heart is enclosed by the lungs, the diaphragm, and the great vessel insertions (Figure 3.1). In the axial plane, it is bounded by the lungs, the esophagus and spinal column, and the sternum (Figure 3.2). Accordingly, there is no free space around the heart in situ.

The function of the heart is to pump blood throughout the cardiovascular system for the distribution of gases, nutrients, and wastes within the body. An illustration of the pathway of the blood through the heart can be seen in Figure 3.3. The heart is made up of four chambers that form two independent pumps ("left" and "right") in series. Each pump has a thinner-walled atrium that acts as a holding area for the blood, and a thicker-walled ventricle for ejecting the blood away from the heart. The atria form the superior portion of the heart known as the base. The ventricles are located directly inferior to their corresponding atria, and form the apex of the heart. Deoxygenated blood from the body enters the right atrium, and is pumped out to the lungs by the right ventricle where it is reoxygenated. The reoxygenated blood then enters the left atrium, and is pumped out to the body by the left ventricle through the aorta. The plumbing of the pumps is such that they are independent, and blood flows only in one direction. The electrical conduction of the heart coordinates the right and left atria to pump synchronously, followed by the synchronous ejection of right and left ventricles.

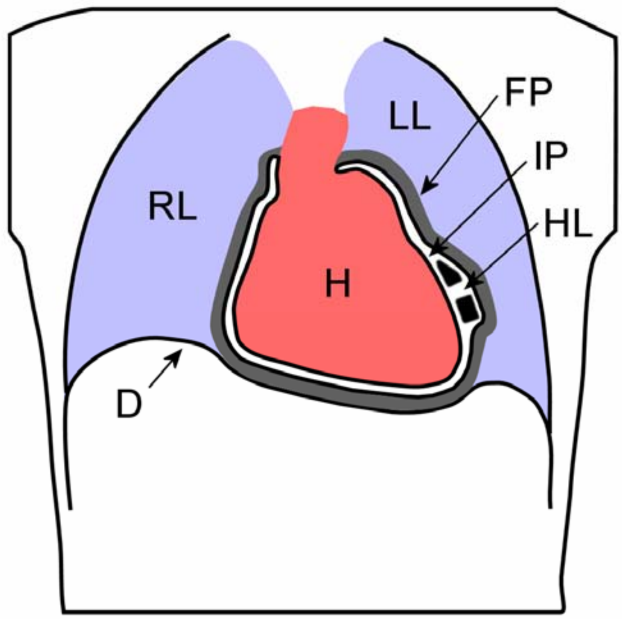

Figure 3.1: Illustration of HeartLander (HL) in the intrapericardial space (IP) in the coronal view. The surrounding organs include the heart (H), right lung (RL), left lung (LL), diaphragm (D), and the fibrous pericardium (FP). The sizes of the intrapericardial space (shown in white) and fibrous pericardium (dark gray) have been greatly exaggerated for clarity. The robot tether is not shown.

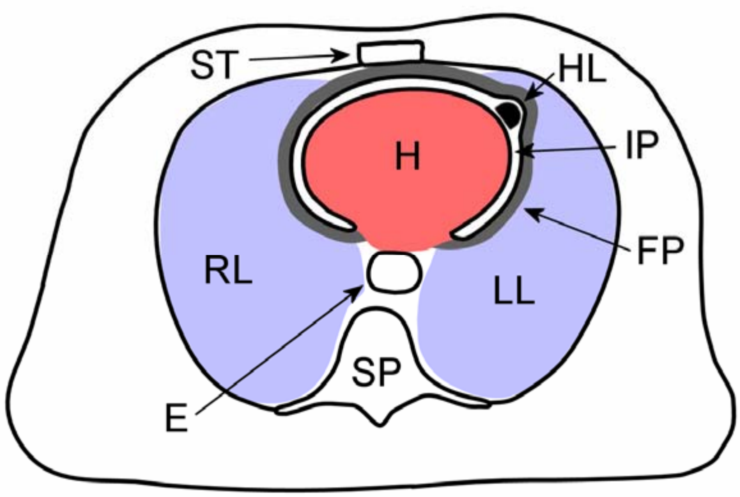

Figure 3.2: Illustration of HeartLander (HL) in the intrapericardial space (IP) in the axial view. The surrounding organs include the heart (H), right lung (RL), left lung (LL), fibrous pericardium (FP), sternum (ST), spinal column (SP), and esophagus (E). The sizes of the intrapericardial space (shown in white) and fibrous pericardium (dark gray) have been greatly exaggerated for clarity. The robot tether is not shown.

The external surface of the heart is grossly convex, and forms a single continuous space within the pericardium. Although the boundaries between the chambers form grooves or sulci, the gross shape of the heart remains convex over the heartbeat cycle. The only rigid attachments to the heart are the great vessel insertions located at the base, allowing the remainder of the heart to move during the heartbeat. Thus, the external surface of the heart beneath the great vessels forms a single continuous convex volume within the pericardium. This geometry is conducive to traversal with a mobile robot because it lacks surface features in which the robot might become stuck (i.e. "obstacles"), and navigation boundaries (i.e. "walls"). Accordingly, the majority of the surface of the heart can be reached from trajectories originating at the apex of the heart. This fact can be seen in Figure 3.4. The anterior surfaces of the right atrium, right ventricle, and left ventricle are directly accessible from trajectories that originate at the apex and move over the anterior aspect of the heart. Meanwhile, the posterior surfaces of all four chambers are accessible from trajectories beginning at the apex that span the posterior aspect of the heart. By placing HeartLander on the apex of the heart through a subxiphoid approach, the robot has access to the epicardial surface of all four chambers of the heart.

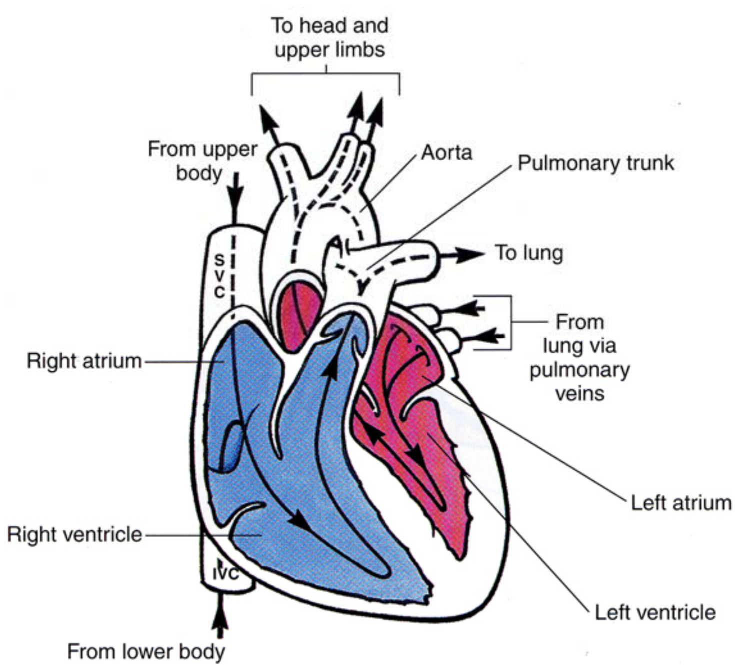

Figure 3.3: Illustration of the blood flow through the four chambers of the heart. The deoxygenated blood (blue) enters the right atrium from the body through the vena cava. It is then pumped out of the heart to the lungs through the pulmonary arteries to be reoxygenated. The reoxygenated blood (red) then enters the right ventricle through the pulmonary veins. Lastly, the reoxygenated blood is ejected from the heart to the body through the aorta. Image reproduced from [56].

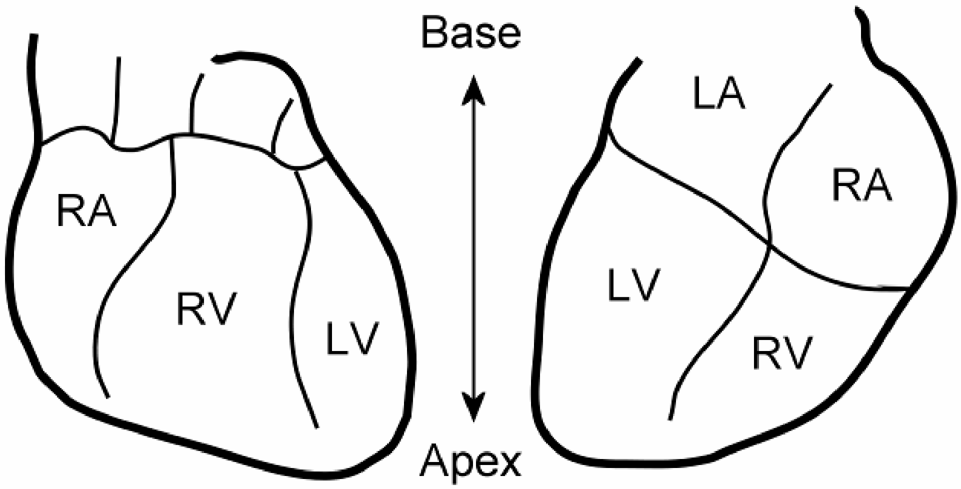

Figure 3.4: Illustration of the locations of the heart chambers in the (left) anterior view and (right) posterior view. The four chambers of the heart are the right ventricle (RV), right atrium (RA), left ventricle (LV), and left atrium (LA).

3.1.2 Pericardial Anatomy

The heart is enclosed within the mediastinum by a two-layered sac called the pericardium, which stabilizes the location of the heart, restrains the volume during filling, and provides friction relief. The thick, fibrous outer layer of the pericardium stabilizes and restrains the heart. It is attached superiorly to the great vessels of the heart, inferiorly to the diaphragm, anteriorly to the sternum, and posteriorly to the esophagus and vertebral column. While the fibrous pericardium is not rigidly attached to the lungs, close contact with pleural cavities is maintained by cohesion of a thin layer of liquid between them.

Friction between the beating heart and the stationary, fibrous pericardium is relieved by the thin, serous inner layer of the pericardium, which lined with epithelial cells and is thus smooth and moist. This layer of the pericardium reflects back over the outside of the heart, and attaches to the myocardium – the thick muscular layer of the heart – to form the epicardium (Figure 3.1). In this manner, the serous layer of the pericardium and epicardium forms a cavity known as the intrapericardial space. This is the space in which HeartLander travels. The intrapericardial space is naturally filled with a film of 20 to 50 mL of serous pericardial fluid, which acts as a lubricant for the heart. This fluid has a consistency similar to blood serum, and a density similar to water [57], [58]. The intrapericardial space, therefore, exists only as a virtual space that is less than 1 mm in thickness [59]. The absence of natural clearance between the epicardium and pericardium means that HeartLander must generate its own clearance by displacing the surrounding tissues. From this point on, I will refer to the visceral serous pericardium attached to the surface of the heart as “the epicardium”, and the connected layers of the fibrous pericardium and parietal serious pericardium simply as “the pericardium”. Beneath the epicardium lies the myocardium, the muscular layer of tissue that is provides the pumping function. The myocardium makes up the vast majority of the heart.

3.1.3 Heart Kinematics and Dynamics

Points on the epicardial surface of the heart undergo large displacements at high speeds during natural beating. Shechter et al. measured the 3-D displacements and velocities of several landmarks along the left and right coronary arteries using angiograms in 10 patients, the results of which are shown in Figure 3.5 [60]. Over these anatomical locations, they measured the range of maximum resultant displacements to be from 8–23 mm. The range of maximum velocities for the same anatomical locations was 34–131 mm/s. HeartLander will be directly subjected to these high displacements and velocities as it travels over the epicardium. These physiological motions will present challenges to both effective locomotion and positioning accuracy.

The normal forces generated by the pericardium over the heart also fluctuate over the physiological cycles. Although total heart volume remains relatively constant when compared to the variations of the heart chamber volumes, it varies approximately 8 – 10 % over the heart cycle [61]. The minimum heart volume occurs at the end of ventricular systole, after the ventricles have ejected their supply of blood out of the heart (Figure 3.6). Because the pericardium applies pressure to the epicardial surface to restrain the volume of the heart, this pericardial pressure varies with the volume of the heart [62], [63]. Measurements of intrapericardial pressure in humans have shown it to vary from 0 to 17 mmHg [62]. Pericardial pressure also fluctuates slightly (from 2 to 6 mmHg) over the respiration cycle [64], [65]. The intrapericardial pressure generates the normal force applied to HeartLander, and thus the friction forces experienced during motion beneath the pericardium.

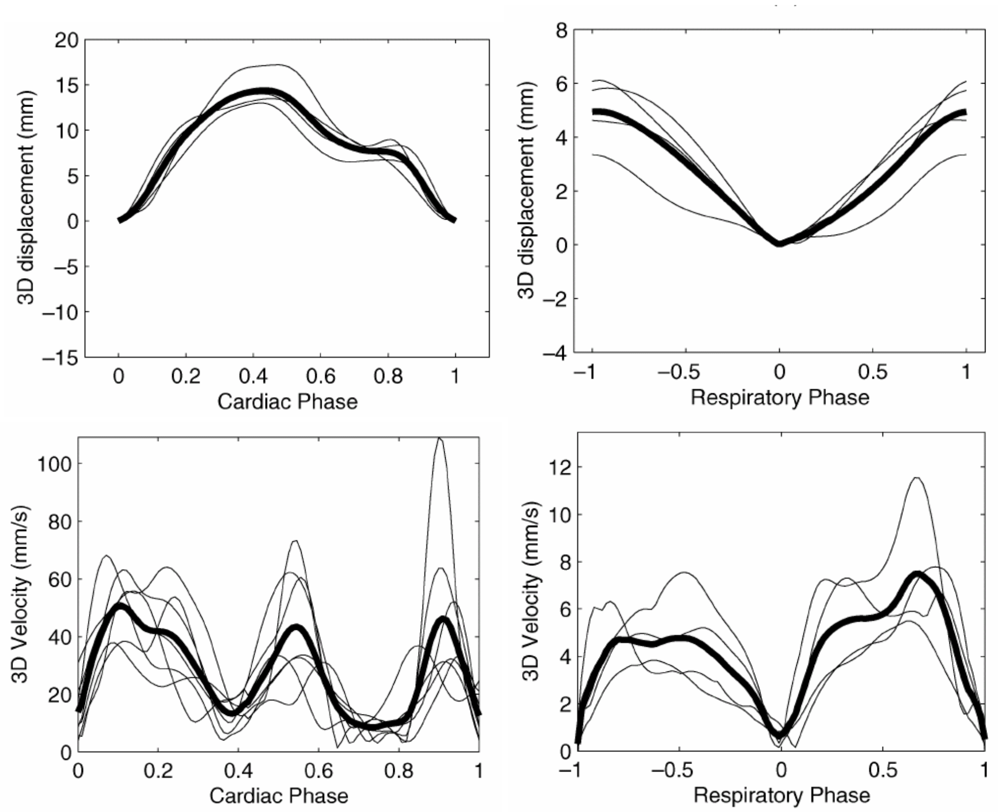

Figure 3.5: Data showing the 3D (upper-left) displacement of the right coronary artery (RCA) due to cardiac motion, (upper-right) displacement of the RCE due to respiratory motion, (lower-left) velocity of the RCA due to cardiac motion, and (lower-right) velocity of the RCA due to the respiratory motion. The average for the 10 human subjects is shown in bold. All data are plotted over the phase of the physiological cycle to which they are attributed. This figure reproduced from [60].

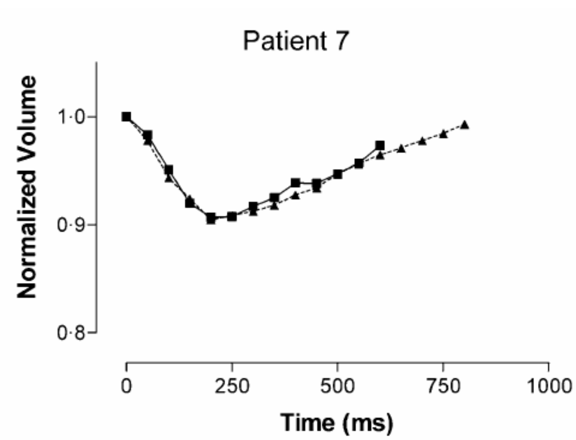

Figure 3.6: A measure of total heart volume (the volume of the contents of the pericardium) using MRI for a typical human over one heartbeat cycle. The THV variation in a human is typically between 8 – 10 %. The two curves show the measure of THV before and after a cardiac procedure. This figure reproduced from [61].

Gilhuly et al. measured the forces and torques on a custom mechanical stabilizer (similar to the Medtronic Octopus™) attached to the anterior epicardial surface of a porcine heart [66]. These measurements were then extrapolated to human values according to the known relationships between body mass and various properties of the heart. Data for the right and left ventricles were similar. The shear force along the base-to-apex axis of the heart ranged from -2 to 2 N, while the shear force in the lateral direction ranged from -0.5 to 0.8 N. The normal force ranged from -6 to 4 N. These shear forces will be applied to the upper surface of HeartLander by the pericardium.

In addition to the shear forces imposed on HeartLander by the heartbeat motion and the normal force imposed by the distention of the epicardium and pericardium, HeartLander must overcome the weight of the heart when it is on the posterior wall of the heart with the subject in the supine position. For humans, heart weight is approximately 5g per 1kg of body weight [67]. Normal heart mass for men is less than 400 g, and for women is less than 350 g. However, heart mass can increase up to 800 g in cases of extreme hypertrophy – thickening of the ventricle walls due to scarring. This will result in a normal force ranging from 3.5 to 7.8 N.

3.1.4 Tissue Mechanics

The epicardium is a thin (0.1 mm) serous membrane consisting largely of a 2D plexus of collagen and some elastin fibers, with an outer layer of mesothelial cells [67]. Experiments in which excised portions of epicardial tissue were biaxially stretched have shown that it exhibits highly nonlinear stress-strain behavior [68]. A plot of the stress-strain behavior in Figure 3.7 shows that the tissue is compliant at low levels of stretch, then quickly stiffens after reaching a threshold. This tissue is also isotropic – similar properties in both axes – within the compliant regime, but becomes anisotropic as the tissue stiffens [68]. The nonlinear stress-strain property of the epicardium suggests that as HeartLander grips the tissue to generate traction during locomotion, the robot will likely stretch the tissue some amount before it stiffens and provides the necessary reaction forces.

The pericardium has a similar tissue composition as the epicardium (a 2D plexus of collagen and elastin), but is much more thick (0.5 mm). Also like the epicardium, it exhibits compliance at low stretch but eventually become almost inextensible at high stretch (Figure 3.8). In biaxial testing it has been shown to be nonlinear and isotropic, and exhibits hysteresis and relaxation [69]. Because HeartLander must displace the pericardium in order to generate intrapericardial clearance, it is critical for the robot to have a low profile in order to avoid stretching the tissue beyond the compliant regime. If this were to happen, the normal force exerted on the robot by the pericardium would be great, thus making motion difficult.

Human hearts also have a variable amount of adipose tissue between the epicardium and the myocardium [70]. This layer of fat is a metabolically active organ, and is directly attached to the myocardial tissue [71]. It has been suggested that epicardial fat serves as a local energy supply for the adjacent myocardium, and as a buffer against toxic levels of free fatty acids [72]. It is commonly found in the grooves or sulci between the chambers of the heart, but can cover 67 to 100% of the myocardial surface in elderly or diseased human hearts. Figure 3.9 shows a human heart that is completely covered in epicardial fat. The layer of epicardial fat tends to be the thickest (up to 11 mm) on the anterior and lateral walls of the right ventricle, and on the anterior wall of the left ventricle. In a clinical setting, HeartLander would likely be used on diseased hearts, and thus the presence of epicardial fat must be assumed. Although total coverage of thick epicardial fat may preclude therapy administered from the intrapericardial cavity, HeartLander must be able to traverse lower levels of fat coverage.

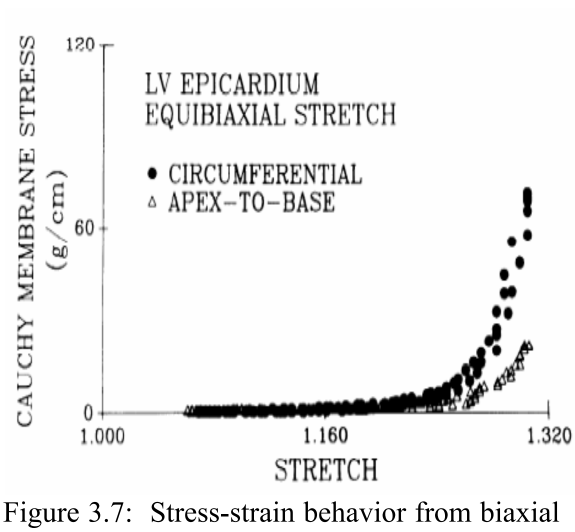

Figure 3.7: Stress-strain behavior from biaxial testing of the epicardium. Notice that the tissue exhibits highly nonlinear stress-strain behavior, in that it is very compliant at lower levels of strain then stiffens quickly after exceeding a threshold. Both tissues also exhibit some hysteresis, and are relatively isotropic. This figure reproduced from [68].

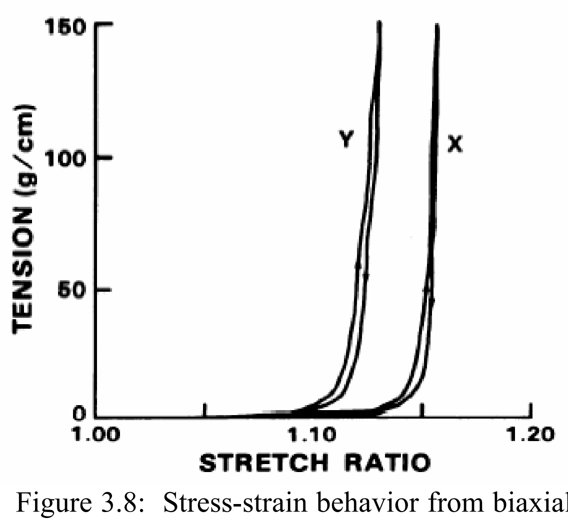

Figure 3.8: Stress-strain behavior from biaxial testing of the pericardium. Notice that the tissue exhibits highly nonlinear stress-strain behavior, in that it is very compliant at lower levels of strain then stiffens quickly after exceeding a threshold. Both tissues also exhibit some hysteresis, and are relatively isotropic. This figure reproduced from [69]

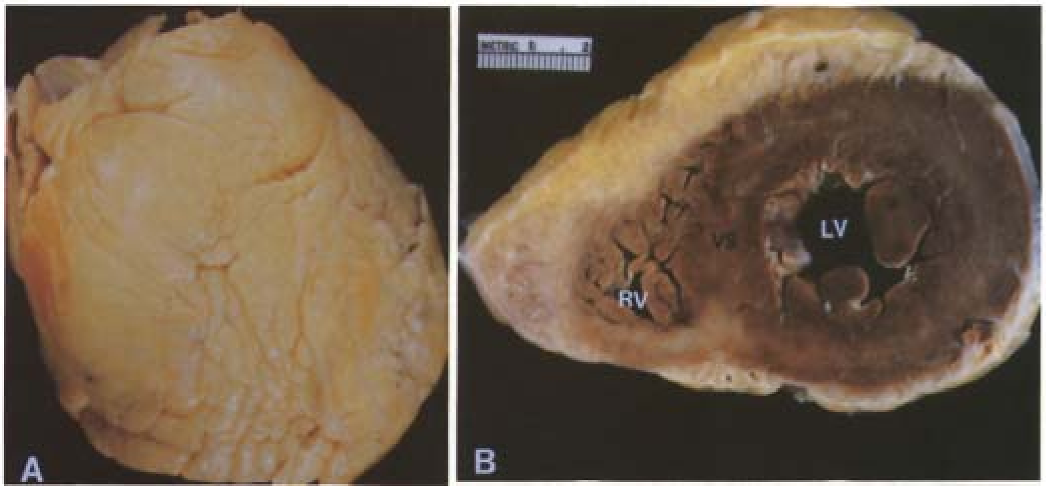

Figure 3.9: (left) Photograph of a human heart completely covered with epicardial adipose tissue (fat). (right) An axial cross section of the heart through the ventricles showing the thickness of the epicardial adipose over the heart surface. Notice that the layer is the thickest on the lateral and anterior walls of the right ventricle, and the anterior wall of the left ventricle; with very little fat on the posterior surface of the heart. Although this is an example of excessive epicardial fat, the distribution is typical. This figure reproduced from [70].

3.2 Intrapericardial Therapies

There is a considerable number of both established and innovative procedures that could conceivably be performed entirely within the pericardium. This means that they do not intrinsically require access to the pleural space or areas outside the pericardium. Examples include:

- cell transplantation [73];
- gene therapy for angiogenesis [74];
- intrapericardial drug delivery [75];
- epicardial electrode placement for resynchronization [76];
- epicardial atrial ablation [77];
- ventricle-to-coronary artery bypass, VCAB [78].

Minimally invasive instrumentation is not currently available for most of these procedures, and those that do exist are typically designed for intercostal transthoracic access. However, all of these procedures could be performed without deflating the left lung if suitable instrumentation were available. These procedures would all benefit from the increased minimally invasive nature of HeartLander, and are thus considered for initial therapeutic applications. From an engineering standpoint, these initial therapies envisioned for HeartLander share three main characteristics: they can be completed entirely from within the intrapericardial space, they require flexible 1-DOF tools, and they comprise multiple treatments made at precise locations on the epicardium. The planning for the treatment sites could be determined from preoperative diagnosis, or created intraoperatively based on readings from diagnostic sensors mounted on the robot. This thesis focuses on the administration of therapies with a definitive preoperative design, and thus a set of predetermined target locations for treatment. The specific intrapericardial therapies being explored are regenerative material injection, pacing lead placement, and epicardial ablation.

For the injection of regenerative materials, we have designed and constructed a novel remote injection system for use from HeartLander. For lead placement and ablation, we deployed commercial therapeutic devices through the working channel of HeartLander. See Section 4.8 for more details.

3.2.1 Myocardial Injection

Congestive heart failure (CHF) caused by myocardial infarction is the leading cause of death in the industrialized world [79]. Myocardial infarction is the death of a region of heart muscle due to the obstruction of the local blood circulation to the tissue, typically caused by the blocking or narrowing of the coronary arteries. The infarct area scars within hours of the ischemic event, and degrades the pumping function of the heart. If the myocardial infarction leads to CHF, the pumping function of the heart fails to meet the circulation demands of the body, typically due to failure of the left ventricle [80]. The severity of this disease is illustrated by the fact that 50% of congestive heart failure patients die with 5 years of diagnosis [81]. Because cardiomyocytes – heart muscle cells – are terminally differentiated, there are currently no effective means to replace scarred myocardium with viable functioning myocardium. Stem cells are precursor cells that are capable of proliferation, self-renewal, and differentiation into cardiomyocytes. Cardiomyoplasty, the injection of stem cells into failing myocardium, offers the potential to reverse the deleterious hemodynamic and neurohormonal effects that result from myocardial infarction and lead to congestive heart failure [79]. Although clinical data on the effects of cardiomyoplasty are very limited, the results of preclinical animal studies and early clinical investigations have shown regenerated myocardium and increased perfusion in the infarct area leading to improved cardiac function [82], [83], [84].

There are three general delivery methods currently used in cardiomyoplasty, the effectiveness of which have yet to be quantitatively determined. The most invasive technique is open-chest intramyocardial delivery, where stem cells are injected directly into the contracting myocardium wall bordering the infarct. This method allows direct visualization of the target zone, and is the preferred approach when the patient is already undergoing an open cardiac procedure [79]. Less invasive techniques include intracoronary and intravascular delivery, which must be further developed to increase the localization of treatment to the targeted myocardium [79]. As the field of myocardial regeneration matures, delivery methods that provide enhanced access in a less invasive manner, such as HeartLander, may prove useful.

3.2.2 Epicardial Pacing

Another potential treatment for congestive heart failure (CHF) is through cardiac resynchronization therapy (CRT). In this procedure, pacing the heart – typically at multiple sites (i.e. biatrial or biventricular pacing) – alters the degree of atrial or ventricular electromechanical asynchrony in patients with major conduction disorders. An estimated 20 – 30% of class III and IV CHF patients have major left ventricular conduction disorders, and are thus considered potential candidates for ventricular CRT [85]. CRT has been demonstrated to improve symptoms and exercise tolerance, as well as reduce mortality due to progressive heart failure by 38% as compared to optimal pharmacological therapy alone [86].

The pacing leads for CRT can be placed using transvenous or thoracoscopic techniques. Although transvenous placement decreased patient morbidity by avoiding thoracotomy, the lead placement success rates vary from 72 – 96 %, and response rates are only 60 – 75 % [6]. Surgical, thoracoscopic techniques – in which the leads are placed in the epicardium – report a 100% placement success rate and lower dislodgement rates [87]. In an attempt to improve the response rates for both placement techniques, researchers are exploring the effect of using electrical mapping to guide lead placement on a patient specific basis [6]. Several recent studies have suggested that the individualization of the pacing configuration can increase the hemodynamic improvement in CHF patients, and also reduces the number of non-responders [88], [89], [90]. As the application of CRT matures, patient-specific mapping and accurate epicardial lead placement could be assisted by HeartLander.

3.2.3 Epicardial Ablation

Atrial fibrillation (AF) is a condition in which the atria rapidly contract without synchronism to the normal heartbeat rhythm. This loss of pumping coordination leads to decreased cardiac output. AF is the most common form of cardiac arrhythmia seen in clinical practice, and has been diagnosed in approximately 2.2 million people in the United Stated and 4.5 million in Europe [91], [92]. The condition is known to be an independent predictor of both death and stroke, and has been associated with significant morbidity [93], [94].

Selective ablation or destruction of cardiac tissue with an electrode to break the faulty conduction pathway is a technique often used to treat AF. Ablation is typically performed by applying radio frequency (RF) energy to the heart, using either an endocardial or epicardial approach. Endocardial ablations can performed with ablation catheters inserted into the heart through the vasculature in a minimally invasive manner. For this reason, endocardial ablation has become the preferred approach for several types of arrhythmias. This technique, however, cannot access transmural or epicardial portions of arrhythmia circuits, and has an average success rate of 76 % (a figure that includes multiple procedures for approximately one third of the patients) [2], [95]. Epicardial ablation is often used to treat AF in the cases for which repeated endocardial ablation have failed. Some researchers are currently investigating methods of performing epicardial ablation in a minimally invasive manner, thus achieving higher success rates with less patient morbidity [95], [96]. Accessing the epicardium in a highly accurate manner through a subxiphoid approach using HeartLander could facilitate epicardial ablation.

Chapter 4

Robot Design

The design of HeartLander enables navigation over the entire epicardial surface of the beating heart in a precise and stable manner, without damaging the surrounding structures. To minimize the associated patient morbidity, the robot also operates within the intrapericardial cavity in situ; i.e., the chest closed, the pericardium intact, and the heart beating. These considerations present a unique combination of difficulties for a mobile robot.

A percutaneous subxiphoid insertion is used to place HeartLander on the apex of the heart in a minimally invasive manner, without requiring differential ventilation and lung deflation. A tethered design allows the functionality of powerful offboard components to be transferred to a robot that is sufficiently small and lightweight to operate within the intrapericardial environment of the heart in situ. A flow chart of the HeartLander system can be seen in Figure 4.1. Vacuum pressure is used to maintain prehension with the epicardial surface in a safe and reliable manner. HeartLander generates inchworm-like locomotion by coordinating the epicardial prehension and the drive-wire actuation of the robot. The inverse kinematics of the crawler were determined for this purpose. A suite of onboard and offboard sensors provides feedback during navigation, and data for offline performance analysis. Several therapeutic end-effectors are proposed for deployment from HeartLander to the epicardium. These components result in a mobile robot that meets the rigorous design requirements within the intrapericardial environment.

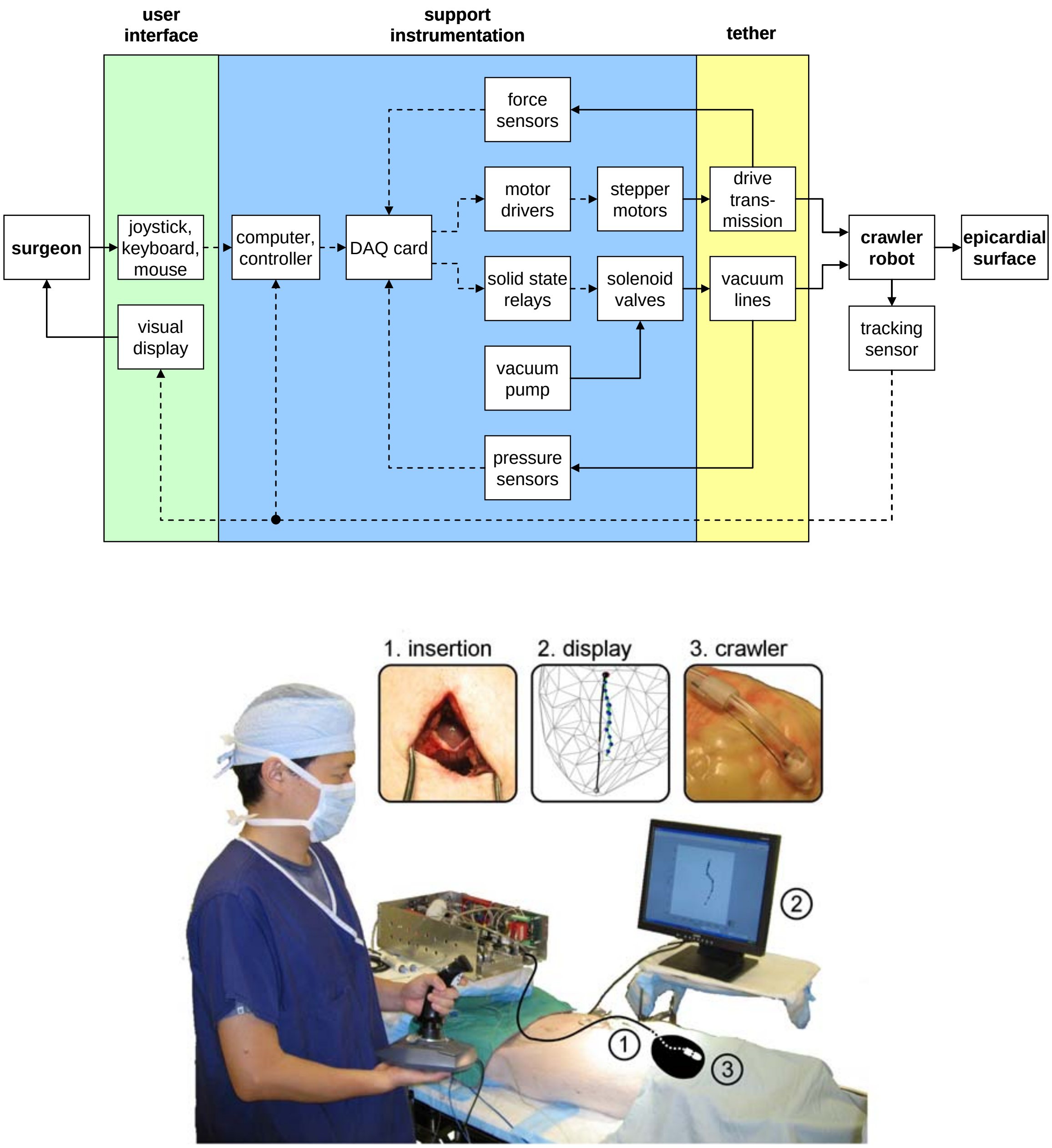

Figure 4.1: (upper) Flow chart for the HeartLander system. Mechanical connections are shown by solid lines, while data flow is shown by broken lines. (lower) Photograph of the operating room during in vivo animal testing, showing the surgeon interacting with the HeartLander system. The approximate heart shape and robot location inside the body have been illustrated for clarity. Insets show larger views of (1) the subxiphoid insertion, (2) the graphical display, and (3) the crawling robot.

4.1 Insertion

Accessing the heart through an incision made below the xiphoid process of the sternum is a compelling minimally invasive approach, which is becoming more commonly used [12], [13] [97], [98], [99]. This is an extremely efficient access method because it provides access to all of the chambers of the heart from the apex (Figure 3.4) and avoids entering the pleural spaces of the lungs (Figure 4.2). Traditional and robotic thoracoscopic tools are inserted between the ribs, using an intercostal approach to access the heart. To avoid accidentally penetrating the left lung with the rigid instruments, this approach requires general endotracheal anesthesia, differential ventilation, and deflation of the left lung. HeartLander will be placed directly on the epicardial surface of the apex either by hand, or with assistance from a rigid subxiphoid videopericardioscope (SVP) [12]. This device has a transparent conical tip that allows it to separate the intervening muscular and connective tissue of the sternum, thus clearing a direct path to the heart (Figure 4.2). The main channel contains an endoscope to visualize the insertion procedure. A second, inferior channel contains a grasper tool that is used to grab the pericardium and draw it back into the sharp edge of a cutting tool. This passively makes an incision in the pericardium. HeartLander will then be inserted directly onto the epicardial surface through the SVP working channel, or through a port inserted after the SVP is extracted. Once the treatment is complete, HeartLander will be retrieved by walking backwards or manually retracting the tether back through the port. Manual retraction also serves as the recovery method should the device become dislodged or damaged during the procedure. The tether has been made sufficiently strong for this purpose.

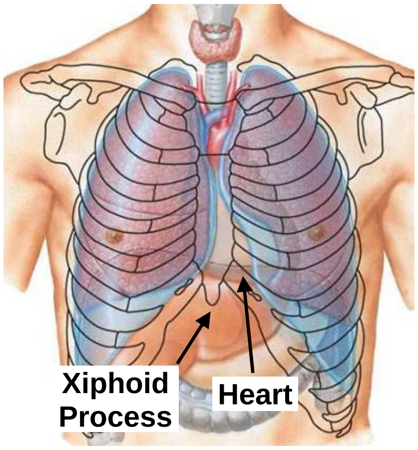

Figure 4.2: (left) Illustration of the thorax with the ribs and organs visible. Notice direct pathway from the xiphoid process of the sternum and the heart that does not pass through the blue pleural spaces of the lungs. Image reproduced from Netter Presenter, 2000. (right) The subxiphoid videopericardioscopy (SVP) device inserted through a small subxiphoid incision *(circled)*. Inset shows a close-up of the distal end of the SVP. The upper channel is occupied by a 4-mm diameter endoscope enclosed by a conical transparent tip, while the inferior channel is open for use as a working channel. Shown here are the pericardial graspers and cutting tool for epicardial access. This figure reproduced from [12].

4.2 Tethered Design

The HeartLander system consists of a miniature crawling robot that is connected to a suite of off-board support instrumentation through a flexible tether (Figure 4.3). This design allows the therapeutic portion of the robot to be small, robust, lightweight, and potentially disposable. Because the intrapericardial space has less than 1 mm of clearance, HeartLander must expand the pericardium to create its own clearance (Figure 3.1). Accordingly, the size of the robot must be made sufficiently small that the pericardium and surrounding organs do not impede the motion of the robot. By offloading the functional components of the robot – i.e., the motors, vacuum pump, and valves – the tethered crawling portion can be made sufficiently small for this purpose. The tethered design also allows the crawler to be simple and robust, which is critical for reliable operation in the constrained and volatile intrapericardial environment. Lastly, the crawler is mechanically and electrically passive, which is important as a safety concern.

The maneuverability of the crawling robot is not significantly hindered by the presence of the tether because the intrapericardial space is a single continuous volume. This means the epicardium of all four chambers of the heart can be reached from the apex by a relatively straight trajectory (Figure 3.4). Accordingly, tight turning maneuvers that would be difficult to execute with a

Figure 4.3: The supporting instrumentation boxes that house the motors and controls (left), the vacuum pump (upper right), and tethered crawling robot (lower right).

tether are not necessary. Additionally, the maximum required length of travel for the robot is limited by the distance from the robot insertion location to the base of the heart. This distance is approximately 150 mm in humans [100]. In our present design, the tether is 650 mm in length so that the offboard instrumentation can be positioned away from the patient in a manner convenient to the surgeon.

4.3 Locomotion Methodology

HeartLander generates a cyclic, inchworm-like gait by controlling the distance between the two bodies of the robot and the vacuum pressure in the corresponding suction grippers. This locomotion modality was selected because we believed that prismatic actuation was more reasonable than rotational actuation through a tether, and that the resulting crawling behavior would be able to overcome the spatial constraints and topological irregularities in the intrapericardial space [101]. One cycle of the locomotion process is illustrated schematically in Figure 4.4. During extension, the front body is advanced by powering the actuators while the rear body is fixed to the epicardium. During retraction, the rear body is advanced to meet the front body by reversing the actuators after epicardial prehension has been transferred from the rear to front body. This loco

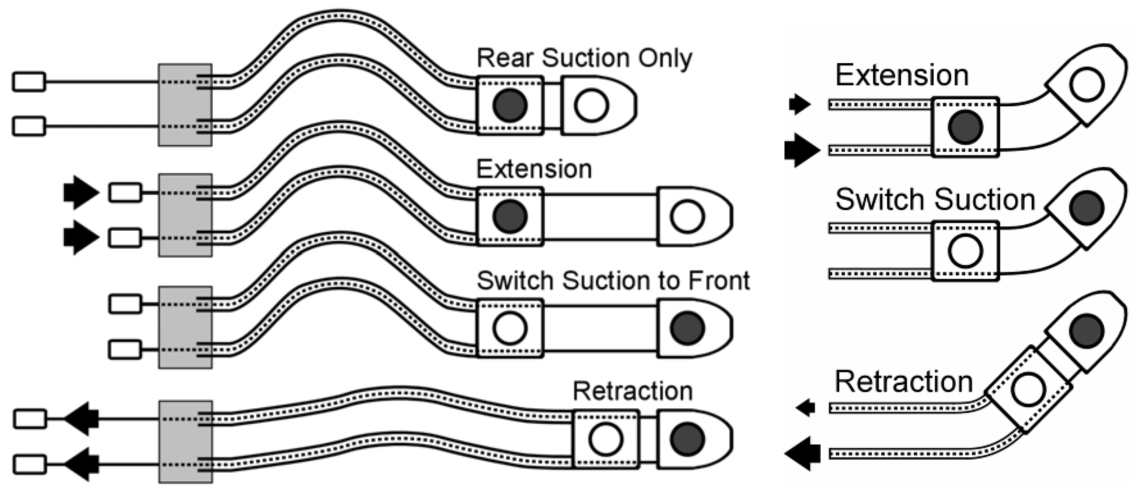

Figure 4.4: (left) Illustration of one cycle of the HeartLander crawler locomotion. The shaded circles show body with active prehension of the epicardium. The arrows indicate the direction in which the prismatic actuators are powered. (right) Illustration of turning, accomplished by differentially actuating the drive wires.

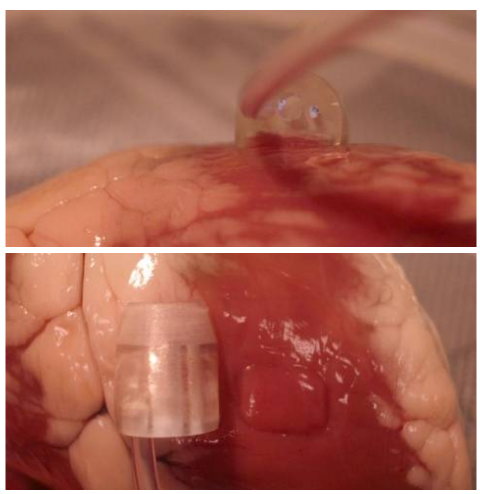

Figure 4.5: (upper) Photograph of HeartLander body section drawing ovine epicardium into its vacuum chamber, and (lower) the suction mark in the tissue the was left behind.

motion scheme requires that some amount of slack be maintained in the tether, and thus the tether has been made sufficiently long. Turning is achieved by choosing a step location for the front body that has a non-zero bending angle.

If the body with active prehension of the epicardium does not slip during either the extension or retraction phases, the efficiency for the step is 100%. This would result in the robot advancing by the full step length. In the intrapericardial environment, however, the body with prehension of the epicardium often slips somewhat, resulting in a step efficiency less than 100%.

4.4 Prehension

Prehension of the epicardial surface is maintained using suction force generated by negative pressure, which can be easily transferred though the tether and has been demonstrated to be safe and effective in commercial medical devices. These FDA-approved positioning and stabilizing devices typically apply a pressure that is no greater than 400 mmHg [9], although some researchers report that the vacuum pressure can temporarily be increased to 600 mmHg without adverse effects on the underlying tissue or vessels [10]. The suction grippers on HeartLander should cause even less epicardial damage than mechanical stabilizers because they are applied for a far shorter duration, and move passively with the epicardium instead of constraining it. Thin latex strips surround the periphery of each suction gripper, helping to create a vacuum seal with the epicardium. Vacuum pressure from the external pump is supplied to the suction pads of the body sections through two vacuum lines that pass through the tether. Preliminary tests with freshly excised ovine (sheep) hearts showed that the epicardium was completely drawn into the vacuum chamber and provided a qualitatively good grasp (Figure 4.5). During locomotion, the vacuum pressure is monitored by external pressure sensors and regulated by computer-controlled solenoid valves, both located in the supporting instrumentation.

As an interesting alternative technology, researchers are attempting to fabricate biologically inspired synthetic gecko foot hairs [47], [102]. These techniques develop arrays of spatulae or miniature fibers – mimicking those on the feet of geckos – to form a dry adhesive capable of adhering to almost any surface, wet or dry, smooth or rough. When this technology matures, it may prove a viable supplement or alternative to suction.

Benchtop experiments were performed in order to quantify the effects of varying the shape of the suction pads used to grip the epicardium, and on the ability of the suction pads to grip the heart in the presence of epicardial fat. These studies are described in the following subsections.

4.4.1 Chamber Shape Study

This study was an attempt to investigate the traction generated by numerous mechanical designs of the suction pad grippers for HeartLander [103]. Our testing setup measured the force applied to a gripper pad adhering to excised ovine (sheep) epicardial tissue. The gripper pad was pushed until it lost traction and began to slide across the epicardial surface. Video was recorded in order to track the pad and tissue during the extension. By synchronizing the force and video data, we were able to reliably determine the point at which the pad lost traction and began to slip during the extension. This maximum force prior to slip was the evaluation criteria by which the design and locomotion parameters were evaluated. Of the suction pads tested (Figure 4.6), the pad with no suction grate achieved maximum traction (Figure 4.7). These experiments provided physical design specifications to improve the traction of HeartLander on excised ovine epicardial tissue.

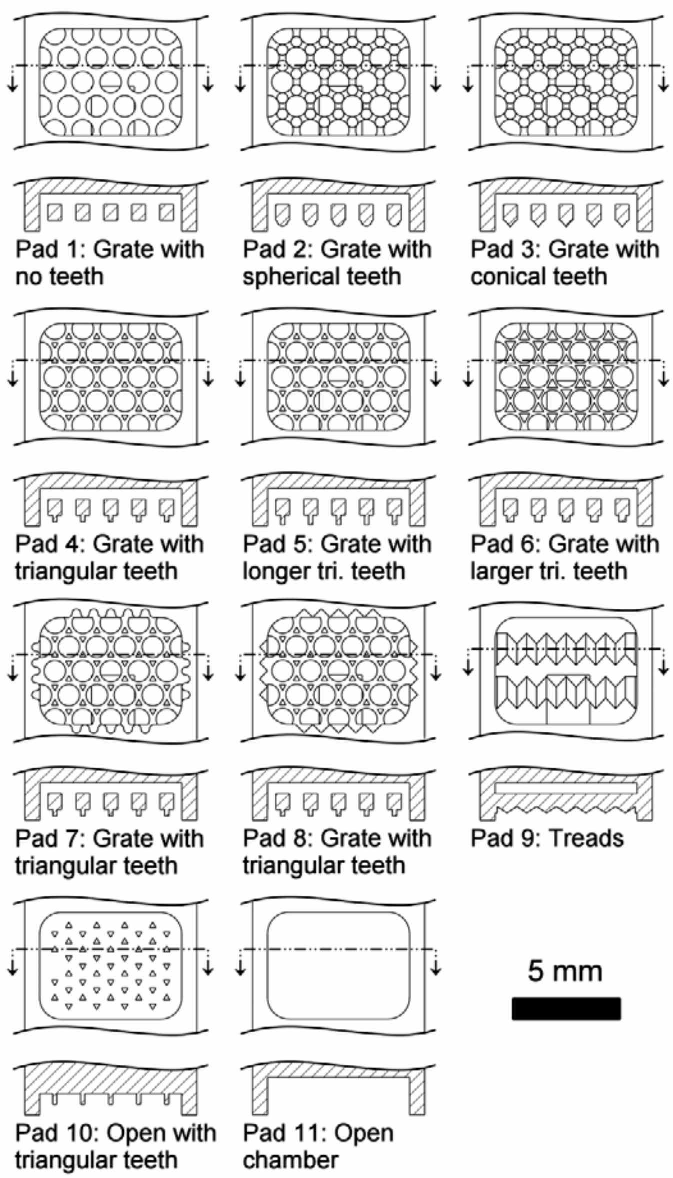

Figure 4.6: Bottom surfaces and profile cross sections for the gripper pads tested for traction on excised ovine (sheep) hearts.

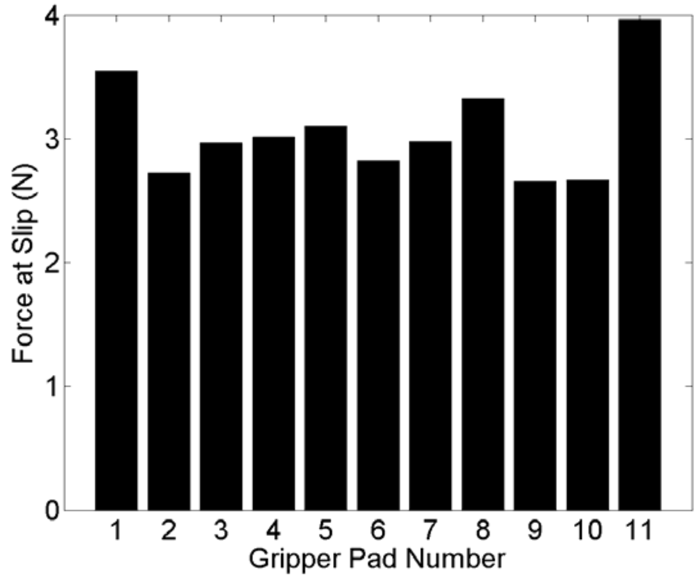

Figure 4.7: The forces recorded at the loss of traction for the different gripper pads extended at a speed of 2 mm/s with vacuum pressure of 400 mmHg.

4.4.2 Chamber Depth Study

In this study, the depth of an open circular suction pad – validated by the previous study – was varied in order to determine the effect of generating traction with the epicardium. The 6-mm diameter suction pad was tangentially sheared over ovine epicardial tissue, with the maximum traction recorded with a handheld force gauge. The maximum traction was recorded for suction chamber heights of 2 and 4 mm, over a pressure range of 100 to 400 mmHg. Photographs of the epicardial tissue being drawn into the suction chambers at the two chamber heights over the pressure range can be seen in Figure 4.8. In the case of the 2-mm chamber height, the epicardial tissue was completely drawn against the top of the suction chamber at approximately 300 mmHg. For the suction chamber with a height of 4 mm, the epicardial tissue did not contact the chamber ceiling, even at the maximum pressure of 500 mmHg. The plots of the maximum traction forces required to slide the suction chamber over the epicardial tissue, seen in Figure 4.9, show that increasing the depth of the suction chamber did not effect the maximum epicardial traction. As expected, the traction increased with vacuum pressure. This study validated the use of a relatively shallow open suction chamber, in which the epicardium maintains complete contact with the ceiling of the chamber.

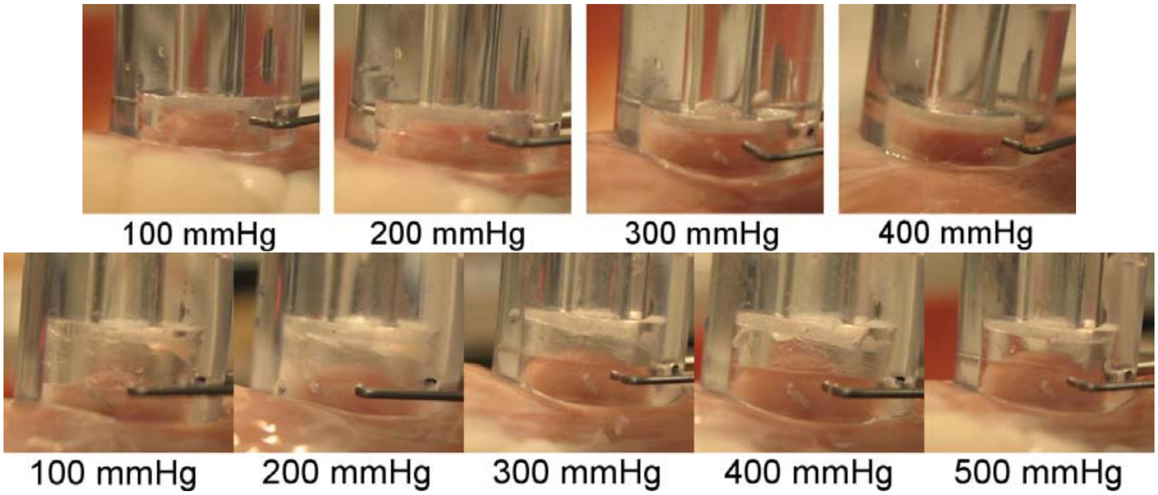

Figure 4.8: Photographs of the ovine epicardial tissue drawn into the variable depth suction chamber by increasing vacuum pressure with the chamber depth set to 2 mm (upper row) and 4 mm (lower row)

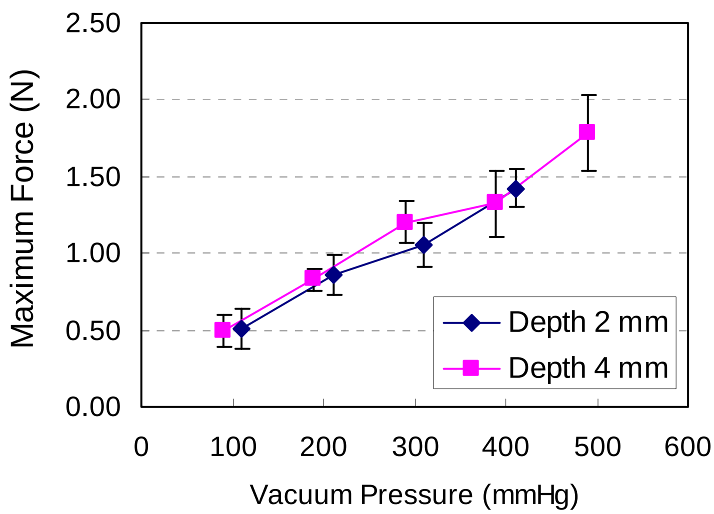

Figure 4.9: Plot showing the maximum traction forces when the front body was sheared off the ovine epicardium with increasing vacuum pressure at depths of 2 mm (diamonds) and 4 mm (squares).

4.4.3 Epicardial Fat Study

Due to the likelihood that the diseased hearts on which HeartLander will be traveling will be covered in some amount of epicardial adipose tissue (fat), it was important to determine how this anatomical structure will affect locomotion. The first issue was to determine whether the suction line or suction chamber will become clogged after repeated steps across epicardial fat. The second issue was to quantify the ability of the robot to generate traction on the epicardial fat, as this is critical for successful locomotion. Ovine (sheep) hearts were used in this study, as they tend to have more epicardial fat than porcine hearts. The hearts were tested within one hour from being excised from the animal, and were kept warm within a saline bath heated to the average ovine internal body temperature (39° C). We defined four classifications of epicardial fat coverage: lean myocardium, thin epicardial fat, thick epicardial fat, and exposed epicardial fat (Figure 4.10). The lean myocardium had no epicardial fat. Thin epicardial fat was defined as having a thickness of less than 1 mm, under which the myocardium was visible. Thick epicardial fat was defined as having a thickness of 3 mm or more, under which the myocardium was not visible. For the exposed epicardial fat classification, the epicardial layer that naturally covers the adipose tissue was dissected away (Figure 4.10).

The front body of a typical robot crawler with an open suction chamber was used in both the suction clogging and traction generation experiments. The suction chamber was supplied with a vacuum pressure of 400 mmHg, which is within the range proven to be safe for the epicardium. In the suction clogging experiments, the front body was dragged 20 mm across the heart surface with the vacuum pressure active at two locations that featured the thick epicardial fat and exposed epicardial fat classifications. These trials were repeated 50 times at each location. The bottom of the suction chamber was photographed after every 10 trials, and the suction chamber was thoroughly cleaned of any accumulating epicardial fat deposits between the two locations. In the traction generation experiment, the same crawler body was dragged 20 mm across the heart surface with the vacuum pressure active at four locations featuring the four classifications of epicardial

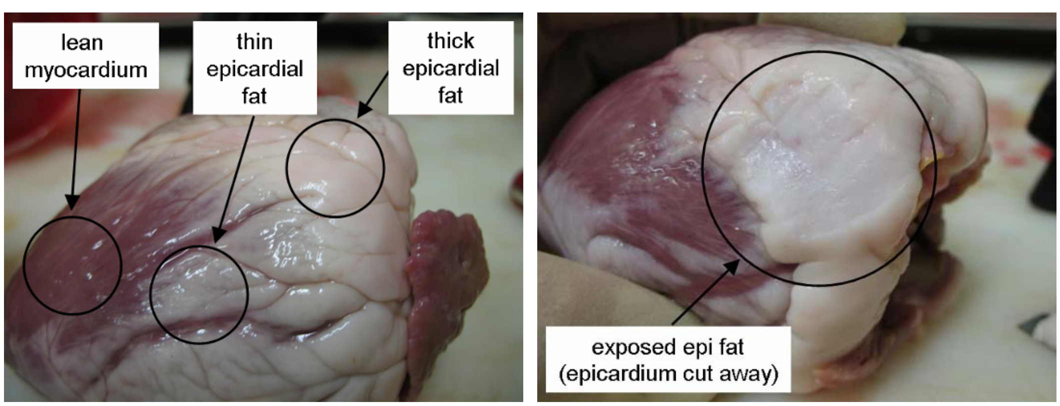

Figure 4.10: (left) Photograph of a freshly excised ovine (sheep) heart with three of the epicardial fat coverage classifications that we defined for this study: lean myocardium, thin epicardial fat, thick epicardial fat, and exposed epicardial fat. (right) Photograph of a freshly excised ovine (sheep) heart with the fourth epicardial fat coverage classification: exposed epicardial fat. For this classification, the epicardial was dissected away from the heart in order to expose the underlying adipose tissue.

fat coverage. The maximum traction force for each trial was recorded by pulling the body with a handheld force gauge. These trials were repeated five times at each of the four locations.

Repeatedly dragging the crawler body over epicardial fat with the vacuum pressure active illustrated that the epicardial fat will not clog the suction line, but does accumulate in the suction chamber. Figure 4.11 shows photographs of the suction chamber after every ten trials on a region of the heart with thick epicardial fat coverage. It can be seen that the front corners of the suction chamber, which were facing opposite to the direction in which the body was dragged, accumulated epicardial fat over the experiment. For the same experiment conducted over the exposed epicardial fat, the accumulation of fat in the suction chamber was more pronounced. It can be seen in Figure 4.12 that the entire front face of the suction chamber became completely filled with the dislodged epicardial fat after just 10 trials. After approximately 20 trials, no further accumulation of fat was possible within the suction chamber. The suction line did not become clogged with dislodged epicardial fat in either experiment.

The traction experiment showed that the suction chamber was able to generate traction on the surface of ovine hearts with thin or thick epicardial fat coverage, but not on exposed epicardial fat. The suction chamber generated an average of 1.5 and 1.4 N of traction on the lean myocardium of the left and right ventricles, respectively (Figure 4.13). These measures served as controls because was no epicardial fat coverage on the heart at these locations. The average traction on the heart with thin epicardial fat was 2.2 N, while the average traction was 1.4 N over thick epicardial fat coverage. On the exposed epicardial fat, however, the average traction was only 0.3 N. The traction on the exposed epicardial fat decreased over the course of the five trials, likely due to the accumulation of dislodged fat along the inside of the suction chamber seen in the previously described experiment (Figure 4.14).

In conclusion, the presence of normal epicardial fat did not clog the suction lines or suction chamber of the crawler, and the suction chamber was able to generate traction over epicardial fat as well. Although some epicardial fat did accumulate in the open suction chamber when dragged over thick epicardial fat, the traction study illustrated that this accumulation did not decrease the ability of the suction chamber to generate traction. The far greater accumulation when the crawler was dragged over exposed epicardial fat did adversely affect the traction generated by the suction pad. Fortunately, we do not expect that HeartLander will often encounter exposed adipose tissue, because the epicardium naturally covers this tissue on the heart.

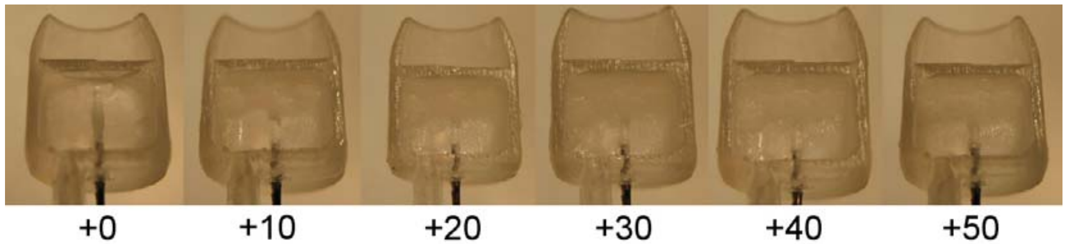

Figure 4.11: Photographs of the open suction chamber after every ten dragging trials on a region of the heart with thick epicardial fat coverage. It can be seen that the front corners of the suction chamber, which were facing opposite to the direction in which the body was dragged, accumulated epicardial fat over the experiment. The vacuum line did not become clogged with the displaced epicardial fat.

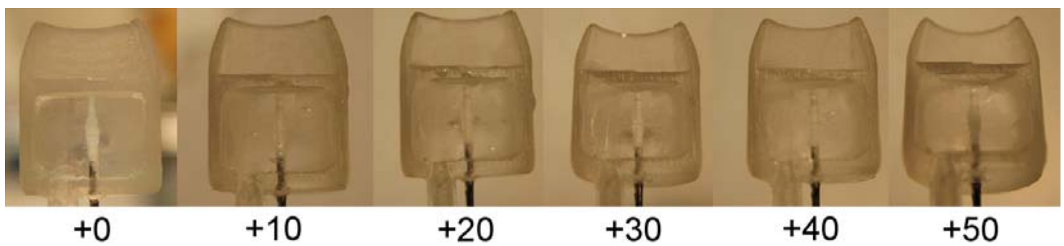

Figure 4.12: Photographs of the open suction chamber after every ten dragging trials on a region of the heart with exposed epicardial fat coverage. It can be seen that the entire front edge of the suction chamber, which were facing opposite to the direction in which the body was dragged, became completely filled with epicardial fat after approximately 10 trials. The vacuum line did not become clogged with the displaced epicardial fat.

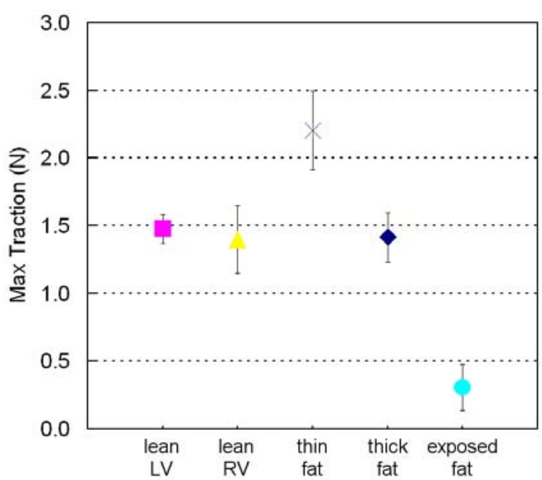

Figure 4.13: The mean and standard deviation of the maximum traction testing over the four classifications of epicardial fat coverage. The suction pad generated similar traction over the lean myocardium, thin, and thick epicardial fat coverage. The maximum traction on the exposed epicardial fat decreased significantly.

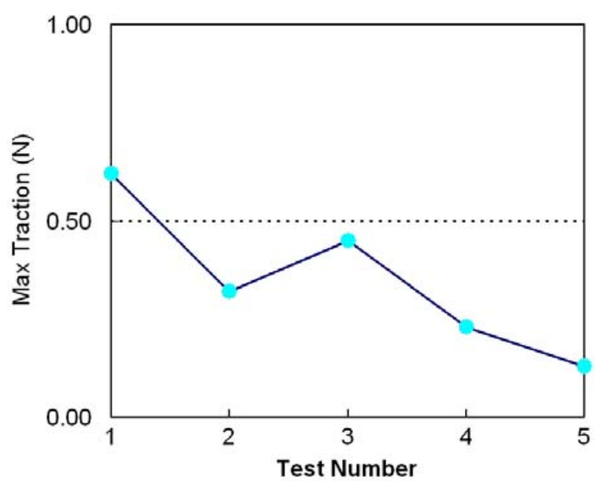

Figure 4.14: A plot of the traction testing of the open suction pad over the exposed epicardial fat.The traction was poor to begin with, and decreased significantly over the testing. It is likely that this trend reflects the fact that the front edge of the suction pad quickly became completely covered with dislodged adipose tissue.

4.5 Crawling Robot

Three actuation methods have been investigated for implementing the inchworm-like locomotion described in Section 4.3: cable-drive actuation, wire-drive actuation, and onboard motor actuation. All prototypes consist of front and rear bodies that are created using stereolithography from a low viscosity liquid photopolymer that cures in a strong, tough, water-resistant plastic that offers many properties similar to traditional engineering plastics like ABS. Each crawler body has an independent suction pads for prehension of the epicardium using vacuum pressure, as described in Section 4.4. The design, construction, and testing of the prototypes developed using these actuation modes are described in the next three subsections.

4.5.1 Cable-Driven

The cable-driven HeartLander has two active degrees of freedom (DOF) and one passive DOF, and can be seen in Figure 4.15. The active degrees of freedom are actuated by two sets of antagonistic cable pairs. One cable pair provides rotation of the rear body relative to the suction pad on which it sits, which allows turning. The other cable pair controls the translation of a prismatic joint connecting the rear and front body sections, allowing the robot to extend and retract. Stainless steel 3x7 braided cable with a diameter of 0.23 mm is used in both cable pairs. Sheathing to maintain tension in the cables is provided by small plastic tubing. The passive degree of freedom is provided by a flexible connection between the prismatic joint and the front body section. This allows the front body to pitch in order to passively adapt to the curvature and motion of the epicardial surface.

Inchworm-like locomotion is accomplished through coordination between the motors controlling the two cable pairs and the solenoid valves that regulate the vacuum pressure in the front and rear suction pads, as described in Section 4.3. This internal coordination of locomotion is maintained by the control system, and is thus transparent to the physician. A joystick provides a simple manner with which to administer the following four commands: *rotate right*, *rotate left*, *walk forward*, and *walk backward*. The turning and locomotion speed can also be adjusted from the joystick, allowing fine position control in sensitive situations. Throughout the locomotive cycle, the software monitors the readings from external pressure sensors attached to the vacuum lines to ensure that at least one suction pad maintains a grip on the heart surface at all times.

The cable-driven HeartLander prototype was bench tested using a poultry tissue model [104]. The robot was able to travel across the surface of the tissue without restriction from the tether, and perform dye injections (Figure 4.16). Although this prototype generated acceptable benchtop locomotion, the larger size of the crawler and friction between the moving parts made locomotion on a beating heart phantom (with pericardium) impossible. Accordingly, this design was not tested on a living animal model.

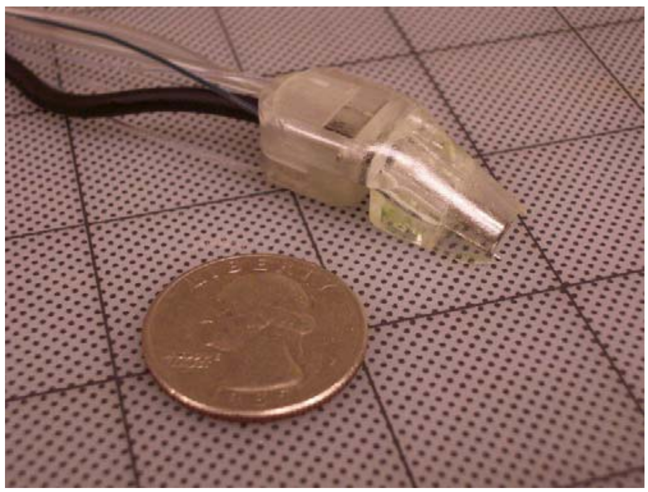

Figure 4.15: The cable-driven HeartLander prototype. The upper arrow highlights the 3.5-mm diameter CCD camera through the translucent tapered front body, while the lower arrow highlights the needle. The height of the robot is 10 mm and the length is 30 mm.

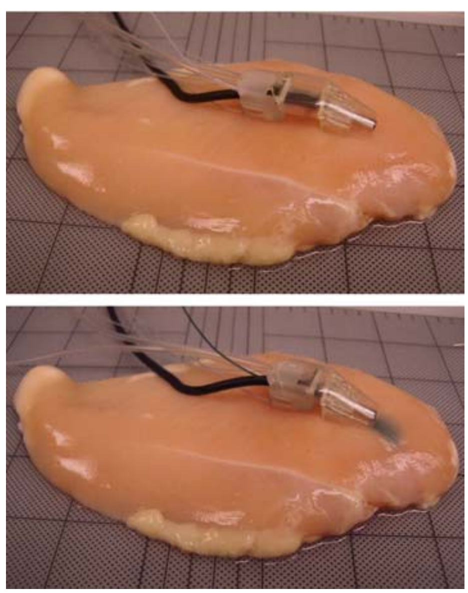

Figure 4.16: The cable-driven HeartLander prototype performing locomotion over poultry tissue, and performing a dye injection.

4.5.2 Wire-Driven

The wire-driven prototype consists of two tandem bodies that independently adhere to epicardium (Figure 4.17). Each body is 5.5 x 8 x 8 mm (H x W x L), and weighs 0.3 g. The distance between the front and rear bodies is controlled by a pair of nitinol drive wires that run longitudinally through the tether, connecting the front body and the offboard motors. Low-friction plastic sheaths, which are attached to the rear body, encapsulate the drive wires as they pass through the tether and transmit the wire forces to the rear body. The two DOFs provided by the pair of drive wires allow the angle and distance between the bodies to vary based on the lengths of the wires between the bodies. This type of robot, which bends continuously along its length through elastic deformation, rather than at discrete joints, is known as a continuum robot. The drive wire configuration exhibits high bending compliance in the direction normal to the transverse plane of the robot (i.e., the *z*-axis), which permits the pericardium to naturally force the robot into contact with the heart surface. Accordingly, navigation on the heart surface reduces to a two-dimensional problem where the rotational and transverse DOFs provided by the drive wires are sufficient to span the epicardium. This continuum robot design facilitates a simple and small form factor for the crawler that passively conforms to the rapidly varying curvature of the heart without the need for a complicated force feedback system [105]. When the bodies are brought close together, the wire compliance diminishes, thus providing a more stable connection between the bodies. The nitinol drive wires are used for their super-elastic properties, and are not actuated using thermal variation. This prototype produced acceptable locomotion on a beating heart phantom with the pericardium intact, and thus was further refined and tested on live animal models (Chapters 6 and 7).

4.5.3 Onboard Motor

A prototype that features onboard motors was developed for the purposes of reducing tether stiffness, and thereby increasing turning efficiency. The prototype, shown in Figure 4.18, is 8.5 mm

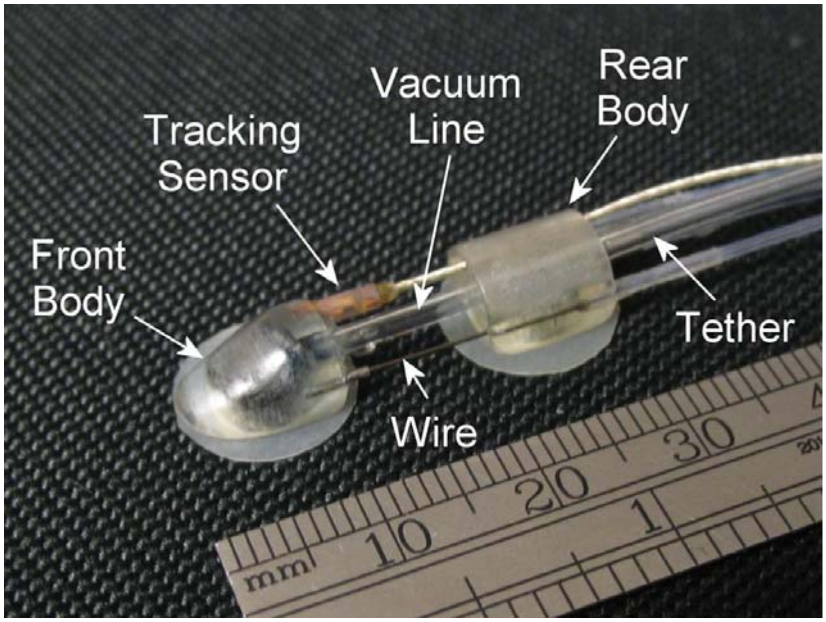

Figure 4.17: Photograph of the HeartLander crawling robot. The bottom of each body contains a suction pad for prehension of the epicardium; vacuum pressure is transmitted through vacuum lines in the tether. Two drive wires transmit the actuation from the offboard motors for locomotion. A 6-DOF electromagnetic tracking sensor is mounted to the front body.

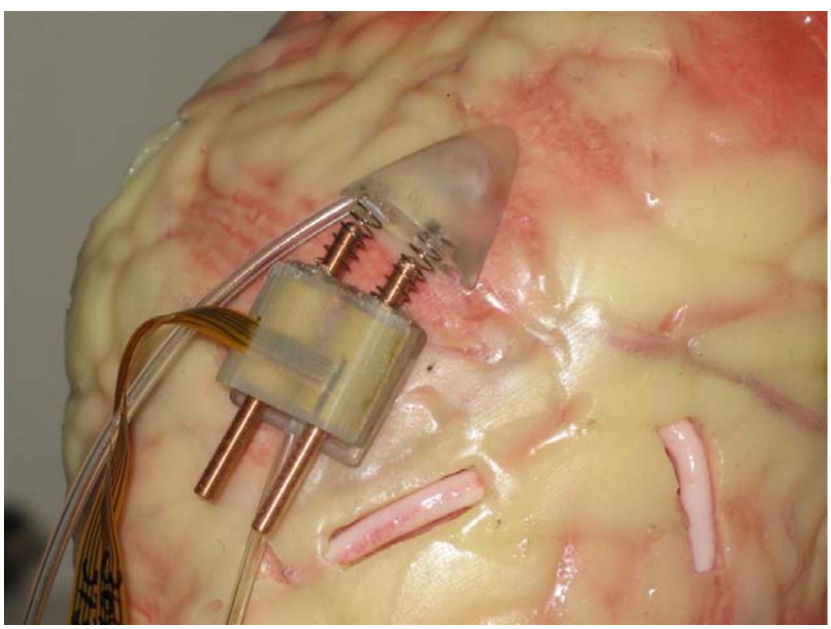

Figure 4.18: HeartLander crawler with onboard motors. HeartLander prototype with onboard motors. This prototype measures 8.5 mm high, 15 mm wide, and 46 mm long. The prototype has demonstrated locomotion on the anthropomorphic heart phantom.

high, 15.0 mm wide, and 45.5 mm long. Locomotion is accomplished in the same general manner as the other HeartLander prototypes, using an alternating inchworm-style locomotion, with each of the two feet having suction to adhere to the epicardium. The robot is entirely controlled using a LabView™ Virtual Instrument (National Instruments, Austin, Texas).

The feet were rapid-prototyped via stereolithography apparatus (American Precision Prototyping, Tulsa, Ok.) using Watershed™ 11120 stereolithography resin. The rear foot of the robot houses two ultrasonic piezoelectric linear motors (Squiggle SQL-3.4, New Scale Technology, Inc., Victor, N.Y.). Each motor is capable of an output force of 1 N. During the extension phase of each locomotion cycle, with the rear foot locked down via suction, each linear motor pushes a threaded rod forward in order to advance the front foot. During the retraction phase, after active suction is switched to the front foot, the direction of travel of the linear motors is reversed, and a spring pulls the rear foot forward to meet the front foot. The crawler has demonstrated locomotion on artificial surfaces and on the beating heart phantom. The maximum speed is 0.004 m/s.

There is a tradeoff between onboard- and offboard-motor prototypes: in principle, onboard motor designs allow a more flexible tether, since there are no drive-wires coming from outside, and this facilitates steering. However, the need to mount the motors within the crawler makes the problem of miniaturization more challenging, a difficulty that must be addressed in light of the spatial constraints of the intrapericardial environment. Accordingly, the onboard motor prototype is considered for future development and miniaturization, but not for live animal testing.

4.6 Kinematics of Wire-Drive Crawler

This section develops the inverse kinematics for the wire-driven crawler. The wire-driven crawler is used in all further testing because it performed the best in benchtop testing. During navigation and fine positioning, the front body must be precisely maneuvered with respect to the stationary rear body. The inverse kinematics provide the relationship between the wire lengths between the bodies (i.e., the joint space variables) and the pose of the front body (i.e., the work space variables). The external normal force exerted by the pericardium on the robot allows us to consider navigation over the curved heart surface as a simplified 2-D problem. The direct mapping of these planar kinematics onto the curved surface of the heart causes an error between the robot pose calculated from the inverse kinematics and the true robot pose on the curved epicardium. This error, however, can be largely neglected because the average curvature of the heart–particularly the ventricular surfaces–is relatively small over the distances traveled in a single step of the robot [106]. Furthermore, this approximation increases in fidelity as the robot approaches the target and the step size correspondingly decreases (Figure 5.12).

Determining the inverse kinematics of a planar continuum robot can be reduced to predicting the length and shape of the curve formed by the primary backbone. In the case of the HeartLander crawling robot, the primary backbone is the extensible imaginary curve located halfway between the two wires, and bounded by the front and rear bodies (Figure 4.19). Between the bodies, the wires assume the shapes that minimize the potential energy generated by the boundary torques at the bodies. In the absence of external transverse forces, the minimum energy curves for the primary backbone and wires will have constant curvatures [105]. We believe that neglecting thetransverse external forces imposed by the pericardium and epicardium is reasonable over the small distance between the bodies. This constant curvature simplification results in the length of the primary backbone curve (L) being equal to the average of the lengths of the two wires. Additionally, the shape of the primary backbone can be represented by a single bending angle β between the y-axes of the rear and front bodies (Fig. 6). The resulting forward kinematics for the

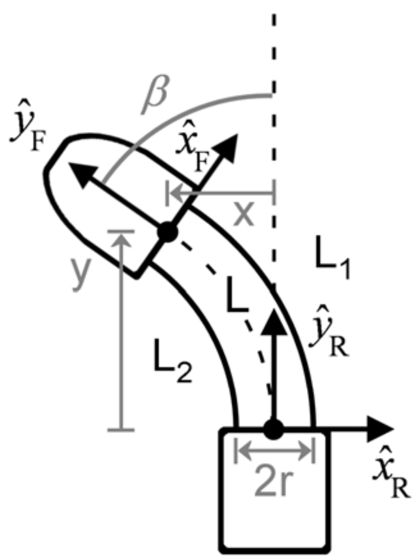

Figure 4.19: Illustration of the front crawler body turning to the left, with kinematic axes and variables shown. The Cartesian location (x, y) of the front body with respect to the rear body is controlled by the wire lengths L1 and L2. The length of the primary backbone L and bending angle β were used to calculate the inverse kinematics.

primary backbone can be determined from geometry as

$$L = \frac{L_1 + L_2}{2}$$
$$\beta = \frac{L_2 - L_1}{2r} \qquad (1)$$

where L_1 and L_2 are the right and left wire lengths, respectively, and $2r$ is the fixed distance between the drive wires.

A geometric evaluation of the Cartesian coordinates of the front body in terms of the length and bending angle of the primary backbone yields the following forward kinematics for the front body position

$$x = \frac{L}{\beta}\left(1 - \cos\beta\right)$$
$$y = \frac{L}{\beta}\left(\sin\beta\right). \qquad (2)$$

Combining (1) and (2) yields the forward kinematics for calculating the front body Cartesian position (i.e., workspace variables) from the wire lengths (i.e., joint space variables)

$$x = \frac{r \cdot \left(L_1 + L_2\right)}{L_2 - L_1} \cdot \left(1 - \cos\left(\frac{L_2 - L_1}{2r}\right)\right)$$
$$y = \frac{r \cdot \left(L_1 + L_2\right)}{L_2 - L_1} \cdot \left(\sin\left(\frac{L_2 - L_1}{2r}\right)\right). \qquad (3)$$

This pair of equations can then be solved for the joint space variables in terms of the workspace variables, yielding the following closed-form inverse kinematic equations:

$$L_1 = -\frac{x^2 + y^2 + 2rx}{2x} \operatorname{arctan2}\left(\frac{-2xy}{x^2 + y^2}, -\frac{x^2 - y^2}{x^2 + y^2}\right) \qquad (4)$$
$$L_2 = -\frac{x^2 + y^2 - 2rx}{2x} \operatorname{arctan2}\left(\frac{-2xy}{x^2 + y^2}, -\frac{x^2 - y^2}{x^2 + y^2}\right).$$

4.7 Sensors

HeartLander uses a suite of onboard and offboard sensors to provide feedback for navigation and gather data from the intrapericardial environment. Load cells within the offboard mechanical transmission measure the forces applied to the drive wires. These data provide a measure of the force required to drive the robot through the intrapericardial space, which directly affects locomotion efficiency. Pressure sensors, also located in the offboard instrumentation, measure the pressure in the suction lines and corresponding suction chambers. These data are used to ensure that the vacuum pressure applied to the epicardium remains at a safe level, and to ensure that suction chambers have a complete seal with the epicardial surface during active prehension. Figure 4.20 shows data recorded from the pressure sensors and load cells during locomotion on a beating porcine heart.

An electromagnetic tracking system (microBIRD, Ascension Technologies, Burlington, VT) is used to measure the position and orientation of the robot in real time, without requiring a clear line of sight with the sensor [107]. This tracking system has been used to track flexible diagnostic catheters inside the body in order to localize sensor readings and register intraoperative and preoperative imaging [108], [109], [110]. The miniature 6-DOF tracking sensor has a 1.3-mm diameter and 8.0-mm length, and is mounted to the front body of the crawler. The magnetic transmitter is attached to the operating table. This tracking system has a translational resolution of 0.5 mm and an angular resolution of 0.1° within our workspace, and a maximum update rate of 68.3 Hz. The tracker data are used by the robot controller during navigation and fine positioning, and also to display the location of the robot on the heart to the surgeon through the user interface. A plot of the position data collected from the microBIRD sensor mounted on the front body of the crawler during locomotion on a beating porcine heart can be seen in Figure 4.20.

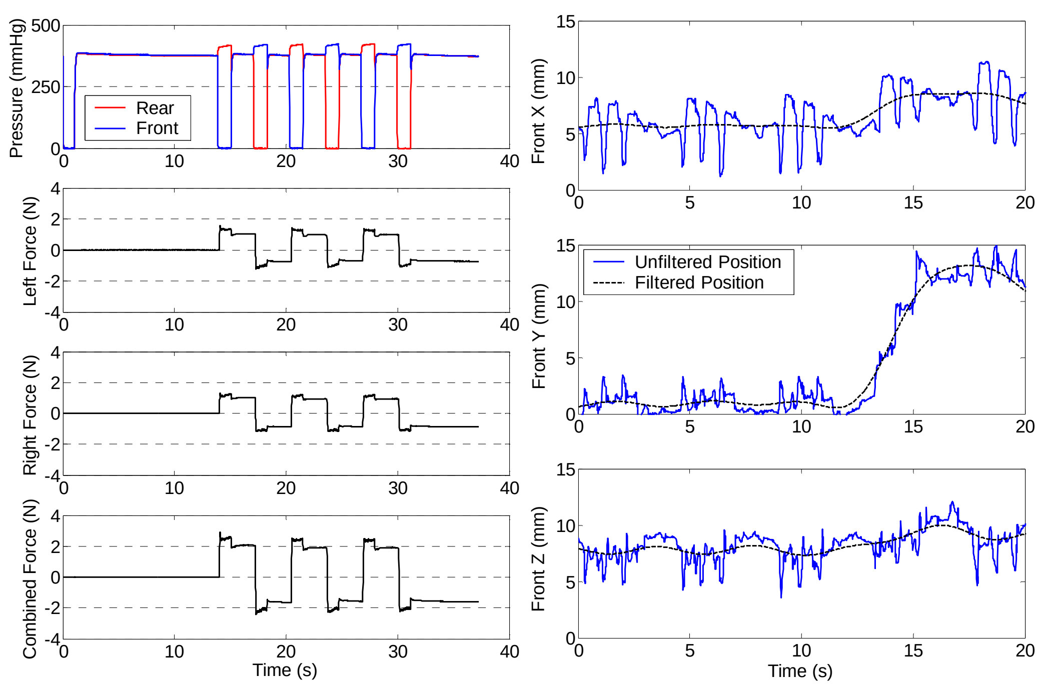

Figure 4.20: (left) Pressure sensor and load cell data recorded during three steps on a beating porcine heart. (right) The raw (*solid line*) and low-pass filtered (*broken line*) 3-D position data collected from the 6-DOF electromagnetic tracking sensor (microBIRD, Ascension Technologies) mounted on the crawling robot during locomotion on a beating porcine heart.

We have also explored the use of flexible fiber optic scopes and CCD cameras to provide direct visualization of the epicardial surface. The video from the CCD camera is displayed directly on a monitor for the surgeon, while the fiber optic images are first digitized by an external video camera before being displayed (Figure 4.21). The FS-066-24 flexible fiber optic scope (ScopeTechnology, CT) had a small diameter of 1.8 mm and included a light guide, but provided insufficient resolution and dramatically increased tether stiffness. To address these issues, we employed a 3.8-mm diameter color CCD camera (Fort Imaging Systems, France). The resolution of this camera is 537(H) x 597(V), which is sufficient for recognition of epicardial landmarks for both navigation and administration of therapy (Figure 4.21). The depth of field is 5-mm to infinity and the field of view is 90 degrees, allowing visualization of the needle tip during puncture and injection. Lighting is provided by two sets of flexible incoherent fiber optic bundles. Although more flexible than the fiber optic scope, the CCD camera still increased the tether stiffness. The camera also required a great increase in the height of the crawler bodies and often overheated due to the confined space within the robot. Although illustrated as a proof of concept, the limitations of both fiber optic and CCD sensors led us to rely completely on the electromagnetic tracking system for localization on the heart. In the future we may consider direction visualization of the epicardial surface as necessitated by the therapeutic interventions.

HeartLander can also be equipped with various diagnostic sensors that measure properties through direct contact with the epicardium. To illustrate this concept, we have mounted a custom bipolar electrode to the bottom of HeartLander to measure the electrical activity of the heart (Section 7.4). Additionally, we have deployed a commercial ultrasound probe through HeartLander to visualize the internal structure of the heart from the intrapericardial space (Section 7.5).

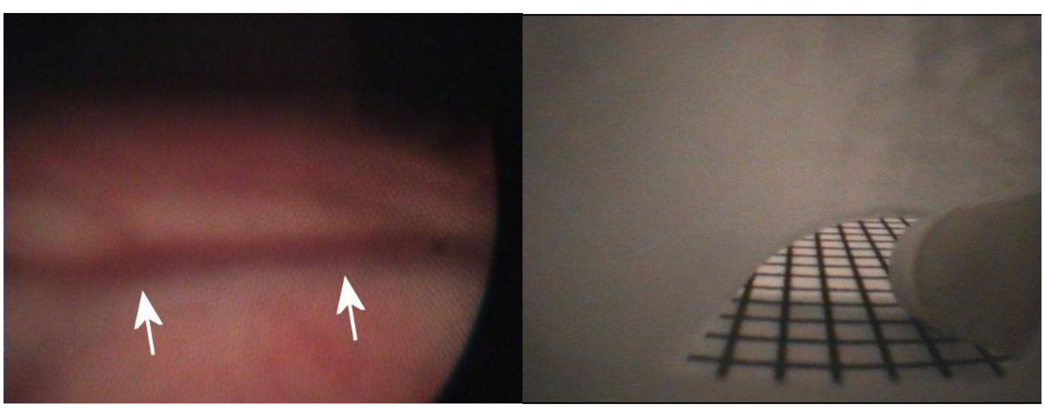

Figure 4.21: (left) View of the left anterior descending artery (LADA) through the flexible fiber optic scope. (right) The view from the CCD camera located on the front body of HeartLander. A grid of 1-mm squares is shown, along with the tip of an implantable pacing lead (*right side*).

4.8 End Effectors

We have designed or adopted commercial therapeutic end effectors for the three intrapericardial therapies initially considered for HeartLander: myocardial injection, epicardial pacing, and epicardial ablation.

4.8.1 Remote Injection System

The remote injection system uses a custom 27G needle that passes through a sheath in the working channel. After the robot reaches the desired epicardial location, the surgeon advances the needle by hand, through the sheath, into the tissue. The depth of the needle puncture is set by the mechanical constraints of the system, such that the needle can extend 3 mm out of the protective needle channel to avoid deep punctures (Figure 4.22). The injection is then performed using a syringe attached to the proximal end of the needle. During locomotion, the needle is safely retracted into the needle channel. This end effector will be useful for the injection of regenerative materials into areas of myocardial infarction. Demonstration of myocardial injection of tissue dye is presented in Chapter 7.

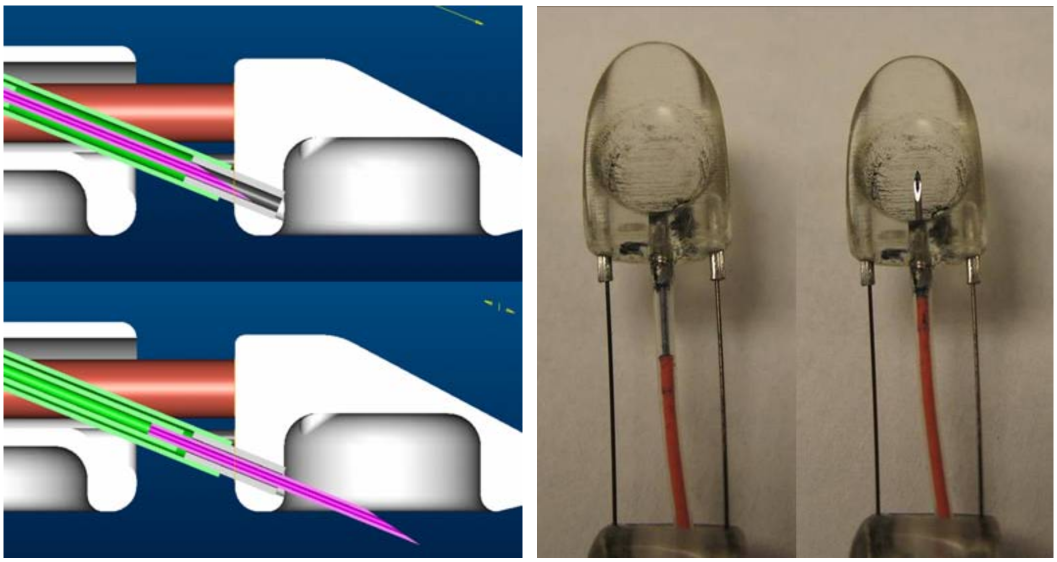

Figure 4.22: (left) CAD images of the remote needle injection system, with the needle retracted and extended. (right) Photograph of the remote needle injection system with the needle retracted and extended.

4.8.2 Lead Placement and Ablation

The remote epicardial lead placement system provides the surgeon a way to advance and engage an FDA-approved implantable lead into the epicardial surface (Flextend™, Guidant, MN) from HeartLander. The lead is advanced toward the epicardial surface under visual feedback (Figure 4.21) using a customized guide wire running through the tether of HeartLander. The lead is then engaged into the epicardial surface using the active fixation mechanism of the device, in the same manner by which the lead is approved to be engaged through an endoscope. The custom guide wire is then remotely detached from the tip of the lead, and HeartLander is manually retracted back over the lead by its tether – leaving the lead engaged with the epicardium. This system could be used to perform left ventricular epicardial lead placement for cardiac resynchronization therapy in patients with congenital heart disease, where open procedures are difficult and dangerous [111]. The preliminary results of a lead placement are described in Chapter 7.

The working channel of HeartLander supports the application of a commercial 5F (1.65-mm diameter) Biosense Webster™ A-type electrophysiology catheter to the epicardial surface of the heart without modification. Chapter 7 describes preliminary testing in an animal model with the chest opened.

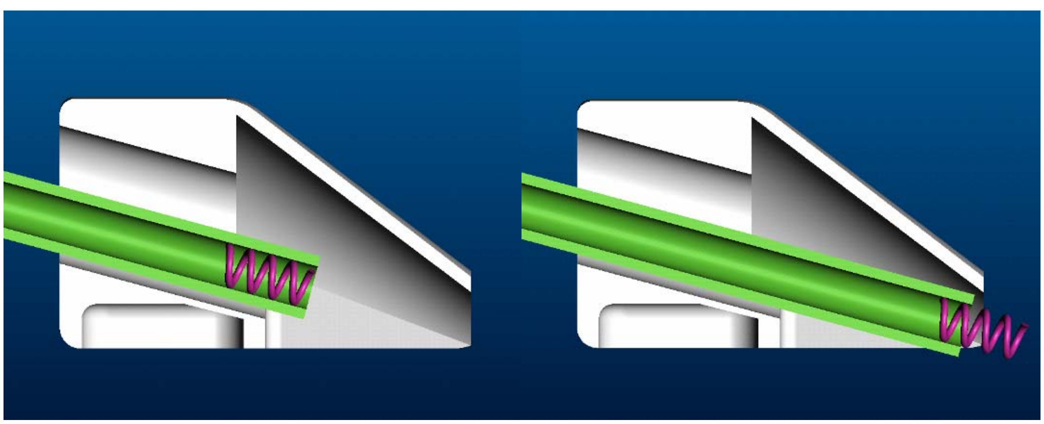

Figure 4.23: CAD images of the modified endocardial active fixation pacing lead in the retracted (left) and extended (right) states. In the extended position, the active fixation lead has also been engaged.

Chapter 5

Control System Design

The HeartLander control system is designed to meet the clinical goal of providing precise and stable access to the entire epicardial surface of the heart. In designing and evaluating the control system, we decompose this goal into two distinct, yet related, tasks: navigation and fine positioning. This chapter motivates the control design specifications, then describes in detail the individual components of the control system. Localization is performed by filtering the robot tracking data to remove the physiological motion, and displaying the position on a static model of the heart surface. The inchworm-like locomotion modality described in Section 4.3 is refined to improve stepping efficiency based on the physiological constraints of intrapericardial environment. Path planning and tracking, which generate navigation, are also tailored to the intrapericardial problem space, and are described in detail. The surgeon interacts with the system through a computer and joystick interface, and is provided feedback of the robot location on the heart as a substitute for direct visualization.

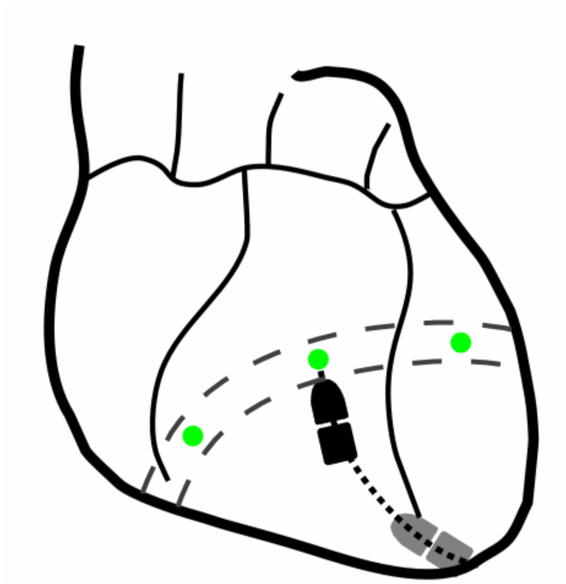

Figure 5.1: Illustration of the navigation task, the initial portion of the general target acquisition decomposition. The robot begins each trial proximal to the apex of the heart, then navigates to the navigation target under semi-autonomous control. The circumference of the ventricles is the region between the broken lines, and three navigation targets are visible in green.

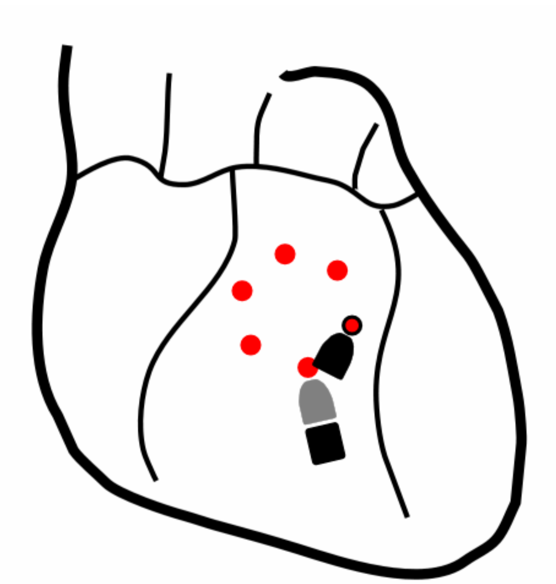

Figure 5.2: Illustration of the fine-positioning task, the final portion of the general target acquisition decomposition. Following navigation to the remote target area, the robot makes a series of small, precise motions to each of the targets within the specified pattern. Six fine-positioning targets are shown in red.

5.1 Control Design Specifications

To facilitate the selected intrapericardial therapies, HeartLander must demonstrate the ability to acquire to a series of targets on the beating heart in a precise and stable manner. The acquisition of any target series with arbitrary size, shape, and location can be decomposed into a navigation task to the general target region (Figure 5.1), followed by fine positioning to each of the local targets within the region (Figures 5.2). This decomposition allows the control system to balance speed and accuracy based on the requirements for each of the navigation and fine-positioning tasks, thus reducing the total task completion time. This is a logical decomposition of the general target acquisition task, but there exist many reasonable alternatives. During the navigation phase to the general target region, the speed with which the robot moves is more critical than the precision of its motions. In the fine-positioning phase, during which the targets are acquired, precision is critical and must take precedent over movement speed. Throughout both the navigation and fine-positioning components of target acquisition, HeartLander must provide a stable platform relative to the heart surface in order to operate safely on the unconstrained epicardium. These experimental criteria of providing semi-autonomous navigation and fine-positioning in a stable manner drove the design and evaluation of the HeartLander control system.

5.2 Localization of the Robot

HeartLander stabilizes itself with the heart by attaching to the epicardium, and passively moving with the heart over the respiration and cardiac cycles. An instrument deployed from HeartLander can safely interact with the portion of the epicardium proximal to the crawler, because it is synchronized with the heart surface motion. Thus, the robot and the epicardium exhibit the same transformations due to the physiological motion of the respiration and heartbeat cycles. These physiological transformations are measured in real time by the tracking sensor mounted on the robot, because the sensor measurements are defined with respect to the stationary magnetic transmitter attached to the operating table. For example, the tracking data will exhibit the underlying physiological motion when the robot is at rest on the surface of the heart (Figure 5.3). For localization, however, we wish to know the position of the robot relative to the heart surface, which changes only as the robot moves over the heart – not with the underlying physiological motion. Accordingly, we will localize the robot with respect to the moving reference frame of the beating heart, rather than the stationary reference frame of the electromagnetic tracking system. With respect to this moving reference frame, the heart surface, the attached robot, and all targets located on the heart surface will be stationary over the physiological cycles. In order to transform the reference frame for the robot tracking sensor from a stationary to a beating-heart reference frame, we filter the underlying physiological motion from the robot tracking sensor in real time. This simulates the effect of mounting the magnetic transmitter to the beating heart, which is not physically possible. The result of this filtering is that the position and orientation of the robot will appear stationary when it is resting on the surface of the beating heart. Additionally, the tracked motion of the robot as it travels over the heart surface will not be superimposed over the underlying physiological motion of the heart (Figure 5.3).

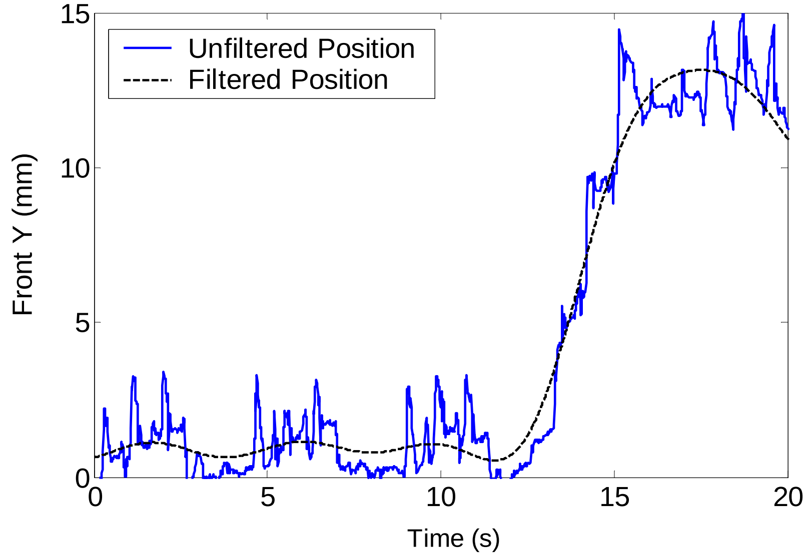

Figure 5.3: The longitudinal axis of the position data from the tracking sensor on the front body of the robot crawler on a beating porcine heart. The robot is at rest for the first 12 seconds, then takes a step forward. The underlying physiological motion of the respiration (lower frequency) and the heartbeat motion (higher frequency) can be seen in the unfiltered data (solid line), but has been largely removed from the filtered data.

For localization, the surface of the heart – as well as targets located on the heart surface – must also be defined with respect the same moving reference frame on the beating heart. These objects will appear stationary over the physiological cycles, and are described in detail in Sections 5.4 and 5.7. In this manner, the control problem reduces to that of a crawling robot traveling to stationary targets over a stationary surface. This simplification is only possible because the robot moves with the epicardium, and is thus located within the reference frame of the beating heart. The remainder of this section provides the details of the filtering techniques used to remove the physiological motion from the robot tracking system in real time.

5.2.1 Filtering Robot Tracking Data

During porcine testing, the animal is placed under general anesthesia and mechanically ventilated, while the heart is left to beat freely without the aide of anti-arrhythmic drugs. The respiration rate of the animal is adjusted within the range of 12 – 16 respirations per minute (rpm) or 0.2 – 0.27 Hz to maintain an appropriate level of carbon dioxide in the blood. The respiration rate for humans is typically in the lower end of that range. The range of heart rate for a pig is 68 – 90 beats per minute (bpm) or 1.13 – 1.5 Hz. The heart rate range for humans also overlaps within the lower end of that range.

Initially, we used a third-order Chebyshev Type II low-pass filter with a stopband cutoff of 20 dB at a frequency of 0.2 Hz to remove all physiological motion from the tracking data in real time (Figure 5.4). Because locomotion over the heart surface is reduced to a 2-D problem within the intrapericardial space, we are primarily concerned with the physiological motion within the plane tangential to the heart surface (i.e., the transverse plane of the robot). In order to quantify the physiological motion attenuation provided by the filter, we first transform the tracker data from the magnetic transmitter reference frame to that of the robot adhering to the heart surface. In this manner, the x- and y-axes form the plane that is tangential to the surface of the heart, while the z-axis is normal to the surface of the heart. The low-pass filter with a cutoff of 0.2 Hz was shown to reduce the tangential component of the physiological motion 85 % from 7.3 ± 1.2 mm to 1.1 ± 0.5 mm. Although this level of attenuation is sufficient to achieve the desired positioning accuracy for our sample therapies, the filter also introduced an undesirable 5 s delay in the tracker data. This delay is apparent in Figure 5.5, when the robot takes a step after an initial 30 s resting period.

To address this filter delay, we implemented a series of filters consisting of a low-pass filter and two notch filters. First, a third-order Chebyshev Type II low-pass filter with a stopband cutoff of 20 dB at a frequency of 1.0 Hz is used to remove the heartbeat motion from the tracking data. This filter is able to attenuate the heartbeat motion despite the frequent fluctuations in heart rate, while introducing a much smaller delay than the same filter with a frequency cutoff of 0.2 Hz. To remove the respiration component of the physiological motion, we then use a series of two second-order IIR notch digital filters, with notch frequencies at the primary (0.23 Hz) and secondary harmonics (0.46 Hz) of the respiration rate. Notch filters are appropriate for this task, because the respiration rate is precisely controlled by the ventilator. The first harmonic notch filter was designed to have a narrow bandwidth of 0.0067 Hz at an attenuation level of -3dB, in order to avoid attenuating the robot motion with a nearby frequency of 0.25 Hz. The notch of the second harmonic filter was widened to 0.13 Hz at an attenuation level of -3dB. The individual frequency responses that combine to form this filter set can be seen in Figure 5.6. This filtering method attenuated the tangential physiological motion 81 %, from 7.3 ± 1.2 mm to 1.4 ± 0.5 mm. The delay caused by this filter was 1 s, which is significantly shorter than that of the low-pass filter previously used to remove both respiration and heartbeat motion (Figure 5.7). This second filtering method achieved an acceptable level of attenuation of the physiological motion, with an acceptable delay in the tracking data. The initial low-pass filtering method was used in early porcine testing, such as the navigation study presented in Section 6.2. The superior combination filter comprised of low-pass and notch filters was used in the more recent porcine testing presented in Sections 6.1 and 6.3. The amplitudes of the physiological motion before and after each of the filtering techniques over a range of locations on various porcine hearts are presented in Table 5.1. The physiological motion is decomposed into the lateral, longitudinal, normal, and tangential components.

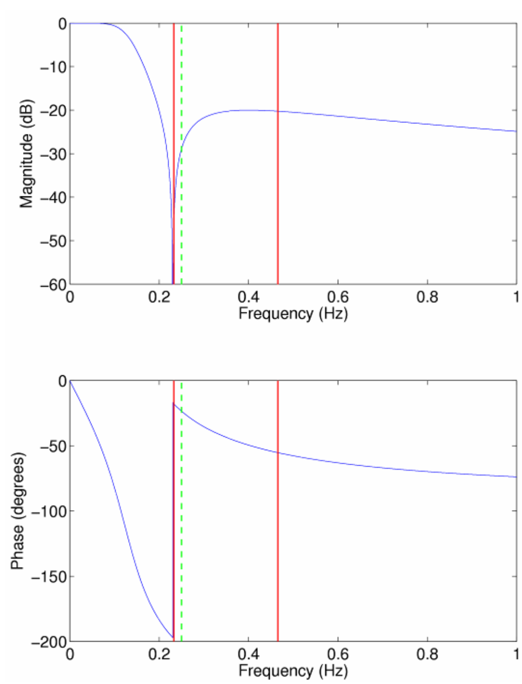

Figure 5.4: Plots of the magnitude and phase of the frequency response of the initial low-pass filter used to remove the physiological motion from the robot tracker data. The filter is a third-order Chebyshev Type II low-pass filter with a stopband cutoff of 20 dB at a frequency of 0.2 Hz. The primary and secondary respiration frequencies are shown by solid vertical lines, while the robot locomotion frequency is shown by the broken line.

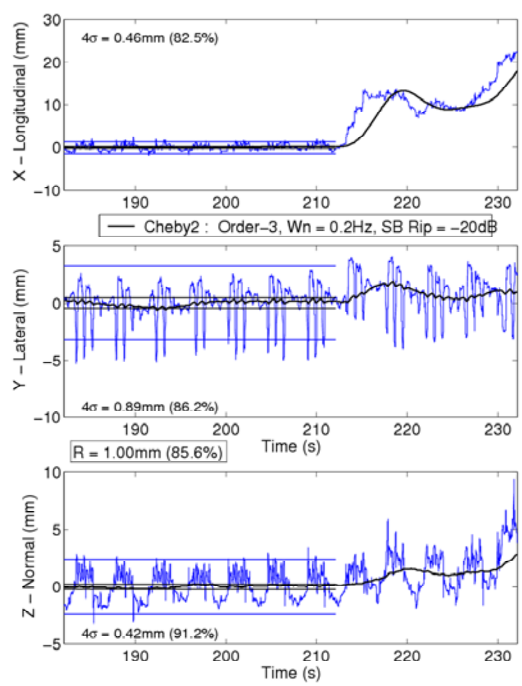

Figure 5.5: The raw and filtered tracker data during robot locomotion on a beating porcine heart. The initial 30 s show isolated physiological motion while the robot is a rest. As the robot takes a step, the physiological motion is superimposed over the robot motion in the raw data. The third-order Chebyshev Type II low-pass filter with a stopband cutoff of 20 dB at a frequency of 0.2 Hz removes 85% of the physiological motion, but introduces a significant delay of approximately 5 s.

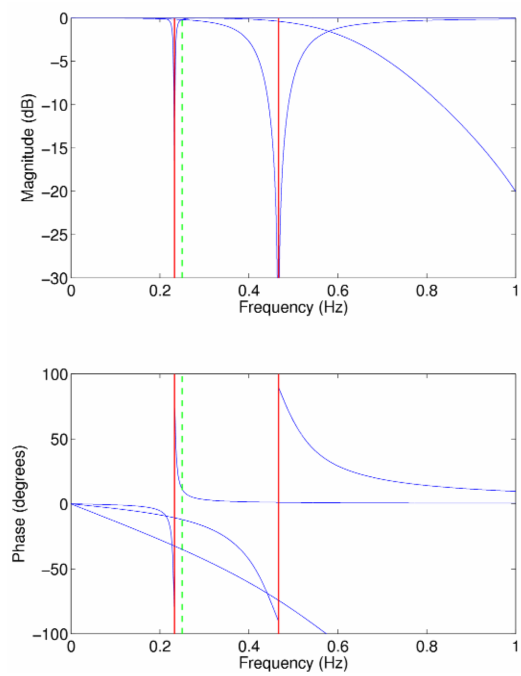

Figure 5.6: Plots of the magnitude and phase of the frequency response of the combined low-pass and notch filter used to remove the physiological motion from the robot tracker data. A third-order Chebyshev Type II low-pass filter with a stopband cutoff of 20 dB at a frequency of 1.0 Hz is first used to remove the heartbeat motion. Two second-order IIR notch filters with notch frequencies at the 0.23 and 0.46 Hz are then used to remove the first and second harmonics of the respiratory motion. The heartbeat and respiration frequencies are shown by solid vertical lines, while the robot locomotion frequency is shown by the broken line.

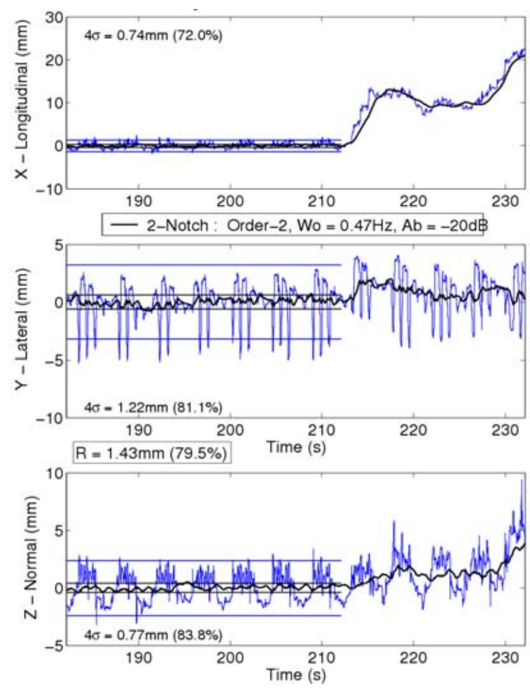

Figure 5.7: The raw and filtered tracker data during a trial with 30 s of resting data on a beating porcine heart, followed by robot locomotion. The data was filtered with a combined low-pass and notch filter. This filter removes 81 % of the physiological motion, and introduces a reasonable delay of approximately 1 s.

Table 5.1: The amplitude of the physiological motion of beating porcine hearts along the primary robot axes and plane tangential to the heart. These data were collected over five porcine studies, with locations spanning the circumference of the heart. The resultant motion within the tangential plane provides a measure of the physiological motion that must be overcome by HeartLander to safely interact with the surface of the heart. The residual physiological motion along these axes after the application of the two filtering techniques described in Section 5.2 is also shown.

Trial	Location	Unfiltered Data				Low-Pass Filter (0.2Hz)				Low-Pass + 2-Notch Filter			
		Long.	Lat.	Norm.	Tang.	Long.	Lat.	Norm.	Tang.	Long.	Lat.	Norm.	Tang.
15-1	anterior	2.7	3.1	4.2	4.1	0.4	0.8	0.4	0.8	0.7	0.9	0.8	1.2
15-9	left-lateral	7.1	4.6	2.7	8.5	0.7	0.7	0.3	1.0	0.5	0.9	0.5	1.0
15-11	posterior	8.3	4.2	5.3	9.3	0.9	0.7	0.6	1.1	0.7	0.7	0.8	1.0
15-12	right-lateral	5.5	2.5	5.5	6.0	0.9	0.7	0.6	1.2	0.8	0.9	0.6	1.2
16-1	anterior	2.6	6.4	4.8	7.0	0.5	0.9	0.4	1.0	0.7	1.2	0.8	1.4
16-8	left-lateral	4.6	3.3	4.5	5.7	0.8	1.2	0.8	1.5	1.0	1.4	1.0	1.7
16-10	right-lateral	8.4	4.7	2.7	9.6	1.9	1.2	1.0	2.2	2.5	1.4	1.0	2.8
16-16	posterior	6.5	5.4	6.5	8.5	0.8	1.4	0.7	1.6	0.7	1.5	0.7	1.7
17-1	anterior	4.3	4.6	10.8	6.3	0.4	0.2	0.6	0.5	0.9	0.6	1.2	1.1
17-4	left-posterior	10.4	4.1	3.4	11.5	0.7	0.6	0.3	0.9	1.4	0.9	0.7	1.7
17-6	left-anterior	2.7	4.7	9.2	5.5	0.4	0.4	0.6	0.5	0.6	0.9	1.3	1.1
18-1	anterior	3.8	3.6	4.9	5.2	0.7	0.5	0.7	0.5	1.1	1.1	1.3	1.5
19-2	left-lateral	3.7	4.9	1.6	6.1	1.5	0.4	0.2	1.6	0.5	0.5	0.3	0.7
19-3	posterior	6.7	7.1	2.5	9.7	0.9	1.2	0.3	1.5	0.6	0.8	0.4	1.0
mean		5.5	4.5	4.9	**7.3**	0.8	0.8	0.5	**1.1**	0.9	1.0	0.8	**1.4**
std		2.4	1.2	2.6	**2.2**	0.4	0.4	0.2	**0.5**	0.5	0.3	0.3	**0.5**

5.3 Locomotion

The coordination of the inchworm-like locomotion of HeartLander is handled by the low-level controller, and is thus transparent to the physician. As described in Section 4.3, the motion is generated by extending the front body with the rear body locked to the epicardium, then advancing the rear body after switching the epicardial grip to the front body. When the efficiency is 100 %, the robot advances by one step length over each locomotion cycle. In the confined and volatile intrapericardial environment, however, the body with suction grip of the epicardium often slips somewhat, resulting in lower locomotion efficiency. To improve this efficiency, we have conducted bench tests to determine the effect of extension speed on the traction of the suction pads. We have also designed a control method in which the tracking sensor data is used coordinate the locomotion timing of the robot with the respiration cycle. These efforts are described in the next two subsections.

5.3.1 Stepping Speed

This study was an attempt to investigate the effect of varying the extension speed on the traction generated by the HeartLander suction pads on the epicardium [103]. Our testing setup measured the force applied to a gripper pad adhering to excised ovine (sheep) epicardial tissue. The gripper pad was pushed until it lost traction and began to slide across the epicardial surface. Video was recorded in order to track the pad and tissue during the extension. By synchronizing the force and video data, we were able to reliably determine the point at which the pad lost traction and began to slip during the extension. This maximum force prior to slip was the evaluation criteria by which the stepping speed was evaluated. Increasing the extension speed up to 20 mm/s resulted in a corresponding increase in traction (Figure 5.8). Increasing the vacuum pressure also improved the traction, but the magnitude of the effect was less than the improvement gained from increasing extension speed (Figure 5.8). These results indicate that an extension speed of 20 mm/s generates the highest traction force for the suction pad locked to the epicardium during a stepping motion.

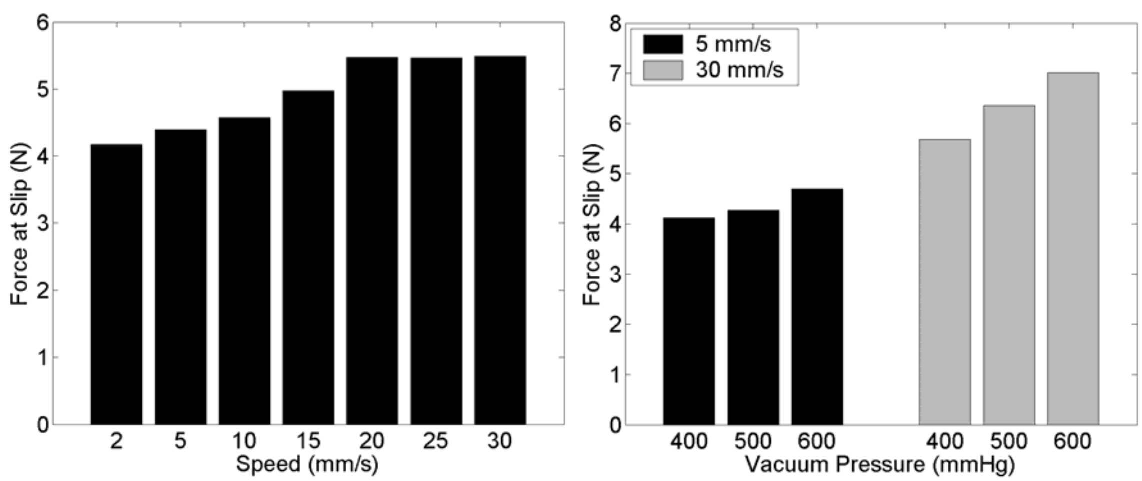

Figure 5.8: (left) The forces recorded at the loss of traction over a range of extension speeds with an open gripper pad and vacuum pressure of 400 mmHg. (right) The forces recorded at loss of traction over a range of vacuum pressures with an open gripper pad, and two different extension speeds.

5.3.2 Step Coordination with Respiration

In an attempt to further improve locomotion efficiency, the timing of the locomotion mechanics is coordinated with the phase of the respiration cycles. As mentioned in Section 3.1.3, the intrapericardial pressure varies approximately 2 to 6 mmHg over the respiration cycle [64], [65]. We propose that this fluctuation in intrapericardial pressure directly affects the normal force, and thus the friction force, imposed on HeartLander by the pericardium. This hypothesis has been supported by video evidence recorded with the chest closed, in which the tightness of the pericardium over the robot appears to vary with the respiration cycle. The underlying physiological reason for this pressure fluctuation may be that the heart moves in the anterior direction (toward the sternum) as the lungs fill with air during inspiration, causing the pericardium to be drawn more tightly over the anterior surface of the heart due to its attachment to the diaphragm. Additionally, the increased lung volume following inspiration likely exerts more external pressure on the surface of the heart.

In light of these considerations, we have coordinated the HeartLander locomotion to take steps only following expiration, when the lungs occupy the smallest volume. Although the respiration cycle can be accurately measured with a mass airflow sensor, such as the AWM700 (Honeywell, Freeport, Illinois), we estimate this information using the existing electromagnetic tracking system located on the front body of the crawling robot. During inspiration, the heart translates in the negative z-direction; i.e., in the anterior direction, toward the sternum. During expiration, the heart translates in the positive z-direction; i.e., in the posterior direction, toward the spine. Figure 5.9 shows a typical measurement of this motion recorded from a beating porcine heart in situ, where the oscillations due to heartbeat (higher frequency) and respiration (lower frequency) are visible. Using the onboard tracker data to estimate the respiration cycle obviates the addition of another sensor, and directly measures the property that we believe contributes to the intrapericardial pressure fluctuation: the antero-posterior (A-P) translation of the heart.

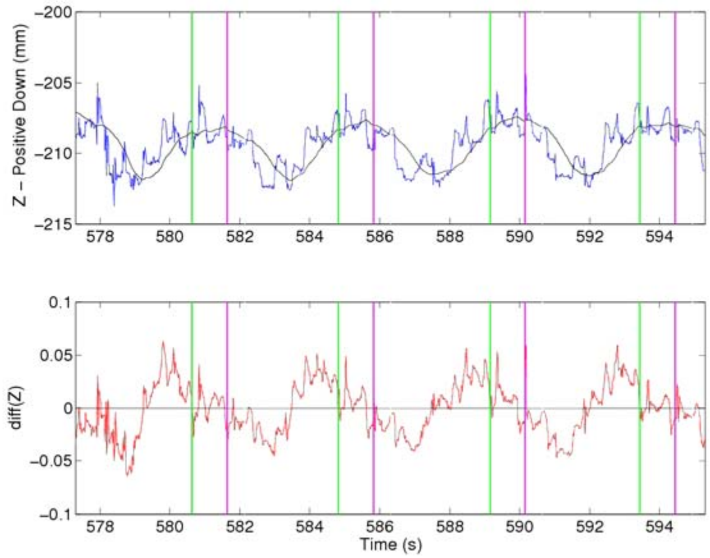

Figure 5.9: (*upper*) The antero-posterior (A-P) translation of the robot resting on the surface of a beating porcine heart over four respiration cycles. The heartbeat motion (higher frequency) has been removed from the filtered data with a low-pass filter. The heart moves in the anterior direction (negative z) during inspiration, and in the posterior direction (positive z) during expiration. We hypothesize that stepping during the pause following the expiration motion will result in improved locomotion efficiency, and therefore must detect the end of the expiration motions in real time. (*lower*) The A-P velocity for the filtered translation data in the upper plot. The end-expiration events can be detected in real time (green vertical lines) by finding the zero-crossings that occur immediately after the data was positive for at least 1 s. This method correctly identified end-expiration events in 91 % of the respiration cycles in 800 s of data tested offline to validate the method. The ideal stepping regions are between each pair of green and magenta vertical lines.

Reviewing the tracking data with HeartLander adhering to various locations around the circumference of the beating porcine heart revealed that this A-P translation of the heart over respiration is independent of the location of the robot on the heart. To take advantage of the portion of the respiration cycle during which the heart is in its most posterior location and the lungs occupy the smallest volume, stepping is performed during the resting period following the expiration motion. This resting period between the end of expiration and the beginning of inspiration lasts approximately one quarter of the total respiration cycle. For a respiration rate of 14 breaths per minute (0.23 Hz), the end-expiration rest lasts approximately 1 s. Accordingly, the control system must detect the end of the expiration motion, and trigger a step that will be completed by the start of inspiration.

To detect the end-expiration (EE) phase of respiration, we monitor the velocity of the A-P tracking data with the heartbeat motion removed using a low-pass filter with a cutoff frequency of

1.0 Hz, as described in Section 5.2. The EE motion can be detected by finding the first zero-crossing in the A-P velocity that immediately follows the peak associated with the expiration motion (Figure 5.9). To avoid misclassifying zero-crossings due to noise as EE events, we require that the velocity remain positive for a minimum duration of 0.6 s prior to the detection of an end-expiration event. This inherently requires that an expiration motion immediately precede each EE event, which is logical. This detection method was applied to a library of over 800 s of data with HeartLander attached to various locations around the porcine heart. The results were 177 correct EE classifications (91.2%), 7 false-positives (3.6%), and 10 false-negatives (5.4%). False-negatives result in the control system missing an opportunity to take a step until the next respiration cycle, and are therefore not of great concern as long as the occurrence rate is reasonably low. The error rate of 3.6% for the false-negatives, which would result in stepping during the suboptimal phase of respiration, was considered acceptable.

The duration of the extension or retraction stepping motion must remain less than 1 s in order to complete the motion prior to the onset of inspiration. To test this hypothesis, we calculated the percentage of stepping motions that would have been completed (in simulation) prior to inspiration for the previously mentioned library of 800 s of resting data. This simulation was performed over a discrete range of stepping durations from 0.25 to 2.0 s. Figure 5.10 shows the average percentages of the steps that fell within the EE resting period over the step duration range. A maximum step duration of 1.0 s was selected because it permitted enough time for a reasonable step length, while maintaining over 95% of the step within the EE rest period.

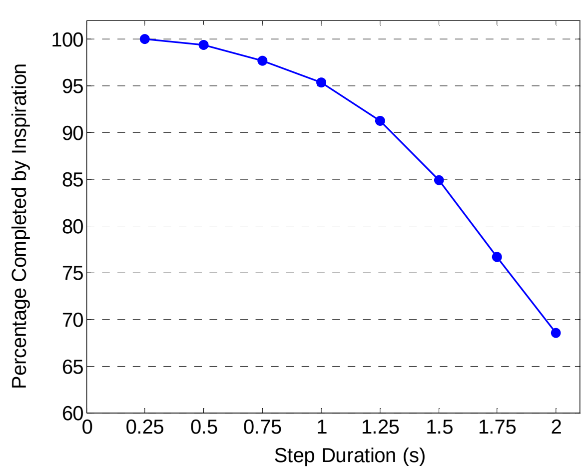

Figure 5.10: The average percentage of stepping motion completed prior to the onset of inspiration for a range of step durations using 800 s of offline data recorded during porcine testing.

5.4 Controller Overview

In order to meet the different requirements of the navigation and fine-positioning components of general target acquisition, the control system has two operational modes. Switching between the control modes balances the tradeoff between speed and accuracy based on the requirements of the task. The navigation mode is used to quickly deliver the robot to the general target vicinity, while the fine-positioning mode is used to precisely acquire the individual targets within the pattern. Targets for both the navigation and fine-positioning tasks are defined with respect to the moving reference frame of the beating heart, in the same manner as the robot tracking data. Accordingly, the locations of the targets do not vary over the respiration or heartbeat cycles, and thus appear as stationary points in space. The 3-D locations of the targets are defined in the coordinate system of the electromagnetic tracker, and thus are properly registered to the robot tracker data. A diagram of the control system architecture for HeartLander can be seen in Figure 5.11.

A circular boundary – originating from the projection of navigation target into the transverse plane of the robot – separates the regions to which the control modes are assigned. (Figure 5.12). As mentioned in Section 4.6, all kinematics are considered only within the transverse plane of the robot. The circular control boundary has a radius equal to the single step length of the robot. When the robot is outside of this boundary, navigation proceeds along the path, without accounting for the filtering delay in the tracking data. This allows the robot to move to the general target vicinity rapidly. The error in the robot localization due to the filtering delay is ignored during navigation because the target will not be acquired in this control mode, making position accuracy less critical.

After the robot crosses the control boundary, the control system enters the fine-positioning mode. The front body of the robot is then maneuvered directly to the current target projection, using the inverse kinematics, until the target is acquired within the distance specified by the surgeon. In this second control mode, the accuracy of the robot localization with respect to the target is critical. After each motion of the front body toward the target, the control system pauses to account for the filter delay before updating the robot localization from the tracker data. If the target was not acquired during the previous motion, subsequent adjustments of the front body are made until the target is acquired within the specified distance. In this manner, the robot makes a series of fine-positioning motions, rather than full steps involving motion of the rear foot. This scheme also allows the acquisition of multiple local targets in minimal time.

The semi-autonomous design of the controller keeps the high-level commands under the control of the surgeon, while managing the underlying control mode selection, path following, and actuator commands. Both control modes proceed as long as the surgeon advances the joystick. The surgeon also determines which target from the pattern is the initial target for navigation, and the order of the target acquisitions in the fine-positioning mode. We believe that keeping the surgeon actively involved in the therapy planning and execution will both ease the adoption of the technology and take advantage of user expertise. Additionally, the surgeon has the option to execute hard-coded, open-loop locomotion commands (e.g., walk straight, turn left) that override the semi-autonomous controller. These open-loop commands are available in case the surgeon desires more direct control over the actions of the robot in a particular situation.

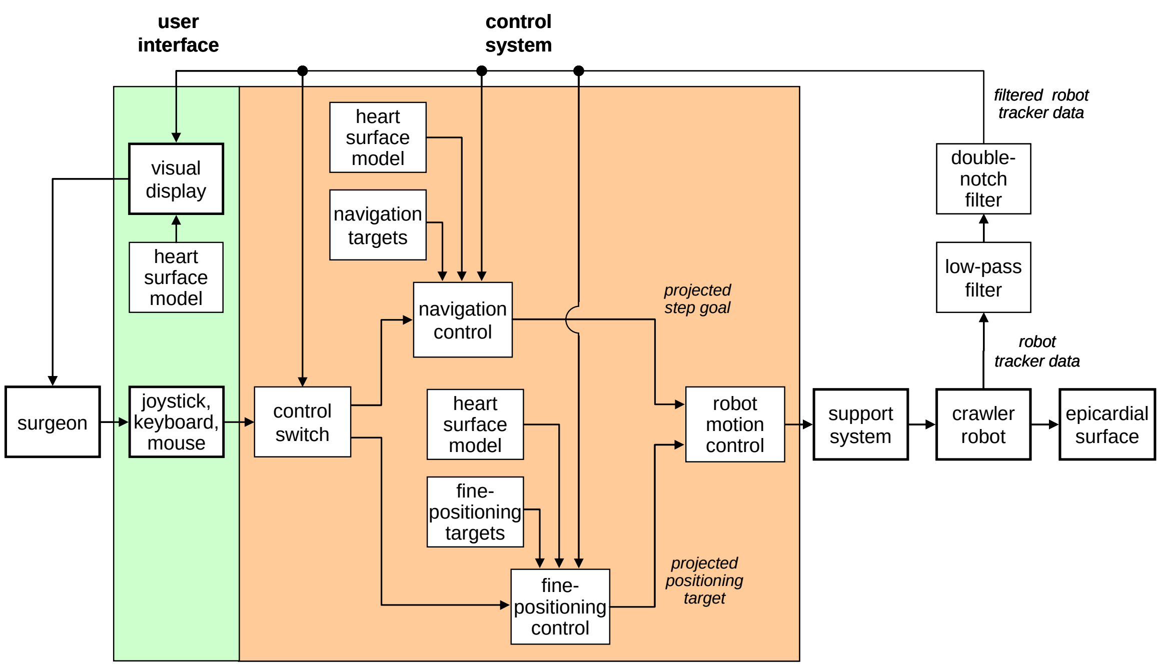

Figure 5.11: Control architecture for the HeartLander system. The control system generates semi-autonomous target acquisition using input from the surgeon through the user interface and feedback from the robot tracking sensor. Based on the distance of the robot from the target, the control switch will select the appropriate control mode: navigation or fine positioning. Both the navigation and fine-positioning control modes use the 3-D location of the current target, the heart surface model, and feedback from the robot tracking sensor to guide the robot toward the current target. Each control mode is tuned to balance speed and accuracy. The robot motion controller generates the lower-level commands to move the robot based on the desired motions passed from the higher-level controllers.

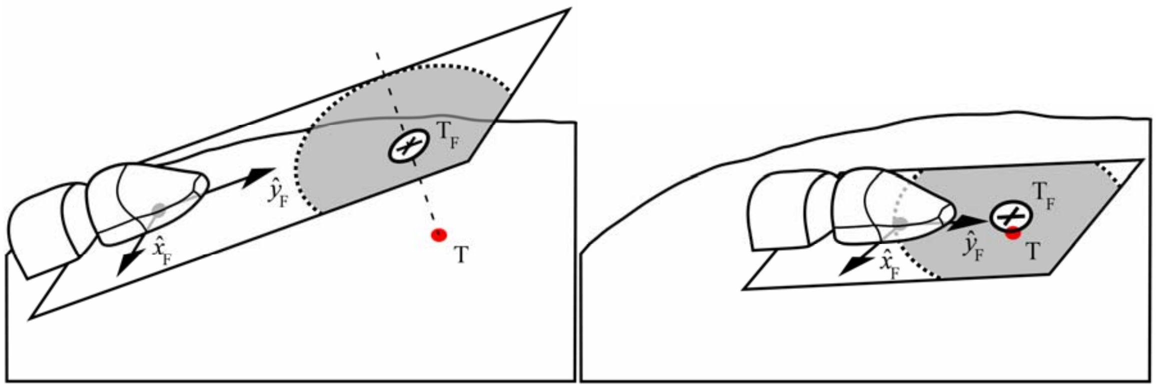

Figure 5.12: Illustration of the target being projected into the transverse plane of the robot during navigation. The white circle shows the target acquisition region, while the light gray circle shows the control mode boundary between navigation and fine positioning. Note that when the robot is far from the target (left), the error cause by projection into the transverse plane is larger then when the robot is close to the target (right). This is due to the curvature of the heart.

5.5 Path Planning

At the start of a target acquisition trial, the control system generates a path that begins at the apex of the heart and ends at the navigation target selected by the surgeon. In the case of a multiple target acquisition, the surgeon generally selects the initial target to be the one that is closest to the apex and located along the approximate midline of the target pattern. This selection method places the target pattern in front of the robot following navigation, thus improving the chance that all targets can be acquired without additional navigation episodes. If multiple target patterns must be acquired at distant locations on the heart, the robot is returned to the apex and the aforementioned process is repeated for each pattern. Generating a direct path from the apex to the navigation target over the heart surface represents the optimal trajectory based on the heuristic of minimizing the curvature and potential energy of the tether. This heuristic is used because the tether exerts a significant external force on the rear body when held in tortuous configurations, and these forces can adversely effect the accuracy of fine positioning. As can be seen in Figure 3.4, direct paths can be used to reach any target on the epicardial surface of the heart from the apex, because the intrapericardial space is a single continuous volume.

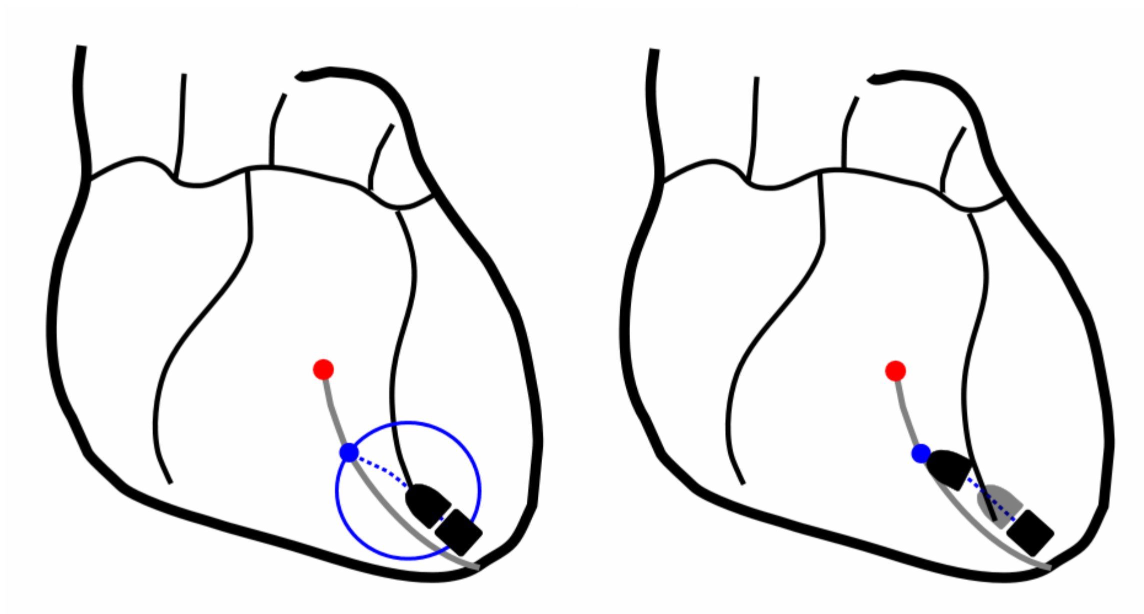

Figure 5.13: An illustration of the path tracking component of navigation. (left) The goal point for the current step is selected as the point along the path (shown in gray) that is one “lookahead distance” from the current location of the robot. The lookahead distance is the radius of the circle, and the goal point is the intersection of this circle with the path (shown by the dot). (right) The front body of the crawler is moved to the goal point for the current step, and the process is repeated until the robot reaches the target.

5.6 Path Tracking

The path tracking component of the navigation controller defines the manner in which the robot follows the path from the apex to the initial navigation target. Specifically, the path tracker selects an intermediate point along the path as the goal point for the current step, plans a trajectory to the goal point, and issues the corresponding actuator commands. Path tracking is accomplished using pure pursuit [112], which is widely used in mobile robot path tracking, and has been shown to outperform numerous other control theory approaches and polynomial fitting approaches under various conditions [113]. Predictive [114], adaptive, and feedforward [115] variations of classical pure pursuit exist, but these more sophisticated methods deal with problems that arise in continuous, high-speed applications. Simple pure pursuit is a reasonable selection for this application because HeartLander makes discrete motions at relatively low speeds along paths with low curvature. The pure pursuit algorithm calculates the constant steering angle that delivers a car-like vehicle from its current location to the goal point [112]. This task is geometrically similar to our path tracking task because the HeartLander crawler moves along arcs of constant curvature at each step. The goal point is selected as the intermediate point along the path that is located a specified distance from the current robot location (Figure 5.13). This distance is called the *lookahead distance*, and is the single parameter that can be adjusted to modify the path following behavior of pure pursuit. If the lookahead distance is small, the robot will tightly adhere to the path, but may oscillate about curves depending on the speed of the robot. If the lookahead distance is large, on the other hand, the robot will smoothly follow the path without oscillation, but may cut off sharp corners. The value of the lookahead distance is specific to the tracking strategy, and therefore cannot be optimized in the general case. We currently set the lookahead distance to be equal to the single step length of the robot – the maximum distance that can be traveled in a single step – because we do not anticipate high path curvatures.

After the goal point has been determined, the path tracker calculates the actuator commands to generate the desired motion of the front body to the goal point (Figure 5.13). The path tracker uses the estimation of the front body location from the filtered robot tracking sensor to transform the goal point into the reference frame of the robot. The inverse kinematics (4) are then used to calculate the drive wire lengths between the bodies that will move the front body to the goal point. After the current step is complete, the next goal point is found and navigation continues until the robot enters the fine-positioning control mode near the initial navigation target.

5.7 User Interface

Prior to each study, an approximate surface model of the porcine heart is generated for the display. The surgeon first traces the epicardial surface of the beating heart with a probe, which has an electromagnetic tracking sensor fixed to the distal tip, in order to generate a 3-D point cloud of the heart surface. The perimeters of 2-mm coronal slices of the point cloud are then segmented by hand for the entire heart. A 3-D convex hull is fit to the segmented heart surface points using the software package Matlab™. Figure 5.14 shows the point clouds, wire frame model, and rendered surface model generated for a porcine heart. This technique of generating the surface model of the heart does not take into account the heartbeat or respiratory motion during the tracing task. Accordingly, the point cloud, and corresponding surface model, represent the approximate average position of the heart over the physiological cycles. No anatomical landmarks are currently represented on the surface model. Similar to both the robot localization and the definition of the targets, the heart surface model is defined with respect to the moving reference frame of the beating heart. Accordingly, the model is stationary. Furthermore, because the positions heart surface tracings, from which the model is derived, are measured with respect to the electromagnetic tracking system, the model is properly registered to both the robot tracking data and the targets.

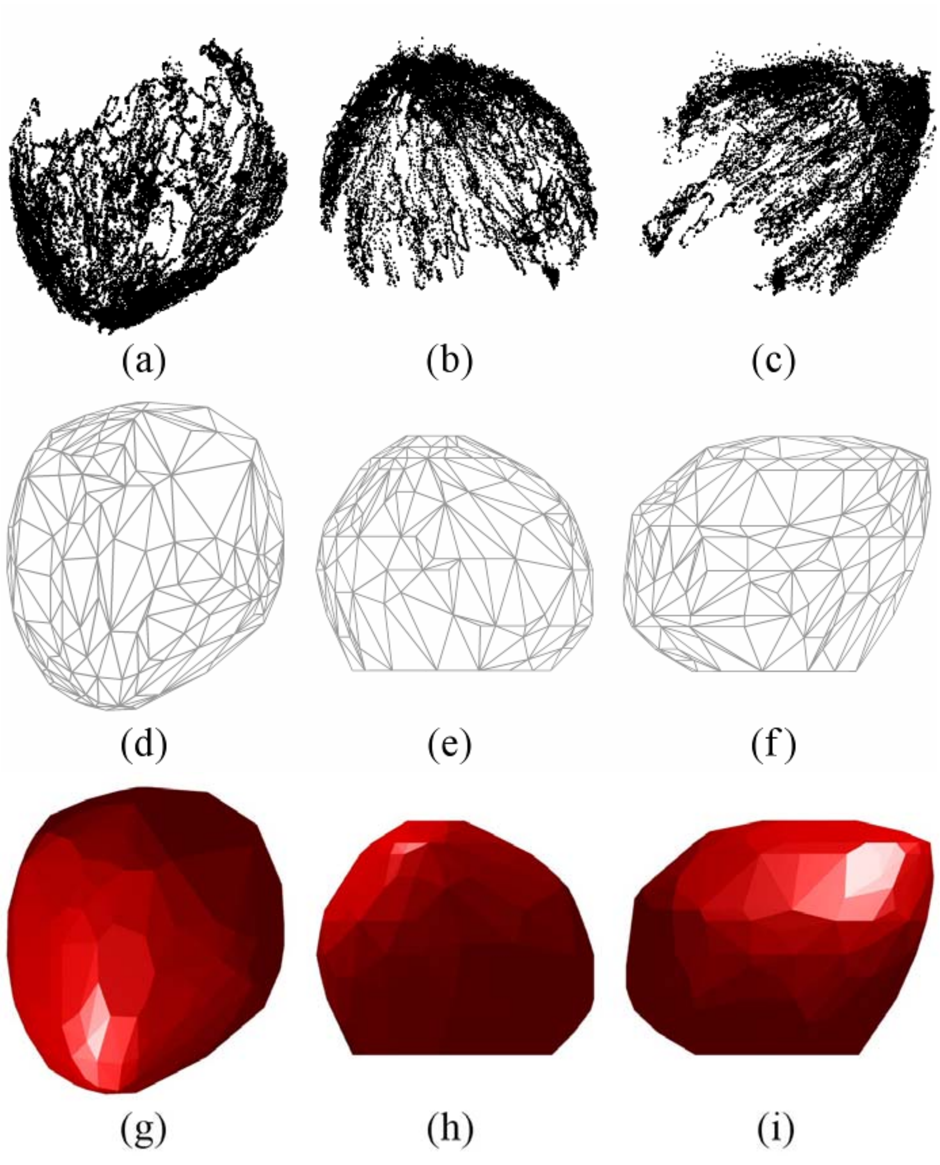

Figure 5.14: A sequence of images showing the generation of the heart surface model for the surgeon's graphic display. A point cloud (a-c) is first generated by the surgeon by tracing the beating heart with a tracker probe. A wire frame surface model (d-f) is then generated by fitting a convex hull to the hand segmented perimeters of the point cloud. Lastly, Matlab™ is used to create a rendering of the wire frame model as a solid object with lighting (g-i).

For both the navigation and fine-positioning tasks, the surgeon views a graphical display of the robot and target positions on the heart. During the navigation task, the path generated by the robot is also shown (Figure 5.15). The surgeon uses the display to select the current target, and monitors the progress of the acquisition. This display is the only form of visualization during the porcine testing in vivo because the closed chest and intact pericardium make direct visualization difficult.

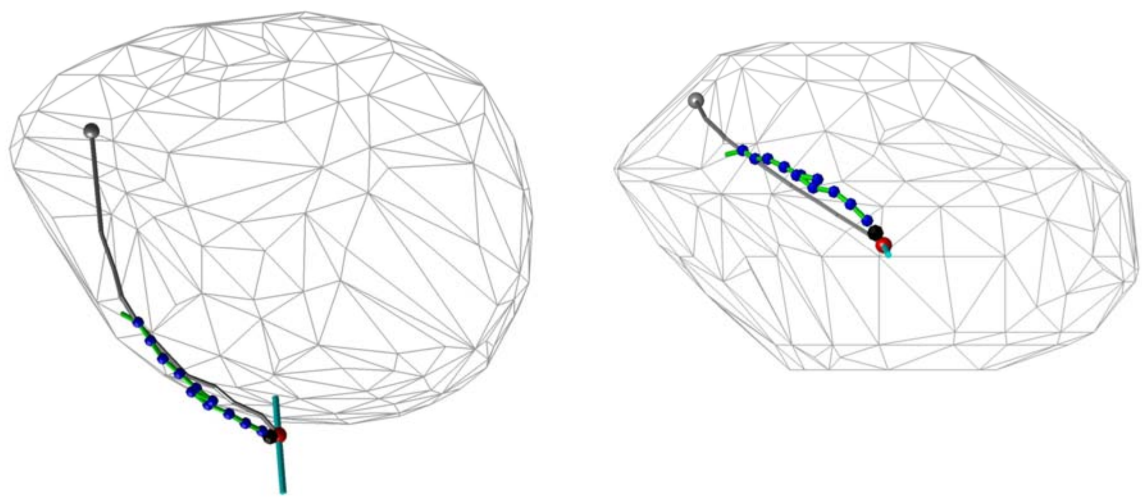

Figure 5.15: Screenshots showing two views of a navigation trial from the graphic display. The ideal path (*dark gray*) and true robot path (*light gray with black way points*) can be seen. The current robot location (*large black sphere*) overlaps the target location (*large gray sphere*), and thus they are difficult to differentiate.

Chapter 6

Robotic System Evaluation

To perform the intrapericardial therapies envisioned for HeartLander, the robot must demonstrate the acquisition of a series of targets on the beating heart in a precise and stable manner. The acquisition of a target series with arbitrary size, shape, and location can be decomposed into a navigation task to the general target region, followed by fine-positioning to each of the local targets within the region. This decomposition is reflected within the control system to meet the different requirements for each of the navigation and fine-positioning tasks, and will also be reflected in the evaluation presented in this chapter.

We evaluated the performance of the HeartLander system through a series of studies using a beating porcine model with the chest closed and pericardium intact. This chapter describes the experimental protocols and results from these studies that demonstrate successful navigation, fine positioning, and stability. This demonstration of precise and stable access, complemented by the results from the therapy feasibility studies presented in Chapter 7, validate that HeartLander can be used as a delivery platform for intrapericardial therapy.

6.1 Animal Preparations

Healthy Yorkshire swine (N = 3; body weight 40–50 kg) were used in all porcine studies in accordance with a board-approved protocol. Porcine models were selected because they have well-developed fibrous pericardia and extensive diaphragmatic attachments that are similar to those in humans [116]. The animals were maintained in the supine position. After standard single-lumen endotracheal intubation, a surgical plane of anesthesia was maintained using isoflurane, 1–3%. The heart was allowed to beat naturally, without the use of anti-arrhythmic drugs. The animal was placed on a ventilator, and breathing was regulated at 0.23 Hz. Invasive hemodynamic and arterial blood gas monitoring was performed throughout the procedure. The surgeon accessed the apex of the heart through a subxiphoid percutaneous incision beneath the sternum, and placed HeartLander on the epicardium through a small pericardiotomy. This subxiphoid technique provided intrapericardial access for the robot on the beating heart without requiring differential ventilation or lung deflation. A photograph of the surgical suite used for all animal testing can be seen in Figure 6.1.

Figure 6.1: Photograph of the surgeon interacting with the HeartLander system through the user interface. The surgeon commands the control system at a high level using the joystick, while receiving real-time feedback of the location of the robot on the heart surface from the display. Some of the support instrumentation can be seen above the animal. The crawler is located on the heart, although the tether is difficult to see due to its neutral color and small size.

The surgeon was able to safely deliver HeartLander to the intrapericardial space using a subxiphoid approach in all porcine studies. A 30–40-mm percutaneous incision was made directly below the subxiphoid process of the sternum, and a small retractor was used to maintain the access. A photograph of a typical subxiphoid approach to the porcine heart can be seen in Figure 6.2. The surgeon then dissected the fascia and sinew located beneath the sternum to clear a direct path to the apex of the heart. A smaller 10–15-mm incision was then made in the pericardium, and 1–3 sutures were used to tent this pericardial opening. This provided direct access to the epicardial surface of the apex, whereby HeartLander was placed beneath the pericardium (Figure 6.3). In all studies, the heart was allowed to beat naturally without the use of pacing or anti-arrhythmic drugs. All animals survived until end of the procedure, at which point they were euthanized according to the board-approved protocol. No adverse hemodynamic or electrophysiological events, such as hypotension or fatal arrhythmias, were noted during any study. Normal sinus rhythm was maintained throughout. No significant epicardial damage was found by visual inspection or histological analyses of the excised hearts.

Following each subxiphoid access, the surgeon generated the heart surface model for the graphic display (see Figures 5.14 and 5.15). The technique described in Section 5.7 was sufficient to create heart models for all porcine studies.

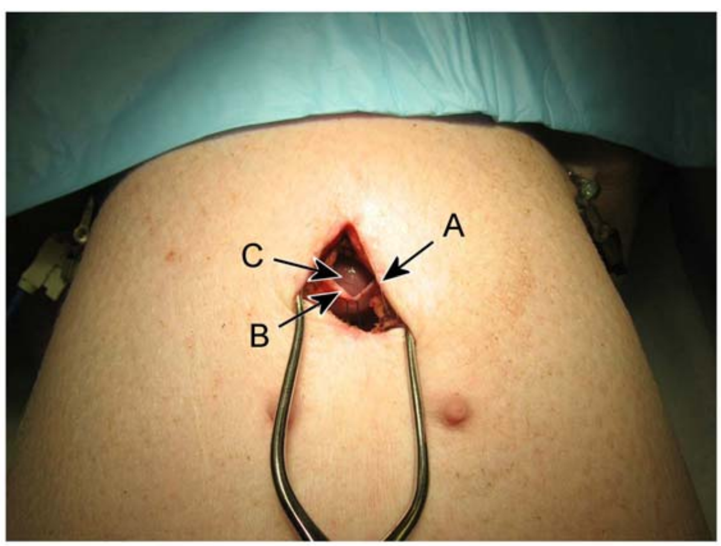

Figure 6.2: A photograph of the subxiphoid approach used in all porcine studies by the surgeon to deliver HeartLander beneath the pericardium near the apex of the heart. A 30–40-mm percutaneous incision (A) was made beneath the xiphoid process of the sternum to expose the apex of the heart. A 10–15-mm incision was then made in the pericardium (B), thus providing access to the epicardial surface of the apex (C).

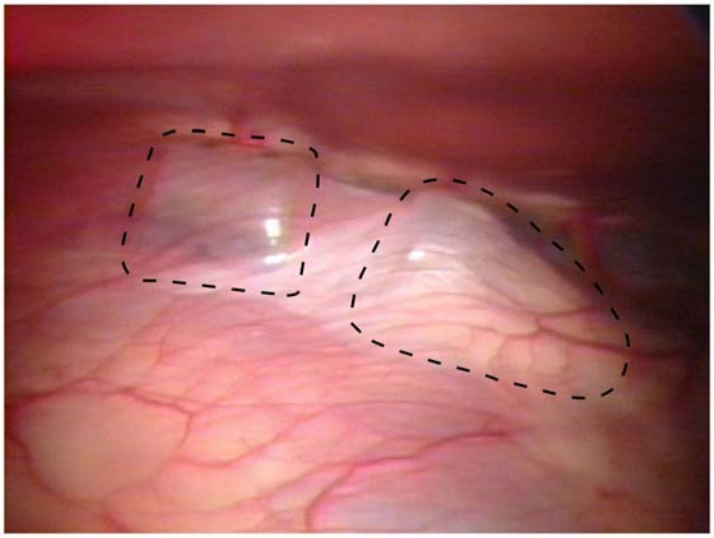

Figure 6.3: Photograph from a thoracoscope showing HeartLander beneath the pericardium on the anterior surface of the heart. The outlines of the front and rear bodies have been highlighted using a broken line. It can be seen that the pericardium is tightly pulled over the robot, thus forcing both bodies into contact with the curved epicardium of the heart.

6.2 In-Vivo Porcine Navigation Study

In the navigation study, we evaluated the ability of HeartLander to travel to the general target area from the apex of the beating heart in a semi-autonomous manner. This is the first component of the decomposition of a general target series acquisition presented in this thesis, which drove the design of the control system. The specific goal for the study was to demonstrate semi-autonomous navigation from the apex to regions that span the circumference of the ventricles, i.e., the anterior, lateral, and posterior surfaces (figure 6.4). This goal is clinically relevant as it covers the entire epicardial surface of the ventricles, which have great significance in the treatment of many cardiovascular diseases. In a clinical application, navigation to the general target area would be followed by fine positioning to each of the individual targets in the specified pattern for the application of treatments. These fine-positioning capabilities are evaluated in the next section of this thesis.

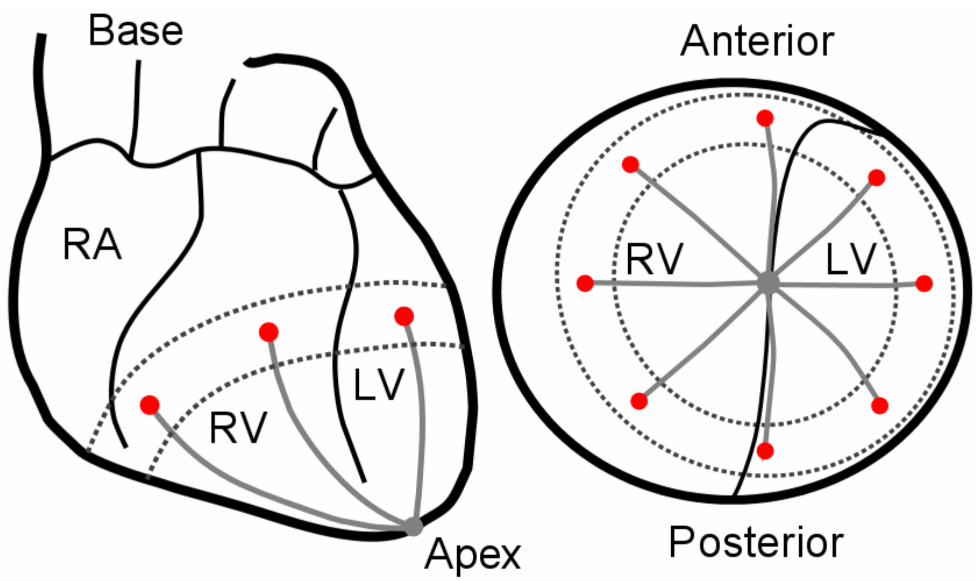

Figure 6.4: (left) Anterior view of the illustration of the navigation task, the initial portion of the general target acquisition decomposition. The circumference of the ventricles is the region between the broken lines, and three navigation targets are visible in red. (right) Apex view of the navigation targets spanning the circumference of the ventricles, the region between the broken lines.

6.2.1 Navigation Protocol

The apex was selected as the origin for all navigation paths because it is the anatomical location of the robot insertion beneath the pericardium, and can be used to reach the entire epicardial surface. The ventricles were chosen as the termination points for the navigation trials because they are the most clinically-relevant regions for our initial intrapericardial therapies. Navigation targets were selected to span the entire circumference of the ventricles in order to illustrate the ability of HeartLander to reach the anterior, left-lateral, right-lateral, and posterior epicardial surfaces (Figure 6.4). The targets for navigation were defined with respect to the moving reference frame of the beating heart, in the same manner as the robot tracking data. Accordingly, the locations of the targets did not vary over the respiration or heartbeat cycles, and thus appeared as stationary points in space. The 3-D locations of the navigation targets were defined in the coordinate system of the electromagnetic tracker, and thus were properly registered to the robot tracker data and the heart surface model.

On the porcine heart, the lengths of the anterior and posterior surfaces of the ventricles are approximately 70 mm and 50 mm, respectively [117]. These dimensions are similar to those of a healthy human heart. Navigation path lengths should thus fall within the range of 30–50 mm, taking into account the body length of the robot. The efficiency of the locomotion must be sufficiently high to accomplish each navigation trial within the target time of 120 s. This rate would result in the completion of ten navigation trials in twenty minutes, which is a clinically acceptable level of performance.

Based on these experimental criteria, separate navigation trials were performed to 7 individual targets located around the circumference of the ventricles. The targets were selected with locations near the superior end of each ventricle, thus requiring navigation over the entire ventricular surface. The targets on the anterior surface of the heart were located more distally than those on the posterior surface, because the ventricles are longer on the anterior surface than the posterior. Prior to each navigation trial, the surgeon selected the current navigation target. The surgeon then placed HeartLander on the epicardium near the apex, using the view of the ideal path to the target on the graphic display as a reference. The individual navigation trials proceeded until the surgeon released the joystick, or the robot acquired the navigation target. Accordingly, each trial consisted of a navigation component, followed by a single short fine-positioning target acquisition. Because the main goal was to evaluate the mechanics and control of navigation, the acceptable fine-positioning target acquisition distance was set to a relaxed value of 2.0 mm. Following each navigation trial, the following parameters were calculated: number of steps, path length, path width, total duration, speed, and efficiency. The target acquisition distance was also calculated, although it was not the focus of this study. These values were also averaged over all trials for the entire study. All sensor data was collected at 100 Hz using an A/D converter. The tracking sensor data was low-pass filtered with a cutoff frequency of 0.2 Hz to remove all physiological components of the motion, as described in Section 5.2. The path length for each navigation trial was calculated as the sum of the progress made toward the navigation target over each step. Path width was defined as the maximum lateral deviation of the robot over each path. The efficiency was calculated as follows:

$$E = \frac{\sum_{i}^{n} L_M(i)}{n \times L_C} \times 100 \qquad (5)$$

where n was the number of steps for the path, L_C was the commanded step length, and L_M was the step length measured from the robot tracker data.

6.2.2 Navigation Results

In the navigation study, the surgeon successfully completed navigation paths to the series of targets located around the circumference of the beating porcine. During each trial, the location of the robot location and corresponding navigation path were displayed to the surgeon in real time (Figure 5.15). This allowed the surgeon to monitor the progress of the robot toward the target. As can be seen in Figure 6.5, the seven targets spanned the anterior, lateral, and posterior surfaces of the heart. Note that the paths were shorter on the posterior surface due to the decreased posterior lengths of the ventricles. The navigation metrics for each trial, along with the averages and standard deviations for the entire study, are available in Table 6.1. The paths averaged 38 ± 10 mm in length, and 3 ± 3 mm in width. The average locomotion speed was 29 ± 13 mm/min, resulting in an average path duration of 97 ± 58 s. The locomotion efficiency was 40 ± 15%. Although the focus of this study was the navigation performance, all navigation targets were successfully acquired within the specified 2.0 mm.

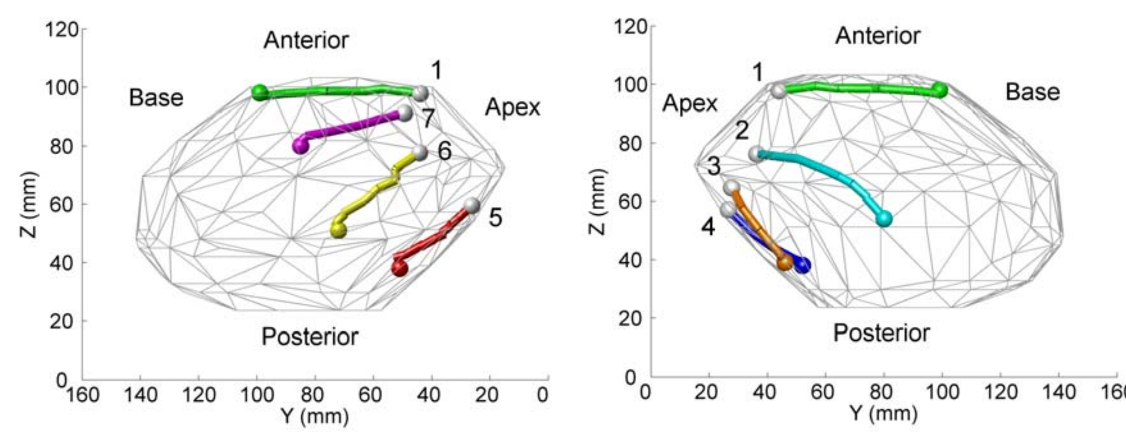

Figure 6.5: Image of heart surface model showing the targets and completed navigation paths reconstructed from microBIRD data collected in vivo using a beating-heart porcine model. All paths began around the apex (shown by white spheres), and terminated on the ventricles toward the base of the heart (shown by gray spheres). The seven paths illustrate coverage the ventricles around the circumference of the heart.

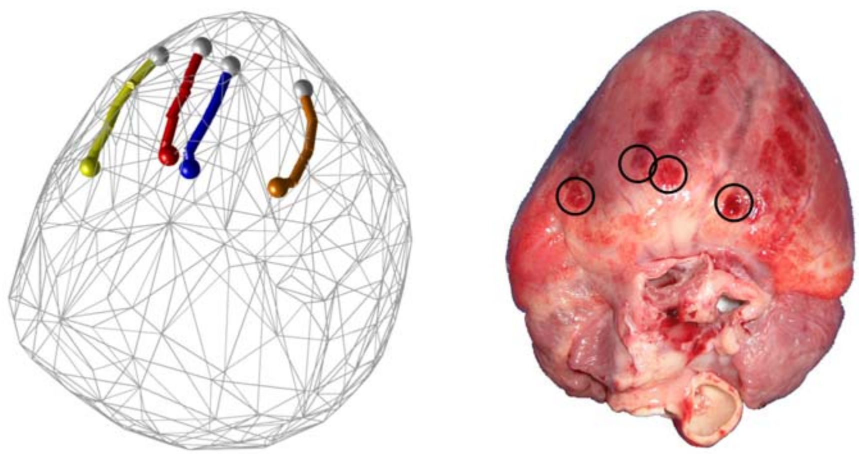

Figure 6.6: (left) Posterior view of the heart surface model showing the navigation paths on the posterior left and right ventricles. (right) Photograph of the excised porcine heart from the navigation study, showing the light suction marks left by the robot on the epicardium. These marks are harmless for the underlying tissue, but show the navigation paths. It is clear that the terminations of the paths (shown by circles) successfully reached the bases of the ventricles.

Table 6.1: The performance data from the navigation study on a closed-chest beating-heart porcine model.

Trial No.	Anatomical Location	No. Steps	Path Length (mm)	Path Width (mm)	Duration (s)	Speed (mm/min)	Efficiency (%)	Target Error (mm)
1	Anterior Midline	6	52	2	68	46	59	1.6
2	Left Lateral	14	50	7	207	15	28	2.6
3	Left Posterior	4	28	7	56	30	55	0.5
4	Posterior Midline	5	29	2	55	32	43	0.3
5	Right Posterior	10	29	0	95	18	20	1.9
6	Right Lateral	11	36	1	144	15	29	1.1
7	Right Anterior	6	39	3	54	44	49	0.0
Mean ± Std		8 ± 4	38 ± 10	3 ± 3	97 ± 58	29 ± 13	40 ± 15	1.1 ± 0.9

6.2.3 Navigation Discussion

The navigation study demonstrated the ability of HeartLander to provide access around the circumference of the heart in a precise, semi-autonomous, and stable fashion. The average target acquisition distance for the seven trials was 1.1 mm, which was within the goal of 2.0 mm. The navigation path lengths were approximately 50 mm on the anterior surface of the heart, and 30 mm on the posterior. These lengths indicate that the navigation trials adequately spanned the lengths of the anterior and posterior ventricles. Furthermore, photographic evidence of the navigation paths on the excised hearts from the suction marks left on the heart by the crawler verify these data (Figure 6.6). This distribution of the navigation targets over the anterior, left-lateral, right-lateral, and posterior ventricular surfaces illustrates the utility of HeartLander to provide general access around the entire circumference of the heart. Although the average locomotion efficiency was relatively low, 40%, the targets were acquired within an average of 97 s. This duration falls within the goal of 120 s, and is reasonable considering that, in general, no more than ten navigation trials will be required for a single intrapericardial therapy.

6.3 In-Vivo Porcine Positioning Study

The purpose of the fine-positioning study was to evaluate the ability of HeartLander to acquire the targets in a local pattern using a series of small, precise motions of the front body in a semi-autonomous manner (Figure 6.7). This task is the second and final component of the decomposition of general target acquisition that we selected to drive the design and testing of the control system. In a clinical application, the fine-positioning task would immediately follow the navigation of the robot to the general target area on the heart surface, which was described and evaluated in the preceding section of this thesis. Following the acquisition of each target, the surgeon would perform a treatment to the epicardium through the working channel of HeartLander. Epicardial treatments were simulated in the fine-positioning study with injections of dye into the heart using the remote injection system described in Section 4.8.1. The observed locations of these injections on the porcine heart also served as a ground truth with which to evaluate the accuracy of the target acquisitions.

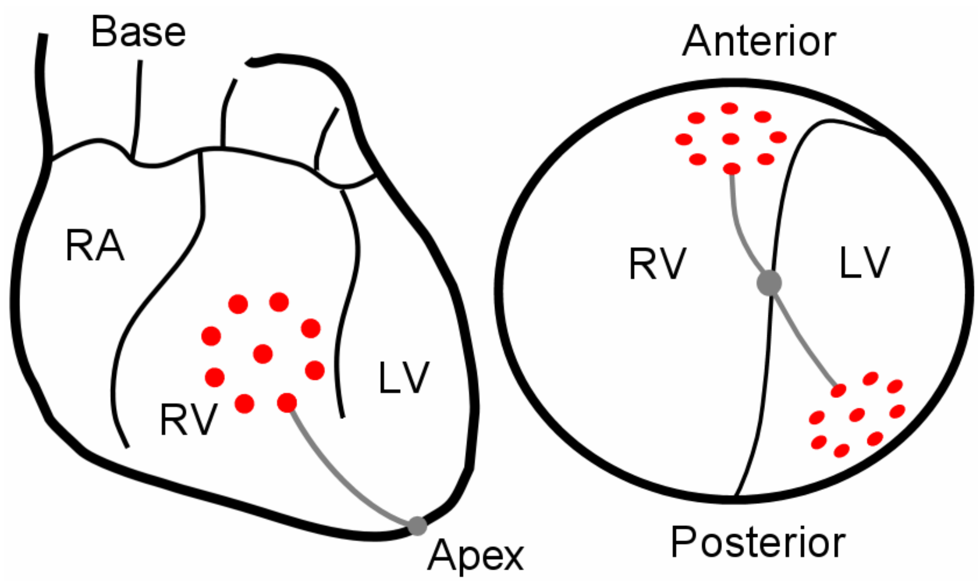

Figure 6.7: (left) Anterior view of the fine-positioning task illustration. (right) Apex view of the fine-positioning task illustration. The fine-positioning targets are shown in red, and the navigation paths in gray.

6.3.1 Fine-Positioning Protocol

To begin each fine-positioning trial, the surgeon used the computer interface to set the parameters of the target pattern, and position the pattern at the desired location on the heart surface model while viewing the graphic display. The size, shape, and density of the target pattern could be easily altered by the surgeon based on the anatomy of the general target region, e.g., the size or curvature of the left ventricle. Through communication with our clinical and industrial colleagues, we selected a local target pattern shape comprising a series of targets located around the circumference of a circle, with one additional central target (Figure 6.7). This pattern was considered to have sufficient size, shape, and complexity to simulate the treatment patterns for our selected intrapericardial therapies. The right and left ventricular surfaces were selected for the application of the target patterns due to their clinical significance. Over two separate animal trials, the circular pattern was applied to the anterior and posterior ventricular surfaces of the beating porcine heart with the chest closed and the pericardium intact. The first trial was located on the anterior surface of the porcine heart, and featured an acquisition pattern with 8 targets located around the circumference of a 20-mm diameter circle with one central target (Figure 6.7). The second trial was located on the posterior surface of the porcine heart, and featured a smaller acquisition pattern of 7 targets located around the circumference of a 15-mm circle with one central target. This smaller pattern was chosen because the size of the porcine heart was approximately 20% smaller than the heart from the first trial.

After selecting the pattern parameters and location on the heart surface model, the surgeon acquired each individual target within the pattern using the semi-autonomous, fine-positioning control mode of the HeartLander system. With the rear body gripping the epicardium, the control system advanced the front body of crawler toward the current target until the surgeon released the joystick or the robot moved within the specified range of the target.

Targets were defined with respect to the electromagnetic tracking system reference frame, and were therefore properly registered to the heart surface model and the robot tracking sensor. The positions and orientations of the targets did not vary over the respiration or heartbeat cycles, and thus appeared as stationary points in space. This simulated the mounting of the magnetic transmitter on the heart surface in order to compensate for the underlying physiological motion present for all components within the control space: the heart surface, the crawling robot, and the surface targets. This compensation was possible because the robot and targets moved with the surface of the heart. Targets referred to 3-D locations on the heart surface for which the anatomical mappings or labels were unknown. Proper anatomical mapping or labeling of the 3-D points on the heart surface would have required the integration of high-resolution preoperative or intraoperative imaging techniques with our simple heart surface model, and was beyond the scope of this thesis.

To determine the offset between the robot and the target, the 3-D location of the target was projected into the transverse plane of the robot, calculated from the position and orientation of the robot tracking sensor (see Section 5.4). The control system then used the inverse kinematics of the crawler to calculate the drive wire lengths necessary to align the front body robot with the current target, based on the 2-D Cartesian offset. The real-time position and orientation of the robot tracking sensor provided feedback for closed-loop control of the robot as it aligned the front body with the current target. The distance between the robot and the target was calculated using the data from the electromagnetic tracking sensor on the robot and the 3-D location of the target. When the control system determined that this offset was within the acceptable value specified by the surgeon in the user interface, the suction pad of the front body was activated to grip the epicardium and fix the robot at the target. We did not constrain the orientation of the robot at the target because our therapeutic applications specify only the locations of the treatments. For the first trial, our goal for the fine-positioning task was to maneuver the front body of the robot within 1.5 mm. This threshold was determined from conversations with several cardiac surgeons and electrophysiologists regarding our initial therapies. In the second porcine trial, we increased the precision requirement to 1.0 mm, in order to further test the limits of the fine-positioning system. During both trials, our goal was to complete each individual target acquisition within 30 s. This single acquisition rate was considered reasonable because a therapy would consist of no more than 20 treatments, which would be administered within a total duration of ten minutes.

During target acquisition, the surgeon monitored the progress of the front body of the robot toward the current target on the graphic display. Following each target acquisition, the final distance between the robot and the target was calculated, along with the length of time for completion. The surgeon then made an injection of dye into the myocardium using the remote injection system in order simulate an epicardial treatment and to mark the physical location on the porcine heart. The accuracy of the fine-positioning system was determined by comparing the locations of the robot and the target, measured with the tracking system, to the physical dye marks on the excised porcine hearts following the trial. These calculations are described in detail in the next subsection.

6.3.2 Fine-Positioning Accuracy and Error Definitions

The 3-D locations of the targets, the robot, and heart surface were measured with respect to the electromagnetic tracking system reference frame. As described in the previous subsection, the comparable underlying motion due to respiration and heartbeat was removed in the localization of all components (i.e. robot, target, and heart surface) within the control system. The robot location was provided in real time by filtering the data from the robot tracking sensor, while the targets and heart surface model were defined in a static manner with respect to the tracking system reference frame. Additionally, the location of the robot on the surface of the porcine heart at the time of the dye injection can be estimated from the epicardial dye mark. In bench testing, it has been noted that these dye marks spread in a relatively even manner over the circular region of the epicardium drawn into the suction pad of the front body of the robot. Accordingly, the location of the robot at the time of injection was estimated as the center of the circular region encompassing the dye mark. Although this localization method was imperfect because we could not guarantee normal dispersal of the dye throughout the myocardium, it provided a ground truth with which to compare the tracker-based accuracy.

Accuracy was assessed at the both the absolute and relative levels. We defined absolute accuracy as the degree to which the location and orientation of the target pattern on the heart surface model (based on the tracking data) matched the location and orientation of the target pattern on the excised porcine heart (based on the dye injection marks). This accuracy is critical because the tracker-based location of the robot on the heart surface model was the only visual feedback provided to the surgeon during the closed-chest animal testing. For the fine-positioning study, we performed a qualitative assessment of absolute accuracy. A rigorous quantitative assessment will be possible in the future when anatomical labels have been integrated into the heart surface model using high-quality preoperative or intraoperative imaging.

Relative accuracy indicated the degree to which the locations of the individual targets, relative to one another, aligned between the electromagnetic tracking data and the injection dye marks on the excised porcine heart. In the assessment of relative accuracy, the target patterns from the tracker data and injection marks were first aligned to minimize the sum of the root-squared errors over all targets. The resultant planar distances between the tracker-based and dye-based target locations were then calculated. Furthermore, the sources and magnitudes of the errors that compose the total relative error between the tracker-based and dye-based patterns were determined.

There were three sources of error that contributed to the total relative error between the tracker-based patterns and the injection-based patterns: (1) the known distance between the robot tracker and target when the control system determined the target to be acquired, (2) the known offset that occurred when the front body of the robot gripped the epicardium following target acquisition, and (3) the unknown error due to the electromagnetic robot tracking. The first two sources of error were measured in real time and known to the control system, while the electromagnetic tracking error was only estimated by offline comparison to the dye patterns.

The absolute accuracy was qualitatively assessed for both the anterior and posterior patterns. The relative accuracy of the anterior pattern was not assessed because the pattern was accidentally positioned across the left and right ventricles, despite the attempt of the surgeon to avoid this case. This placement violated one of the main assumptions of the control system design, and resulted in abnormally large relative errors between the portions of the patterns located on the two chamber surfaces.

6.3.3 Fine-Positioning Absolute Accuracy Results

The locations and orientations of the tracker-based and dye-based target patterns on both the anterior and posterior heart surfaces were qualitatively compared in the assessment of absolute accuracy of fine positioning. The tracker-based pattern was evaluated using the 2-D projection of the robot positions and heart surface model into the plane corresponding to the appropriate view of the heart (i.e., anterior or posterior). The dye-based pattern was evaluated from a photograph of the excised porcine heart, showing the aspect of the heart on which the pattern was applied. The tracker images and dye photographs were scaled based on known distances in each image, and were aligned so the contours of the hearts matched. The scaled and aligned tracker images and excised heart photographs can be seen separately in the top two frames of Figures 6.8 and 6.9 for the anterior and posterior patterns respectively. These images were then overlaid in the lower-left frames of Figures 6.8 and 6.9, to show the agreement in scale and alignment of the hearts using these two different imaging modalities. Lastly, the tracker-based patterns (alone) were overlaid on the photographs of the dye patterns in the lower-right frames of Figure 6.8 and 6.9. These figures demonstrate good qualitative absolute accuracy in the position and orientation of the tracker-based and dye-based target patterns on the anterior and posterior surfaces of the heart. In order to evaluate the agreement between each of the individual targets within the patterns, we address the relative accuracy in the next subsection.

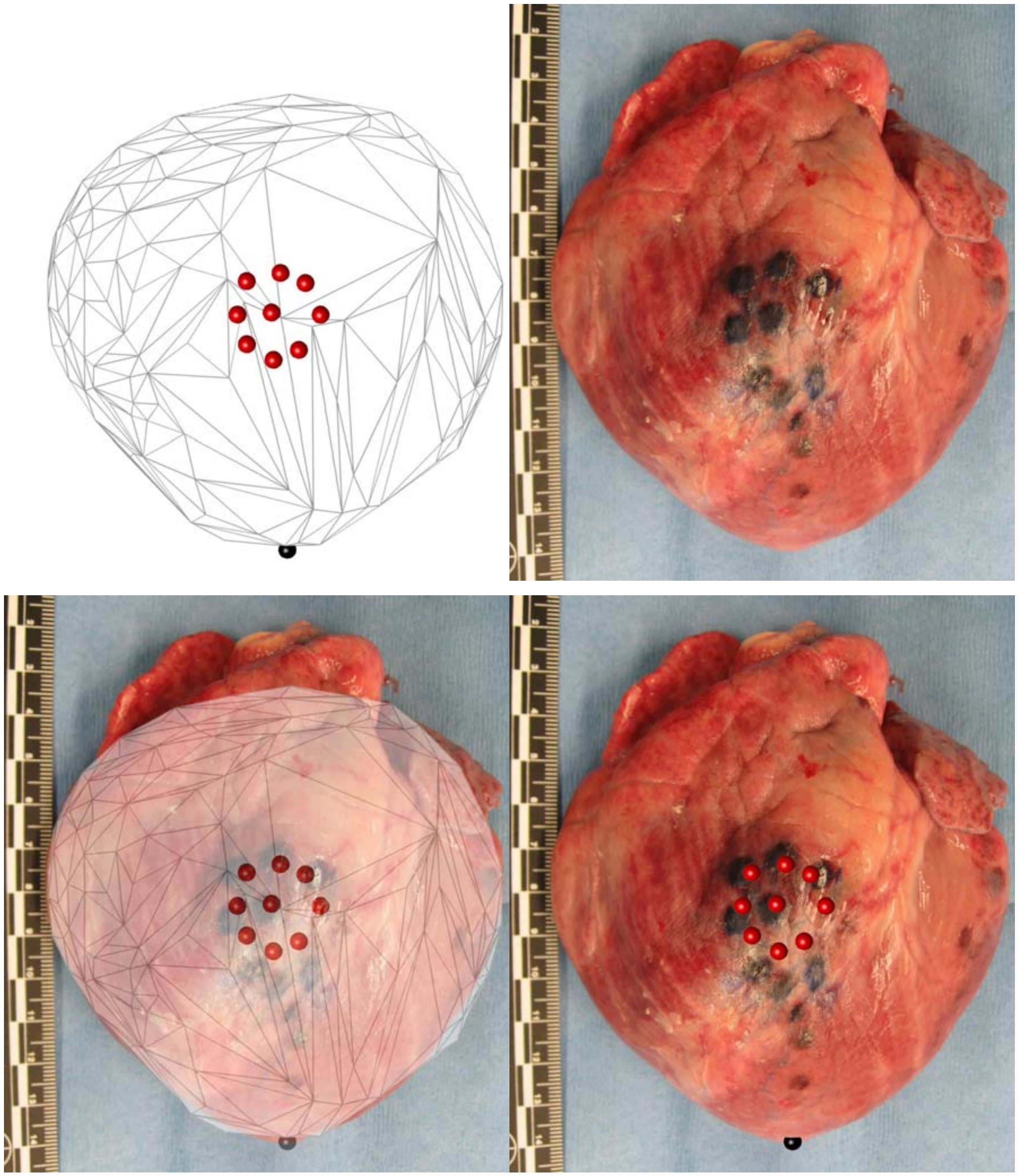

Figure 6.8: (upper-left) Image of the heart surface model and tracker-based target acquisition pattern on the anterior surface of the heart. This was displayed as feedback to the surgeon during the closed-chest testing. (upper-right) Photograph of the excised porcine heart and injection-based target acquisition pattern on the anterior surface of the heart. The two images are scaled and aligned properly. (lower-left) The tracker-based image and injection photograph overlaid. (lower-right) The tracker-based injection target pattern overlaid on the injection photograph. The absolute location and orientation of the target pattern qualitatively agree between the two methods, although the errors due to the cross-chamber placement of the pattern are apparent on the excised heart.

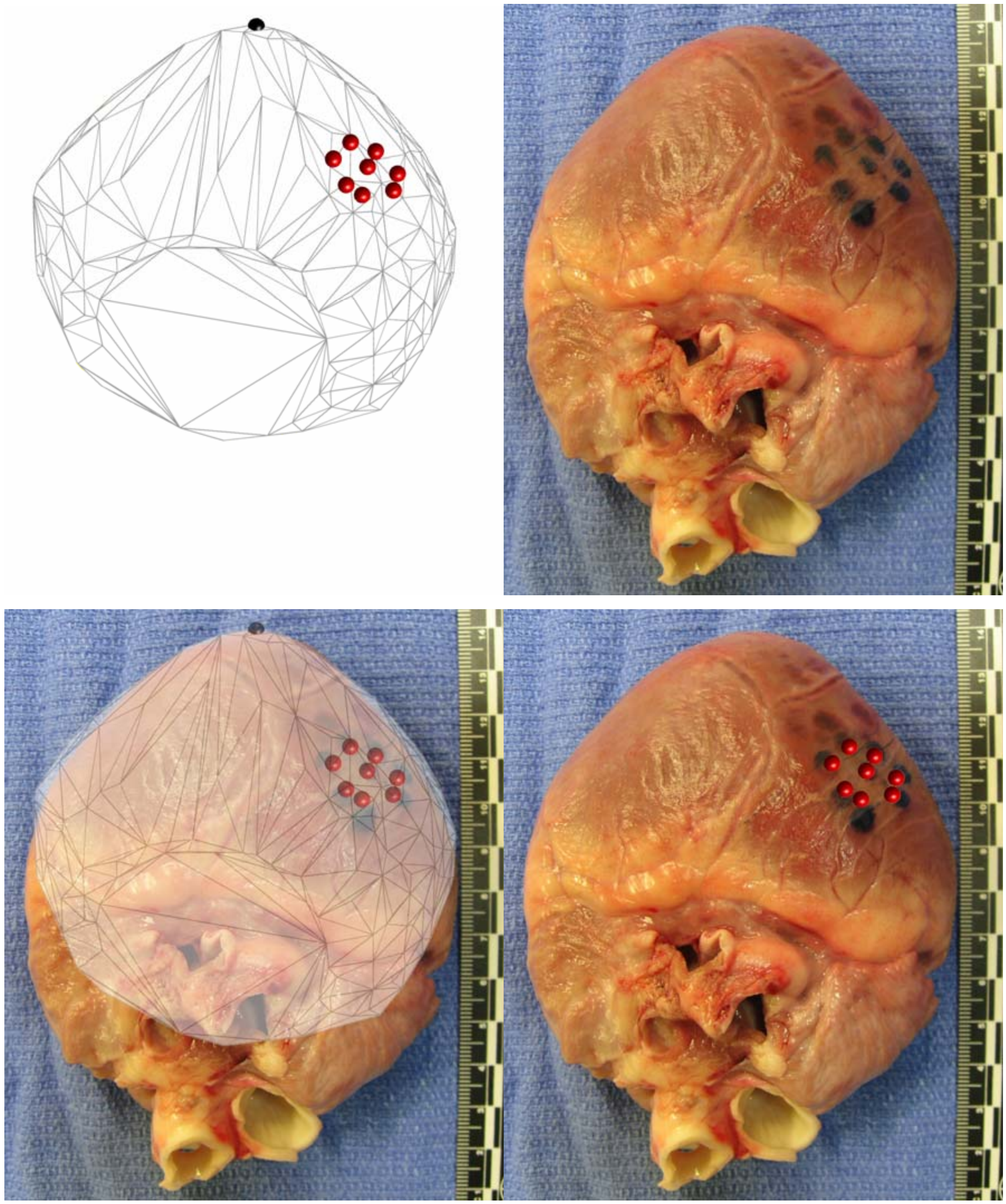

Figure 6.9: (upper-left) Image of the heart surface model and tracker-based target acquisition pattern on the posterior surface of the heart. This was displayed as feedback to the surgeon during the closed-chest testing. (upper-right) Photograph of the excised porcine heart and injection-based target acquisition pattern on the posterior surface of the heart. The two images are scaled and aligned properly. (lower-left) The tracker-based image and injection photograph overlaid. (lower-right) The tracker-based injection target pattern overlaid on the injection photograph. The absolute location and orientation of the target pattern qualitatively agree between the two methods.

6.3.4 Fine-Positioning Relative Accuracy Results

The errors between the positions of the individual targets in the tracker-based measurements and dye-based measurements were determined in the assessment of the relative accuracy of fine positioning for the posterior trial. All tracker-based patterns were generated from a 2-D view of the tracker data, with a view angle normal to the least-squares best-fit plane through the tracker data at the time of the dye injections. Figure 6.10 shows the tracker-based positions of the planned targets, referred to as pattern "A", in the upper-left frame. This figure also shows the tracker readings of the robot position at the time of target acquisition (pattern "B", upper-right frame), and the tracker readings of the robot position at the time of dye injections (pattern "C", lower-left frame). The dye mark pattern (pattern "D") was assessed using a photograph of the excised porcine heart with the camera oriented normal to the surface of the heart on which the dye pattern was visible (Figure 6.10, lower-right frame). As stated in Section 6.3.2, the location of the robot at the time of injection was estimated as the center of the circular region encompassing the distribution of the dye over the tissue. All three tracker-based patterns (A, B, C) and the dye mark photograph (D) were scaled according to known distances in both imaging modalities. The locations of the tracker-based patterns were properly registered to one another because they were all measured with respect to the tracking system reference frame. To align the tracker-based patterns to the dye mark pattern from the photograph, the translation and rotation that minimized the sum of root-squared distances between the tracker-based and dye-based injection locations were calculated.

The total relative error between each dye mark and the planned tracker-based target (A→D) was due to the combined serial effects of three errors:

1. the error between the tracker-based planned target and the robot tracker reading at the target acquisition event (A→B),
2. the error between the robot tracker reading at the target acquisition event and the robot tracker reading at the dye injection event (B→C), and
3. the error between the robot tracker reading at the dye injection event and the physical dye mark on the heart tissue (C→D).

The individual contributions of these sources of error can be seen in Figure 6.11, and in columns 3-5 in Table 6.2. The average error between the planned targets and robot tracker readings at target acquisition (A→B) was 0.7 ± 0.4 mm, which was within the range of 1.0 mm specified by the surgeon for the control system. The average error between the robot tracker readings at target acquisition and dye injection (B→C), caused by gripping the epicardium following target acquisition, was 1.1 ± 0.5 mm. The average error between the robot tracker readings at dye injection and the dye marks on the excised heart (C→D) was 0.8 ± 0.9 mm. The average total relative error between the tracker-based planned targets and the dye marks on the excised heart (A→D) was 1.7 ± 1.0 mm. A 2-D plot of the positions of all three tracker-based patterns (planned targets, robot tracker readings at acquisition, and robot tracker readings at injection) and the dye mark pattern can be seen in Figure 6.12. The corresponding error values for each target, and averaged over all targets, can be found in Table 6.2.

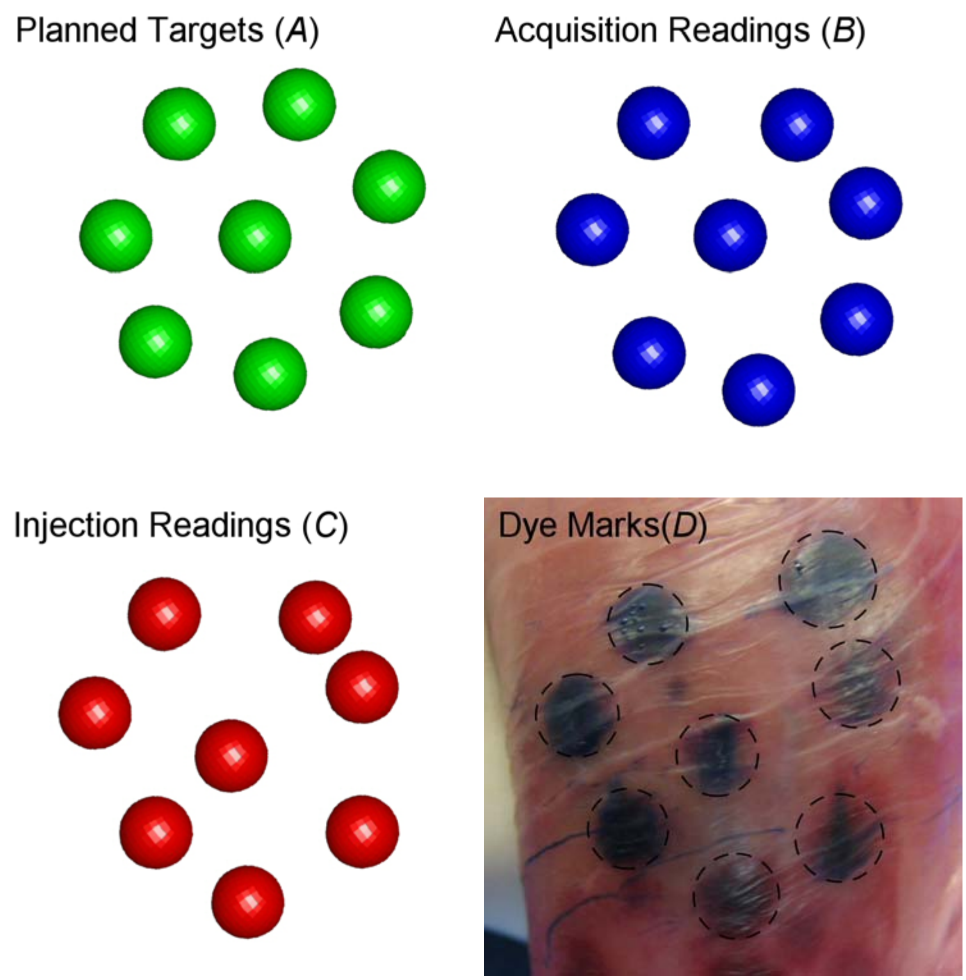

Figure 6.10: (upper-left) The tracker-based pattern of the targets. (upper-right) The tracker-based pattern of the robot positions at the target acquisitions, as determined by the fine-positioning control system. (lower-right) The tracker-based pattern of the robot positions at the dye injections, after gripping the epicardium with the crawler front body. All tracker-based patterns were generated from a 2-D view of the tracker data with a view angle normal to the least-squares best-fit plane through the tracker data at the time of the dye injections. (lower-right) Photograph of the dye-based pattern, taken normal to the surface of the heart.

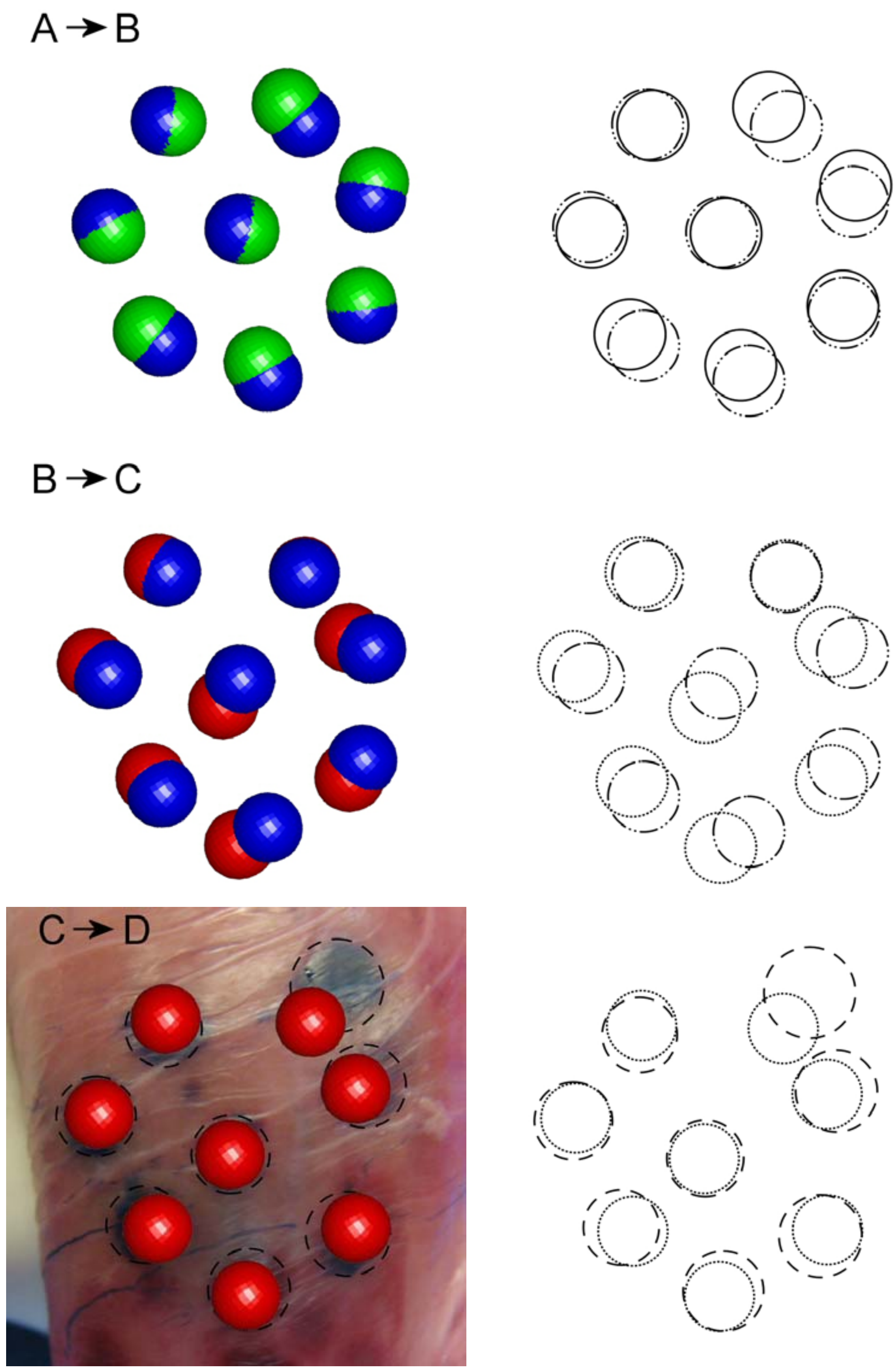

Figure 6.11: Images of the three sources of error that contribute to the total relative error between the tracker-based targets and the dye-based injection marks. (upper row) Error from the tracker-based target and robot at target acquisition. (middle row) Error from the tracker-based robot locations at target acquisition and dye injection. (lower row) Error from the tracker-based robot location and dye-based marks at dye injection.

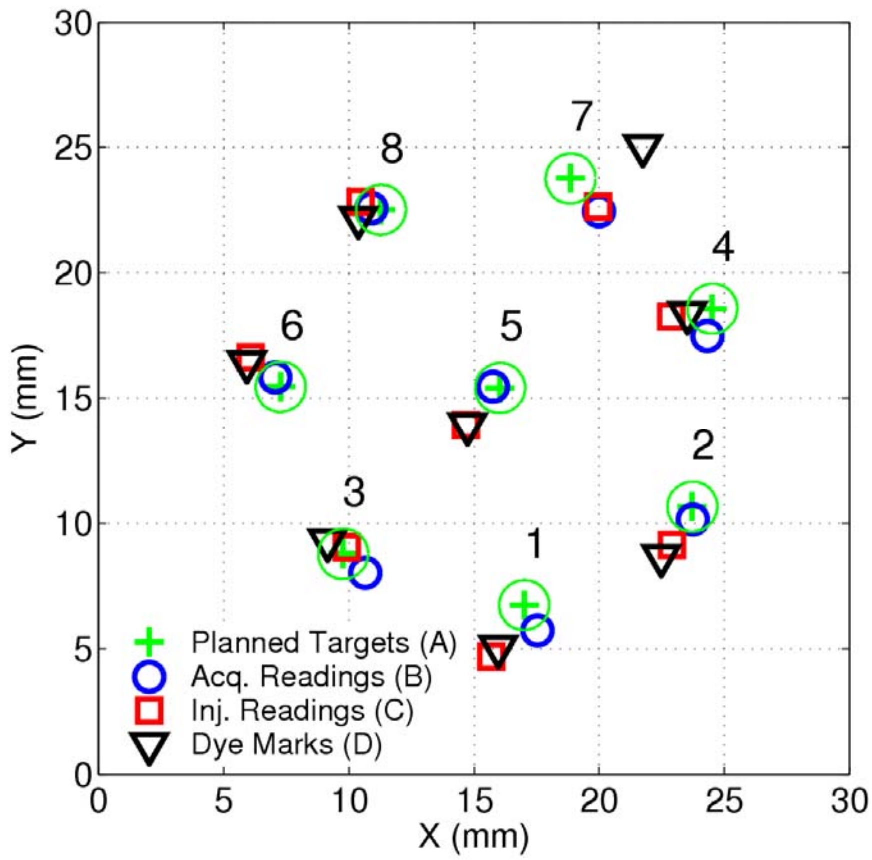

Figure 6:12: A 2-D plot of the locations of all tracker-based patterns (targets, robot at acquisition, and robot at injection) and the dye-based injection marks. The acceptable range for target acquisition, used by the control system, is shown as the larger dark circles.

Table 6.2: The values for each of the three sources of relative error, and the total relative error for the 8 target acquisitions of the pattern applied to the posterior surface of the beating porcine heart. The distances of the targets from the initial starting location, and the durations for each target acquisition are also provided.

Target No.	Target Distance (mm)	A→B Error (mm)	B→C Error (mm)	C→D Error (mm)	A→D Error (mm)	Duration (s)
1	5.0	1.0	1.9	0.4	1.7	13
2	9.8	0.4	0.8	0.6	2.3	28
3	9.8	1.0	1.0	0.8	0.9	23
4	15.9	0.9	1.6	0.7	0.3	9
5	12.5	0.3	1.5	0.1	1.6	21
6	15.9	0.4	1.1	0.3	1.9	20
7	19.5	1.5	1.0	3.0	3.6	56
8	5.0	0.3	0.3	0.7	1.1	11
Mean ± Std		0.7 ± 0.4	1.1 ± 0.5	0.8 ± 0.9	1.7 ± 1.0	23 ± 15

6.3.5 Fine-Positioning Discussion

The fine-positioning study demonstrated high absolute accuracy in a qualitative sense; i.e., visual alignment of the position and orientation of the target patterns measured with the electromagnetic tracking data and the dye injection patterns visible on the excised heart. The absolute accuracy was qualitatively high for the injection patterns on both the anterior (Figure 6.8) and posterior (Figure 6.9) surfaces of the heart. There are many errors inherent to a comparison of this nature. The size and shape of the heart can vary significantly between the in-situ and excised states due to the severed attachments of the great vessels, the absence of blood, and relaxation of the cardiac musculature. Additionally, both the tracker-based image and excised heart photograph show only a single pose of the heart over the cardiac cycle, which likely have no direct correspondence to one another. Accordingly, rigorous calculation of the absolute accuracy based on this comparison method would be inherently flawed, and could generate misleading results. We believe that the qualitative assessment of the absolute accuracy reported using this comparison method is fair, and successfully demonstrated that the graphical display of the robot tracking data over the heart surface model corresponds to the same geometric location on the physical heart.

HeartLander also demonstrated high relative accuracy; i.e., alignment of the positions of the individual targets measured with the electromagnetic tracking system and the dye marks visible on the excised heart. For this analysis, the tracker-based and dye-based images were aligned to minimize the sum of the root-squared distances between the tracker-based and dye-based target positions. Accordingly, relative accuracy measures the ability of HeartLander to precisely deliver treatments in a specified pattern, without regard to the absolute position of the patterns on the heart. This is obvious as the patterns were first aligned for maximum agreement. The control system was able to position the front body of the robot within an average of 0.7 mm of the planned tracker-based targets, which was within the specified range of 1.0 mm for the posterior pattern. Target 7 was not acquired within the specified range (1.5-mm error), because the surgeon terminated the trial after the control system was unable to acquire the target after approximately one minute. The average acquisition time was 23 s, which was below the goal of 30 s. The error between the planned tracker-based targets and robot tracker readings at the time of target acquisition (A→B) is measured by the tracking system in real time, and therefore known to the control system. Accordingly, this error can likely be reduced by tuning the control parameters or allowing the target acquisitions to run for longer durations to improve the accuracy. An additional average error of 1.1 mm between the planned tracker-based targets and the robot tracker readings (B→C) occurred after the control system determined that the target was acquired, and before the dye was injected into the heart. This additional error was due to the front body of the robot gripping the epicardium of the moving heart, and was also measured by the tracking system in real time during the testing. In the future, this error can be reduced by using the robot tracking data to synchronize the gripping of the epicardium with the cardiac cycle. By gripping the heart surface at a specific phase of the cardiac cycle, the robot will overcome the variability of the heart position that likely causes this additional error. The last source of error for the relative accuracy is the error between the robot tracker readings at dye injection and the physical positions of the dye marks on the excised hearts (C→D). This error could be due to positioning inaccuracy of the electromagnetic tracking system, or distortion of the excised heart from its shape in situ. In order to further classify this error, we must evaluate the dye marks (or another form of marking) on the heart in situ. Although this error is relatively small in magnitude, 0.8 mm, it must be addressed in future work. The average total relative error for the fine-positioning task was measured to be 1.7 mm. This error is larger than the specified range of 1.0 mm set within the control system, but takes into account the errors due to gripping the epicardium and the distortion of the excised heart, which were not taken into account by the control system. In the future, each of the three sources of the relative error must be reduced to bring the total relative error within the specified range. Nonetheless, this relative accuracy is impressive considering that the animal testing was performed with the chest closed, the pericardium intact, and the heart unconstrained. The results of this study, combined with those of the navigation study, demonstrate that HeartLander can acquire targets anywhere on the epicardial surfaces of the ventricles in a semi-autonomous and precise manner on the beating porcine heart with the chest closed and pericardium intact.

Future studies must also address the total accuracy of the fine-positioning system, which would comprise the absolute and relative accuracies described in this section. In such a study, HeartLander would attempt to generate a treatment pattern at specific anatomical locations on the surface of the heart, which would be compared offline to the visual locations of the treatments on the animal heart. A study of this nature would truly demonstrate the clinical potential of the HeartLander system, but would require the anatomical labeling of the geometric points that compose the heart surface model. This mapping requires the integration of high-resolution preoperative or intraoperative imaging techniques, which is considered to be future work for the HeartLander project.

6.4 In-Vivo Porcine Stability Study

This study evaluates the ability of the HeartLander system to provide stability during both the navigation and fine-positioning components of target acquisition. This capability is critical to demonstrate that HeartLander provides a stable platform relative to the heart surface in order to operate safely on the unconstrained epicardium.

6.4.1 Stability Protocol

Using the data from both the navigation and fine-positioning studies, we quantified the stability provided by HeartLander following target acquisition with both bodies fixed to the epicardium. Our goal for stability was to maintain the maximum resultant drift of the robot, after removing the physiological motion with a low-pass filter, below 1.0 mm for a period of 30 s. Considering that mechanical epicardial stabilizers currently used in cardiac surgery exhibit a residual motion of 1.5–2.4 mm, we believe that this goal is sufficiently stringent [11], [12]. Additionally, the resultant drift is a conservative estimation of stability because it attributes all motion that remains after low-pass filtering to slippage of HeartLander relative to the epicardium. In reality, there exists variation in the pose of the heart over the heartbeat and respiratory cycles that is erroneously classified as slipping by our methodology. The low-pass filtering stopband ripple attenuation was decreased from -20dB to -40dB to eliminate all physiological motion from the robot tracker data. This more aggressive filtering was used offline because the increased delay was not detrimental, as it is for real-time navigation and fine-positioning. If HeartLander did not slip at all relative to the epicardium, the maximum resultant drift would have a value of zero, indicating perfect stability.

Stability was assessed at each of the navigation targets (N = 7) and each of the anterior fine-positioning targets (N = 9). The navigation targets spanned the circumference of the ventricles, while the fine-positioning targets were all located on the anterior surface of the left ventricle. Accordingly, stability was assessed over a wide range of the heart.

6.4.2 Stability Results

Stability of epicardial fixation was estimated by measuring the maximum 3-D resultant drift of the robot for 30 seconds following target acquisitions in the navigation and fine-positioning studies. Figure 6.13 shows the raw tracker data from the robot while resting on the heart, and the residual filtered motion that is attributed to slippage of HeartLander over the epicardium. For the navigation target acquisitions (N = 7), the average maximum resultant drift was 0.6 ± 0.1 mm. For the fine-positioning target acquisitions (N = 9), the average maximum resultant drift increased to 0.9 ± 0.5 mm. Over all trials, the average maximum resultant drift was 0.7 mm. The stability data from all trials can be found in Table 6.3.

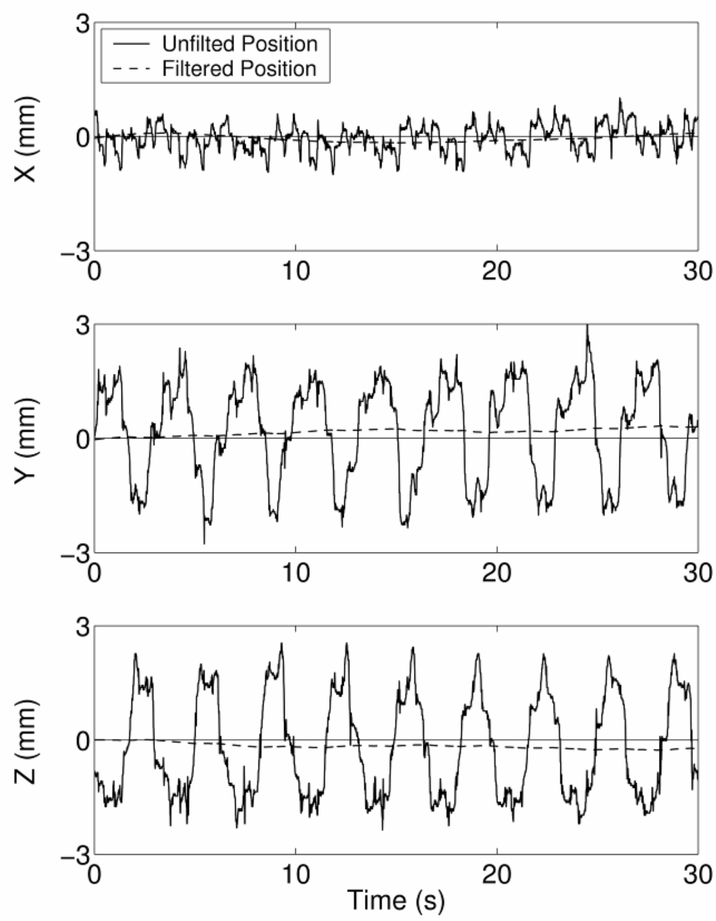

Figure 6.13: Plots showing the *x*, *y*, and *z* components of the motion measured by the microBIRD™ tracking sensor when the robot is stationary and fixed to the epicardium with both suction grippers. The raw data (*solid line*) shows that the heart has considerable motion over the physiological cycles. The filtered data (*broken line*) shows that there is very little low-frequency drift of the robot over the epicardium during this 30 s period.

Table 6.3: The stability data for both the navigation and fine-positioning studies. The stability measure was calculated as the maximum resultant deviation of the low-pass filtered position data over the 30 s window in which both crawler bodies were fixed to the epicardium of the beating heart.

Target No.	Navigation Study		Fine-Positioning Study	
	Anatomical Location	Drift (mm)	Anatomical Location	Drift (mm)
1	Anterior midline	0.7	Left antero-lateral	0.3
2	Left lateral	0.3	Left antero-lateral	0.3
3	Left posterior	0.7	Left antero-lateral	0.9
4	Posterior midline	0.5	Left antero-lateral	0.4
5	Right posterior	0.5	Left antero-lateral	1.0
6	Right lateral	0.6	Left antero-lateral	1.3
7	Right anterior	0.6	Left antero-lateral	1.7
8			Left antero-lateral	1.0
9			Left antero-lateral	1.0
Mean ± Std		0.6 ± 0.1		0.9 ± 0.5

6.4.3 Stability Discussion

The stability provided by HeartLander following target acquisition on the anterior, left-lateral, right-lateral, and posterior regions of the ventricles was shown to be greater than that of commercial mechanical stabilizers used in surgery, which exhibit 1.5–2.4 mm of residual motion [11],[12]. The goal for epicardial stability was to keep the maximum resultant drift of the robot below 1.0 mm for a period of 30 s with both bodies fixed to the epicardium. The 3D drift averages for the navigation and fine-positioning studies were 0.6 and 0.9 mm respectively, below the target threshold in both cases. The decrease in stability for the fine-positioning study may have been due to the fact that the front and rear bodies were located farther from one another compared to the navigation task. This increased wire extension length may have allowed the external transverse forces applied by the pericardium to slightly destabilize the front body.

6.5 Locomotion Synchronization Study

This study was conducted to evaluate the ability of the synchronization algorithm to detect the end-expiration (EE) events in respiration, and to determine the effects of synchronized locomotion on various performance parameters. As described in Section 5.3.2, the rest period following EE was selected as the stepping synchronization modulator because it is the period during which the heart is at its most posterior location and the lungs occupy the minimum volume. We hypothesized that the combined effects of these two factors would decrease the pericardial pressure, and thus friction force, on the HeartLander crawler during locomotion. Accordingly, we hypothesized that locomotion efficiency would increase when the stepping actions (i.e., extension and retraction) were properly synchronized with the rest period following EE events in respiration. As with the previous testing, this study was conducted on a beating porcine heart, with the chest closed and pericardium intact.

6.5.1 Locomotion Synchronization Protocol

Locomotion synchronization trials were performed on the lateral wall of the right ventricle (Figure 6.14). Over the same pathway on the heart, 18 locomotion trials were conducted, half of which had stepping synchronization active (n = 9). The trials without stepping synchronization served as control trials (n = 9). The trial order was such that the stepping synchronization trials and control trials were alternated to avoid potentially confounding the results with time varying effects such as heart swelling. Each locomotion trial consisted of 6 steps. For the stepping synchronization trials, the EE events were detected using the electromagnetic tracking data, as described in Section 5.3.2. As in previous locomotion testing, data were collected from the vacuum line pressure sensors, drive-wire load cells, and electromagnetic tracking system. The following locomotion parameters were calculated for each step and averaged over the control and stepping synchronization sets of trials: extension efficiency, retraction efficiency, step efficiency, step length, step progress, extension force, and retraction force. The values of these parameters for the control and stepping synchronization sets of data were then compared using the Mann-Whitney-Wilcoxon test. This non-parametric test assesses the probability that two sets of observations come from the same distribution.

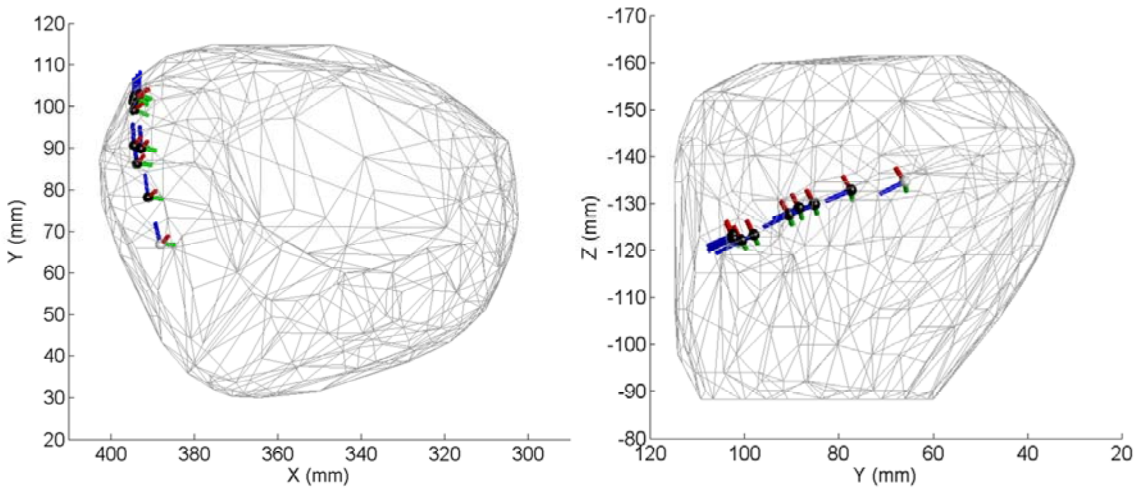

Figure 6.14: The left plot shows an anterior view of a locomotion trial on the lateral wall of the right ventricle. The right plot shows a right-lateral view of the same locomotion trial. The locations of the robot at each step is shown by the black spheres. The robot orientation is also shown via the primary sensor axes at each step.

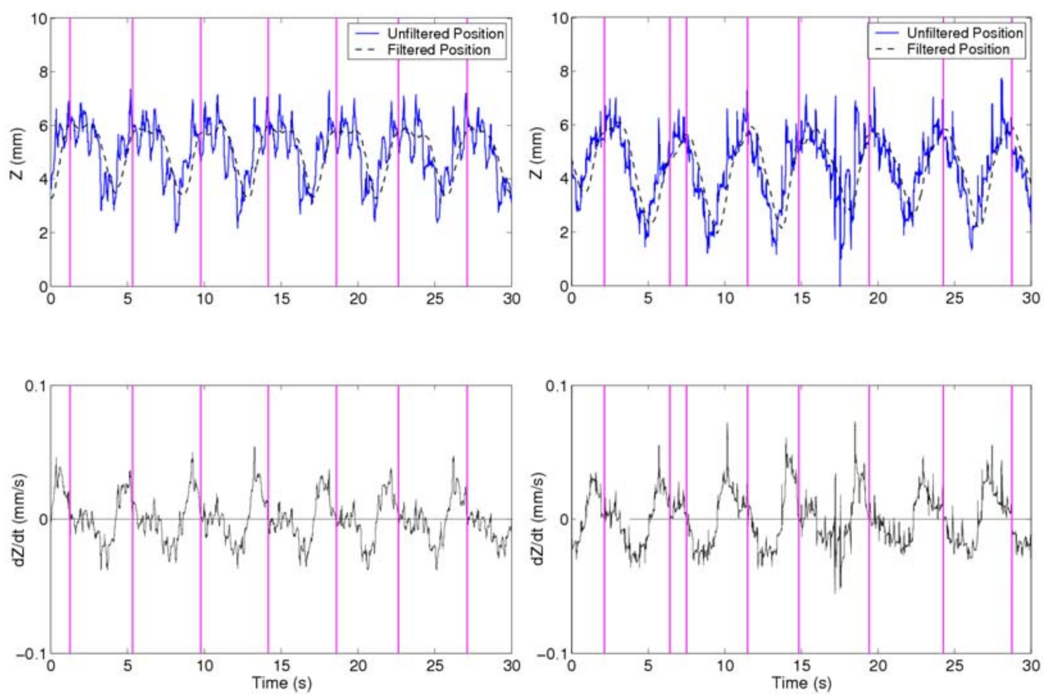

Figure 6.15: The upper plots show the unfiltered (solid line) and low-pass filtered (broken line) position data along the z-axis with the robot resting on the left-lateral (left plot) and the left-posterior (right plot) surfaces of the beating heart. The end-expiration resting periods correspond with the plateaus in the filtered data. The lower plots show the time derivative of the low-pass filtered z-position data for the left-lateral (left plot) and left-posterior (right plot) locations. These data were used by the synchronization detection algorithm to identify the end-expiration events. The end-expiration events are shown by the vertical magenta lines.

6.5.2 Locomotion Synchronization Testing Results

The synchronization event detection algorithm accurately detected the EE phase of respiration on the lateral wall of the right ventricle during locomotion using the onboard robot tracking sensor. The upper plots of Figure 6.15 show the antero-posterior (A-P) data from the electromagnetic tracking sensor onboard HeartLander. Recall that the z-axis is positive toward the posterior of the animal (i.e., the floor); therefore, the EE period occurs when the z-position data reaches its plateau during the respiration cycle. The velocity of the low-pass filtered A-P data is shown in the lower plots of Figure 6.15. The EE events were detected as velocity zero-crossings where the previous data were positive for at least 0.6 s. The EE events shown by the vertical lines in Figure 6.15 are correct, with the exception of the false positive detection around 7.5 s in the two right-hand plots. Table 6.4 shows the percentages of extension step motions, retraction step motions, and both motions that were correctly synchronized with the EE rest periods during locomotion on the lateral wall of the right ventricle of a beating porcine heart. The numbers of correct synchronized stepping motions are shown in parentheses. The percentage of correctly synchronized stepping motions (extensions and retractions) was 68% when synchronization was inactive, and 96% when active. A single step (extension and retraction) correctly synchronized with the EE rest period can be seen in Figure 6.16.

Table 6.4: The percentages of extensions, retractions, and both motions that were correctly synchronized with the end-expiration rest periods during locomotion on a beating porcine heart. The numbers of correct synchronized stepping motions are shown in parentheses. Nine trials were performed with the synchronization inactive and active, with six steps per trial.

Location	Correct Sync Rate: Ext (#)	Correct Sync Rate: Ret (#)	Correct Sync Rate: Both (#)
Sync OFF (n = 9)	64 % (34)	74 % (39)	68 % (73)
Sync ON (n = 9)	96 % (52)	96 % (52)	96 % (104)

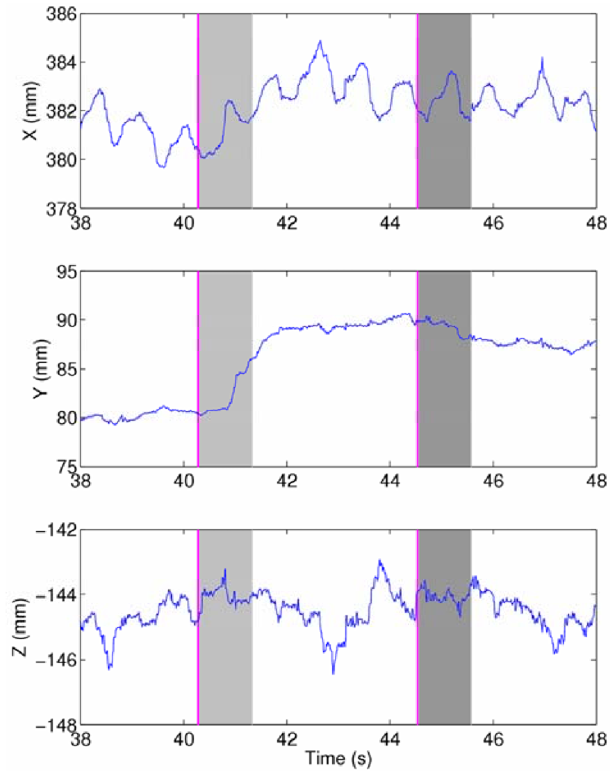

Figure 6.16: The position data from the robot tracking sensor during locomotion synchronized with the end-expiration (EE) rest periods of respiration. The synchronization events are shown by the vertical lines, while the extension duration is shown by the light gray window, and the retraction duration is shown by the darker gray window. Note that both stepping motions occur when the z-position of the robot is at a plateau, indicating the EE rest period of respiration, and correct synchronization.

Contrary to our hypothesis, the extension, retraction, and step efficiencies did not statistically increase when synchronized to the EE rest period of respiration. Figure 6.17 shows the extension efficiencies for each individual trial (upper-left frame) and averaged over all trials (lower-left frame). Figure 6.17 also shows the retraction efficiencies for each individual trial (upper-right frame) and averaged over all trials (lower-right frame). Although it can be seen that the average efficiency for both extension and retraction was greater with synchronization active for the first five steps, this did not generate a statistically significant result. The means, standard deviations, and Mann-Whitney-Wilcoxon p-values for all locomotion parameters can be found in Table 6.5. Additionally, there was no change in the average peak extension or retraction forces with synchronization (Figure 6.18).

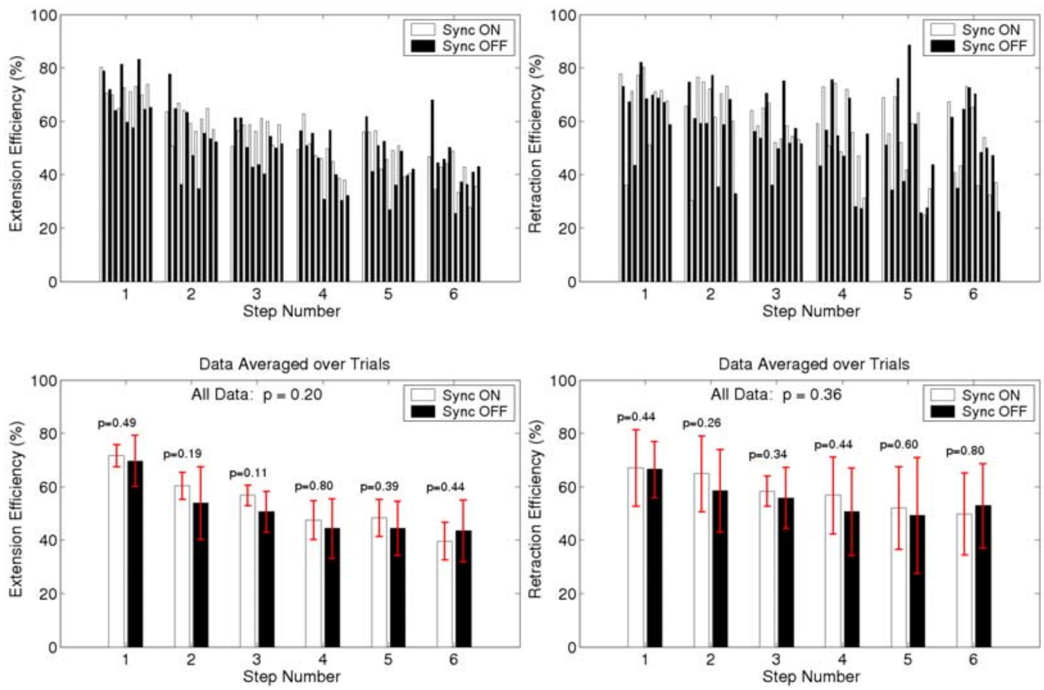

Figure 6.17: The extension efficiencies (left plots) and retraction efficiencies (right plots) for the locomotion synchronization (white) and control (black) testing. The upper plots show the efficiencies for all trials, while the lower plots show the results averaged over all trials.

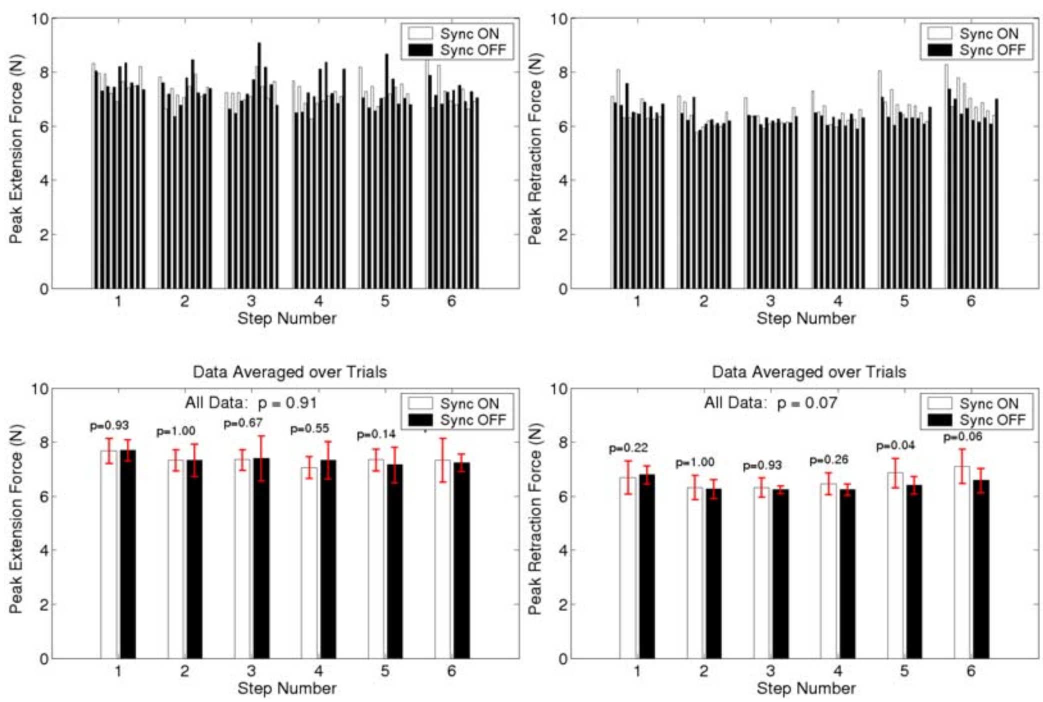

Figure 6.18: The extension peak forces (left plots) and retraction peak forces (right plots) for the locomotion synchronization (white) and control (black) testing. The upper plots show the peak forces for all trials, while the lower plots show the results averaged over all trials.

Table 6.5. The locomotion parameters for the stepping synchronization trials (N=9) and control trials (N=9) performed on the lateral wall of the right ventricular surface of the beating heart. The p-values were determined using the Mann-Whitney-Wilcoxon test.

Step Sync	Extension Efficiency (%)	Retraction Efficiency (%)	Step Efficiency (%)	Step Length (mm)	Step Progress (mm)	Extension Force (N)	Retraction Force (N)
Off	51 ± 14	56 ± 16	29 ± 13	5.2 ± 2.8	31 ± 5	7.4 ± 0.6	6.4 ± 0.4
On	54 ± 12	58 ± 14	33 ± 13	5.5 ± 2.8	33 ± 4	7.4 ± 0.5	6.6 ± 0.6
p	0.20	0.36	0.16	0.45	0.49	0.93	0.07

6.5.3 Locomotion Synchronization Discussion

Although the extension and retraction stepping motions were correctly synchronized with an accuracy of 96%, none of the evaluated locomotion parameters (e.g., efficiency, peak force) demonstrated a statistically significant change due to synchronization with respiration. The average extension, retraction, and step efficiency increased slightly with synchronization, but the increases were not statistically significant. This result is further enforced by the lack of change in the average measured extension and retraction peak force with synchronization, which we hypothesized would decrease when locomotion was synchronized with the EE rest periods. We believe that these results demonstrate that the anatomical changes that occur with respiration (described in Section 5.3.2) are not significant enough alone to reduce the pericardial pressure, and thus friction force, experienced by the HeartLander crawler in situ. In the future, we will synchronize the extension and retraction stepping motions with both the heartbeat and respiration phases. In this manner, we hope to take advantage of the natural fluctuations in the anatomical factors contributing to the normal pressure exerted on the crawler to improve locomotion efficiency.

Chapter 7

Preclinical Results In Vivo

The results presented in Chapter 6 illustrate the ability of HeartLander to semi-autonomously acquire targets located around the entire circumference of the ventricles of a beating porcine model in a precise and stable manner. These goals were derived from the tasks required to complete three initial intrapericardial therapies envision for administration from HeartLander: myocardial injection of regenerative materials, epicardial lead placement, and epicardial ablation. In principle, each of these therapies can be effectively performed using the target acquisition abilities demonstrated in Chapter 6. To complete the demonstration of HeartLander's utility, this chapter presents proof of concept testing with the end effectors required for each of these therapies. It should also be emphasized that although we have successfully demonstrated the use of therapeutic end effectors for all three of the aforementioned therapies, these were feasibility studies that did not produce a medical result in the animal models.

7.1 Myocardial Injections of Dye

Following each of the target acquisitions described in Section 6.4, an injection of 0.10 mL of oil-based dye was performed using the remote injection system. For the pattern on the anterior surface of the heart, 8 out of 9 targeted injections successfully penetrated into the myocardium leaving a 6-mm diameter dye mark visible on the epicardium (Figure 7.1). The pressure data from the injection that failed to leave an epicardial mark indicated that the front suction chamber had grip of the epicardium during the injection. Additionally, a small needle stick was visible around the location where the failed injection should have occurred. It is likely that the needle penetrated into the cardiac vasculature beneath this target location, and that the dye was carried away into the blood steam rather than dispersing into the myocardium. For the successful myocardial injections, the dye penetration depth ranged from 3 – 7 mm, with an average penetration of 5 mm. This depth was sufficient to penetrate the entire myocardial wall thickness of the left ventricle in several locations (Figure 7.2). For the pattern on the posterior surface of the heart, all 8 targeted injections successfully penetrated into the myocardium leaving a 6-mm diameter dye mark visible on the epicardium (Figure 7.3). The average dye penetration depth for this pattern was 3.6 mm.

The remote injection system demonstrated a 100% injection success rate for the 17 target sites described in Section 6.4, with one injection accidentally performed into cardiac vasculature rather than the myocardium. After the targeting control system is properly integrated with preoperative or intraoperative imaging that shows the locations of the cardiac vasculature, injections into the cardiac vasculature will be avoided. The injection depths were sufficient for the clinical injection of regenerative materials.

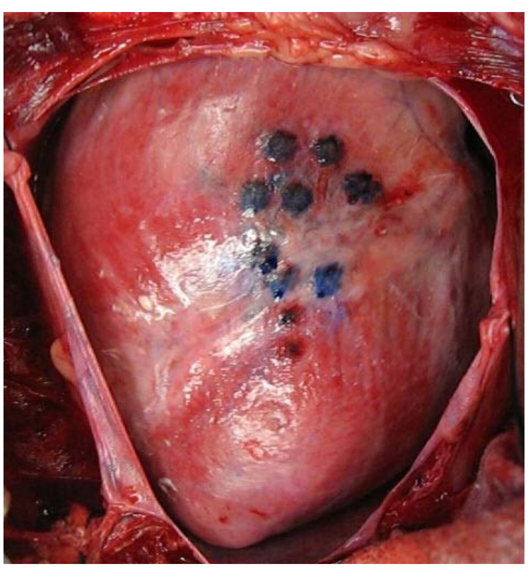

Figure 7.1: Photograph of the anterior injection pattern with the chest opened and pericardium removed after testing. 8 out of the 9 injections were successfully made into the myocardium.

Figure 7.2: Photograph of two of the injection sites from the anterior target pattern, with an incision in the heart wall to reveal the dye penetration depths of 3-5 mm.

Figure 7.3: Photograph of the posterior target injection pattern with the chest opened and pericardium removed following testing. All 8 injections were successful.

7.2 Epicardial Pacing Lead Placement

The deployment of a pacing lead was demonstrated with a larger version of the third HeartLander prototype that was equipped with the CCD camera and the remote epicardial lead placement system (Figure 7.4). The device was inserted onto the apex of the heart in the manner described above, and walked to the targeted posterior wall. The pacing lead was advanced toward the epicardial surface using the guide wire, screwed down into the myocardium, and released from the HeartLander front body. The successful placement of the lead was confirmed by fluoroscopy (Figure 7.4) and actual electrical pacing tests with a threshold of 0.5mV/0.5ms (Figure 7.5) [15]. The electromagnetic tracking system was also used to record the 6 degree of freedom coordinates of the robot during navigation. No adverse hemodynamic or electrophysiologic events were noted during the trial. A histological study of the excised heart was performed to verify that no epicardial damage was caused by the locomotion. This approach may be useful for epicardial LV lead placement for cardiac resynchronization therapy.

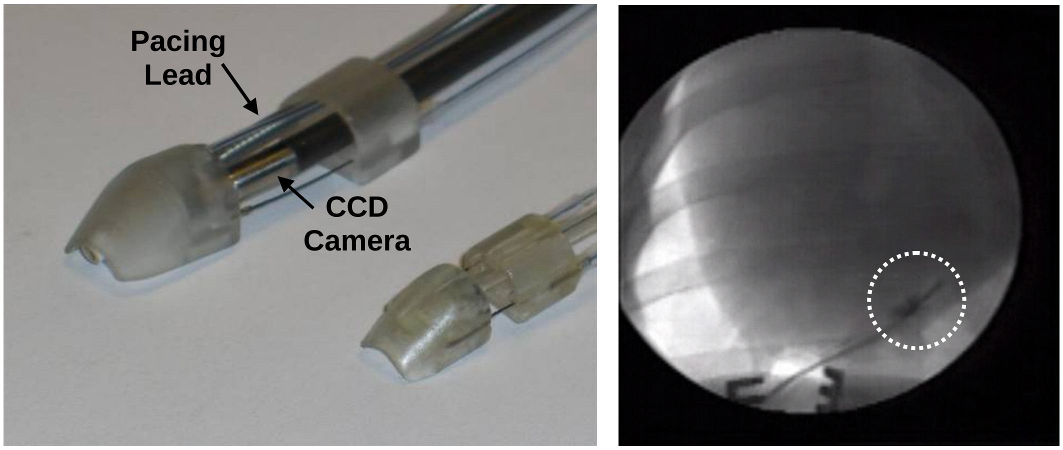

Figure 7.4: (left) The third HeartLander prototype, and an enlarged version to carry the CCD camera and remote epicardial lead placement system. (right) Verification of the location and successful attachment of the epicardial lead on the poster wall of the left ventricle using fluoroscopy (x-ray video). HeartLander highlighted by circle.

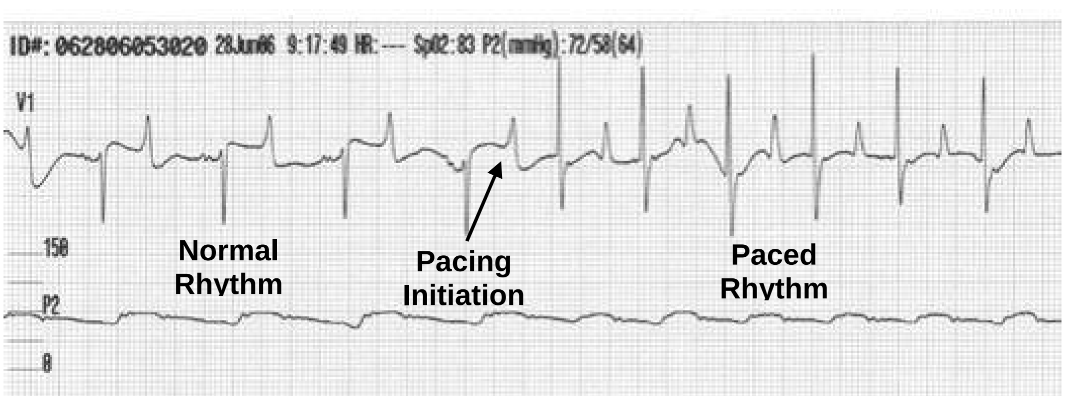

Figure 7.5: An ECG recording showing successful pacing of the heart using the epicardial lead placed by HeartLander. Notice the transition from the natural ECG signal on the left to the paced rhythm on the right.

7.3 Tissue Ablation

Spot ablations were performed on an open-chest beating porcine heart using a commercial ablation catheter deployed from a third-generation crawler that was designed to carry larger payloads. The ablation catheter used was a 5F (1.65-mm diameter) Biosense Webster™ A-type electrophysiology catheter with a 3-mm deflectable RF ablation tip. The catheter was deployed through the working channel of the crawler (Figure 7.6). The robot also contained a 1.8-mm diameter low-resolution fiberscope with a built-in light guide to provide visualization of the ablation tip.

The spot ablations were performed with the chest opened. The pericardium was intact for half of the ablations (N=2), while it was removed for the other half (N=2) to allow direct visualization of the ablated regions. The ablations were performed for 30 s at 30 W, with saline irrigation prior to the applications. Examination of the ablations following the excision of the heart revealed that all ablations were successful (Figure 7.7).

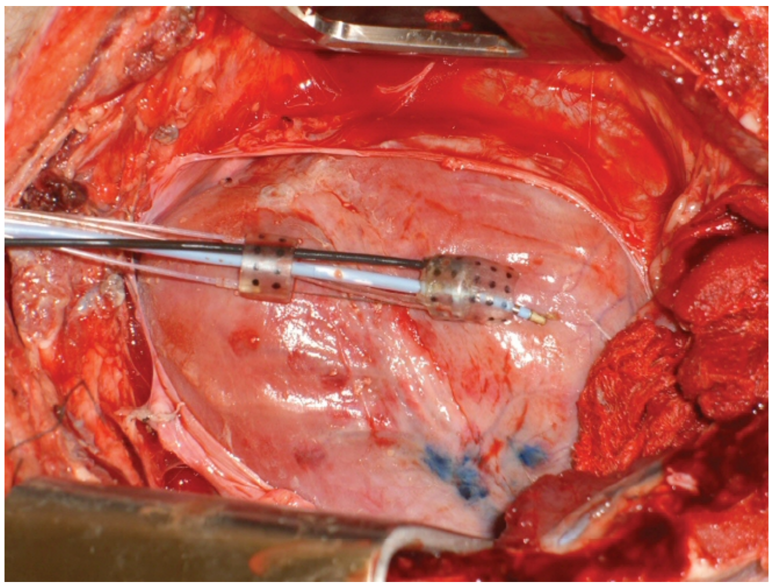

Figure 7.6: Photograph of the larger HeartLander prototype deploying a commercial ablation catheter to the epicardial surface of the right atrium of a beating porcine heart.

Figure 7.7: Photograph of the excised porcine heart showing three spot ablations performed on the right atrium with the heart beating and pericardium intact.

7.4 Electrophysiological Sensing

A bipolar electrode was fabricated using two Ethicon™ temporary cardiac pacing wires with multifilament surgical steel constructions. The wires were attached to the bottom of the HeartLander front body, located 6 mm from one another (Figure 7.8). Contact between the electrodes and the epicardium was maintained by the suction chamber located between the electrodes. With the chest closed, the surgeon placed the robot at 13 distinct locations on the heart surface through the subxiphoid incision. The activation time was calculated from the ECG signal by an electrophysiologist at each site, and the corresponding 3-D location of the robot from the electromagnetic tracking sensor was also recorded (Figure 7.9). The facets of the heart surface model were then assigned the activation value equal to the activation reading with the closest distance from the facet. In this manner, a crude activation map of the heart model was generated (Figure 7.10). In the future, bipolar electrodes mounted into the HeartLander crawlers can help to locate diseased regions of the heart during a procedure.

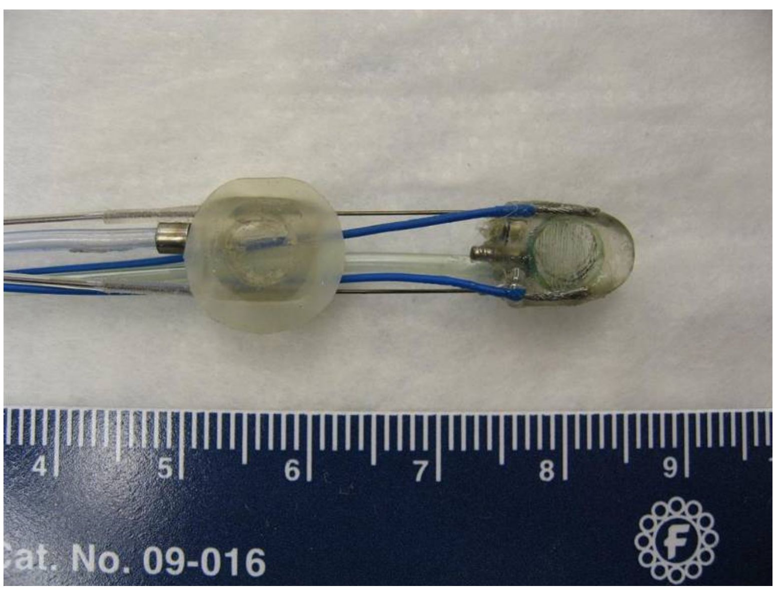

Figure 7.8: Photograph of the HeartLander prototype with a custom bipolar electrode mounted to the bottom surface of the robot for the measure of the electrical excitation of the heart in situ during locomotion.

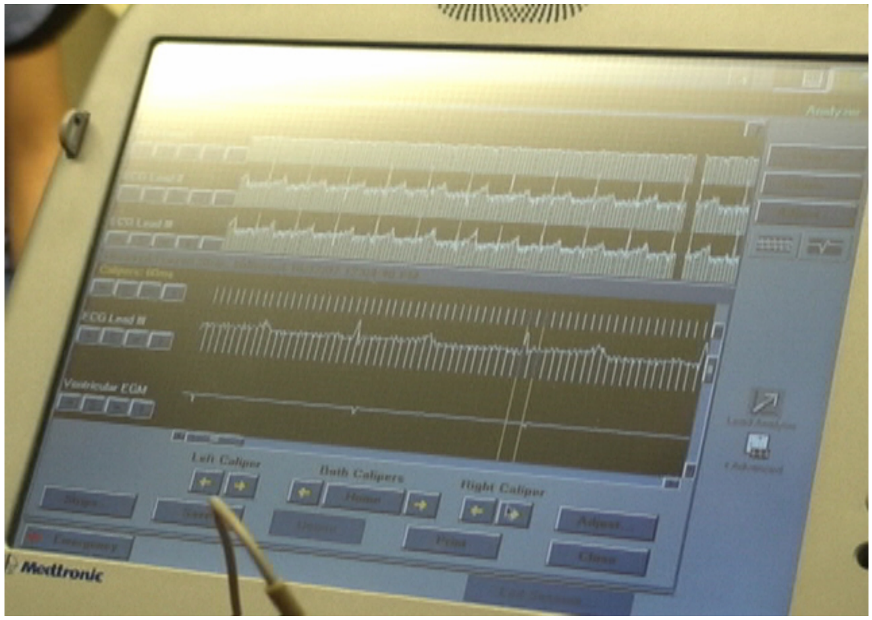

Figure 7.9: Photograph showing the electrocardiogram (ECG) reading from the custom HeartLander bipolar electrode measured from the epicardial surface of the heart in situ.

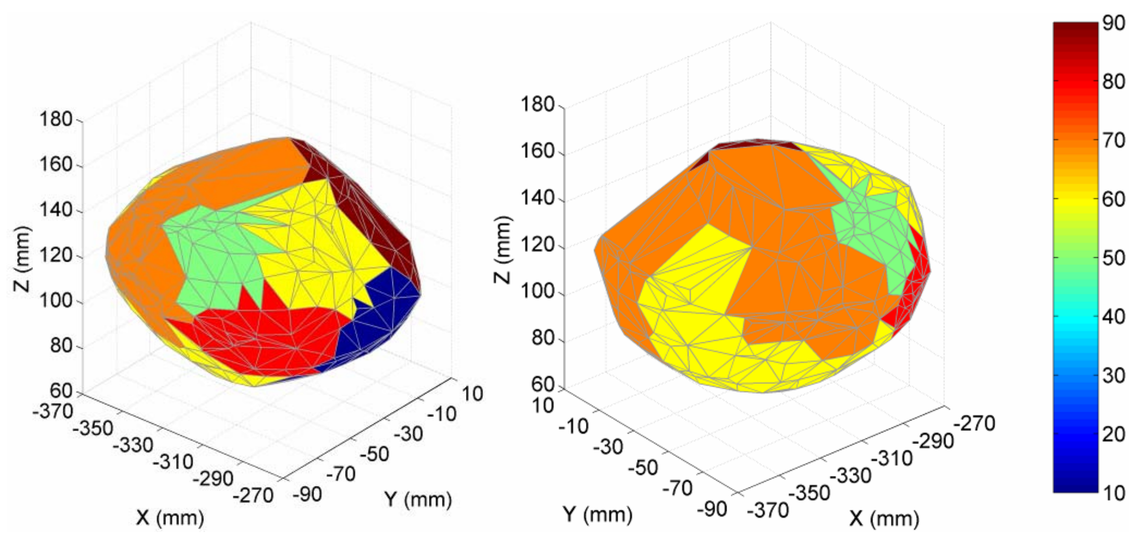

Figure 7.10: A heart surface model with the facets colored to indicate the activation reading from the bipolar electrode that was measured from the location closest to the facet. In this manner, the epicardial bipolar electrode readings were used to generated a course activation map of the heart model.

7.5 Epicardial Echocardiography

As a proof of concept, a commercial intracardiac echocardiography (ICE) catheter was used to image the internal structure of a beating porcine heart from the intrapericardial space onboard HeartLander. The chest was closed and pericardium intact for this experiment. The ICE catheter was a disposable 8F (2.7-mm diameter) ACUSON AcuNav™ planar diagnostic ultrasound catheter. The catheter was deployed through the working channel of the larger third-generation crawler. The left atrium (LA), left ventricle (LV), and mitral valve (MV) were clearly visible on the ultrasound monitor, despite the lower quality of the image due to the inability to guarantee close contact between the catheter tip and epicardium (Figure 7.11).

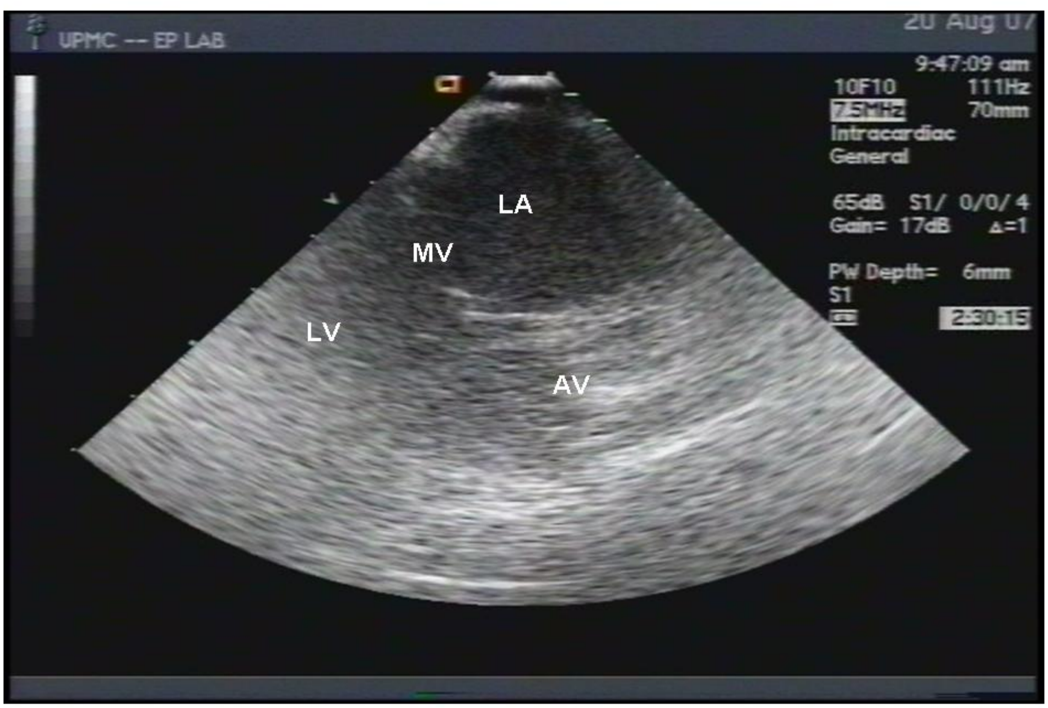

Figure 7.11: Screenshot from the ultrasound monitor displaying the output from a commercial intracardiac echocardiography (ICE) catheter that was used to image the internal structure of a beating porcine heart from the intrapericardial space onboard HeartLander. The left atrium (LA), left ventricle (LV), and mitral valve (MV) were visible on the ultrasound monitor.

Chapter 8

Conclusion

HeartLander is a miniature mobile robot designed to provide enhanced access for minimally invasive cardiac intervention by traversing the epicardial surface of the beating heart in situ. Numerous cardiac therapies can be administered from within the intrapericardial space surrounding the heart, through a series of treatments applied to the epicardial surface in a controlled fashion. Accordingly, the design of the robot and control system presented in this thesis were directly motivated by the goal of providing precise and stable target acquisition over the entire epicardial surface of the heart. The evaluation of HeartLander through a series of studies on a closed-chest beating porcine model demonstrated its ability to traverse the entire surface of the ventricles, acquire clinically relevant target patterns with sub-millimeter accuracy, and maintain stability with the epicardial surface. In combination with the feasibility studies conducted using several therapeutic end-effectors, HeartLander has demonstrated the ability to provide enhanced minimally invasive access to the epicardium for intrapericardial intervention. In the future, this system may prove a useful tool for both cardiac surgeons and cardiologists.

8.1 Summary

In this thesis, we demonstrated that the development of a miniature mobile robot (HeartLander) that adheres to and traverses the epicardium provides a tool for precise and stable interaction with the beating heart. The ability of the robot to adhere to the epicardium obviates the need for cardiopulmonary bypass or mechanical stabilization, while the mobility overcomes access limitations that currently limit thoracoscopic techniques. Additionally, the ability of HeartLander to be deployed to the apex of the heart through a percutaneous subxiphoid approach obviates differential ventilation and left lung deflation, which may enable cardiac surgeons to provide outpatient procedures.

To demonstrate the utility of HeartLander, we focused on a subset three intrapericardial therapies that require precise and stable treatments at multiple sites on the surface of the heart: myocardial injection of regenerative materials, epicardial lead placement, and epicardial ablation. To facilitate these clinical tasks, HeartLander provides access over the entire epicardium, precise positioning to selected targets, and ensures safe and stable interaction with the surface of the beating heart. To minimize the associated morbidity, the robot achieves these goals with the chest closed, the pericardium intact, and the heart beating. Through a series of closed-chest, beating-heart porcine studies, HeartLander demonstrated navigation over the entire circumference of the heart, the acquisition of targets within 1.0 mm, and stability with residual motion less than 1.0 mm. Accordingly, the design of the robot and control system met the requirements motivated by our clinical goals.

The novel HeartLander paradigm combines the tracking techniques, anatomical models, and minimal access morbidity of transvenous procedures with the epicardial access and fine control of thoracoscopic techniques. A hybrid device of this nature may provide advantages over current approaches within the field of cardiac care for certain procedures.

8.2 Contributions

- **Development of a mobile robot to access the entire epicardium**. The miniature size of the HeartLander crawler permits it to travel beneath the intact pericardium to reach any location on the surface of the beating heart through a small subxiphoid percutaneous and pericardial incisions. The navigation system has demonstrated locomotion to points around the entire circumference of the heart. Thus, HeartLander provides total epicardial access thorough a minimally invasive approach.

- **Development of a positioning system with high accuracy on the beating heart**. The drive-wire mechanism, suction-based prehension, and real-time filtering allow HeartLander to act as a manipulator for reaching a series of target locations in distal regions on the beating heart. The accuracy of the positioning system has demonstrated positioning errors less than 1.0 mm on the beating heart with the chest closed.
- **Platform stability beyond the current capabilities of mechanical stabilizers**. The miniature size and prehension capabilities of HeartLander allow the robot to remain fixed on the surface of the heart without being displaced by the shearing motion of the pericardium relative to the heart. The robot has demonstrated resultant maximum 3-D displacement of less than 1.0 mm over a period of 30 s around the entire circumference of the heart. This resultant drift is less than that provided by commercial mechanical stabilizers currently used in beating-heart surgery.
- **Application of pure pursuit to a new mobile robot domain**. The pure pursuit path tracking algorithm has been adapted from use in wheeled mobile robots to the wire-driven HeartLander crawler traveling on the beating heart. The incremental goal steps generated by the tracking algorithm were fed to the inverse kinematics of the wire actuation for step planning to the target location along the desired path.
- **Development of a novel method for generating a registered surface model**. A surface tracing methodology was developed to provide a still 3-D reconstruction of the beating heart surface through a subxiphoid incision. This model was automatically registered within the tracking system used by the robot during navigation. The technique takes the surgeon and engineer less than 30 minutes to complete, and required no preoperative or intraoperative radiation-based imaging.
- **The design and construction of three generations of crawlers**. Three distinct generations of crawlers have been developed and tested in vivo. Each crawler was built to overcome difficulties encountered by its predecessor, improving epicardial access and requiring less invasive approaches. The third generation crawler is capable of accessing the entire epicardial surface of the beating heart through a subxiphoid percutaneous incision.
- **Demonstration of sample therapy administration from robot platform**. The remote injection system permitted the surgeon to inject dye into the myocardium through the working

channel of the robot. Dye was used to simulate regenerative material injection, and to validate the location of the robot on the heart during target acquisition trials. Additionally, a commercial pacing lead and ablation catheter designed for transvenous application were successfully applied to the epicardium using HeartLander through a subxiphoid percutaneous incision. In combination with the navigation capabilities of HeartLander, this represents a highly accurate therapeutic system.

8.3 Future Work

Several improvements to the design of the robot and control system are necessary to prepare HeartLander for clinical use. One critical area of future research will focus on improving motion efficiency during both navigation and fine-positioning, thereby lowering the average target acquisition time. Efficiency can be improved by further reducing the profile of the crawler robot, thus lowering the friction forces exerted by the pericardium on the robot. Safe lubricants, such as saline, could also be secreted by the crawler bodies immediately prior to stepping motions to attempt to lower friction with the environment. Although the coordination of the stepping motions with respiration did not yield an improvement in efficiency, coordination with the heartbeat cycle may generate results. The heart volume and position vary greatly over the cycle, and anecdotal evidence suggests that these factors may influence the normal force of the pericardium on HeartLander. The main challenge will be to accurately detect the optimal phase of the heartbeat cycle for stepping, and to complete the stepping motion within that region. The high and varying frequency of the heartbeat will make these tasks nontrivial.

Within the control system, a more sophisticated planner will be necessary in order to treat diseased regions on the heart as obstacles and avoid them during navigation. The planner should also be used to generate a complete plan to acquire the entire series of targets located on the heart, rather than treating each target as a separate trial. In this manner, the targets can be acquired in more efficient manner.

From a clinical standpoint, both the therapeutic and diagnostic capabilities of HeartLander must be further developed. One of the most exciting future applications is to mount diagnostic sensors as well as therapeutic end-effectors onboard the robot. HeartLander could then provide direct measurements from the heart that contribute to the diagnosis and planning of treatment, perform the designed treatment, then make additional sensor readings to validate the treatment.

Devices with the functionality to diagnose, treat, and validate are highly desirable in the health-care industry. Additionally, high-quality pre-operative imaging, such as computerized tomography or magnetic resonance imaging, must be integrated into the graphical interface. When properly registered, this will allow the surgeon to see details, such as the coronary arteries, on the graphical display that shows the current location of the robot.

Bibliography

[1] D. N. Feldman, C. L. Gade, A. J. Slotwiner, M. Parikh, G. Bergman, S. C. Wong, and R. M. Minutello, "Comparison of outcomes of percutaneous coronary interventions in patients of three age groups (<60, 60 to 80, and >80 years) (from the New York State Angioplasty Registry)," *Am J Cardiol,* vol. 98, pp. 1334-9, Nov 15 2006.

[2] R. Cappato, H. Calkins, S. A. Chen, W. Davies, Y. Iesaka, J. Kalman, Y. H. Kim, G. Klein, D. Packer, and A. Skanes, "Worldwide survey on the methods, efficacy, and safety of catheter ablation for human atrial fibrillation," *Circulation,* vol. 111, pp. 1100-5, Mar 8 2005.

[3] W. H. Maisel, "Transvenous implantable cardioverter-defibrillator leads: the weakest link," *Circulation,* vol. 115, pp. 2461-3, May 15 2007.

[4] W. E. Boden, R. A. O'Rourke, K. K. Teo, P. M. Hartigan, D. J. Maron, W. J. Kostuk, M. Knudtson, M. Dada, P. Casperson, C. L. Harris, B. R. Chaitman, L. Shaw, G. Gosselin, S. Nawaz, L. M. Title, G. Gau, A. S. Blaustein, D. C. Booth, E. R. Bates, J. A. Spertus, D. S. Berman, G. B. Mancini, and W. S. Weintraub, "Optimal medical therapy with or without PCI for stable coronary disease," *N Engl J Med,* vol. 356, pp. 1503-16, Apr 12 2007.

[5] R. A. Schweikert, W. I. Saliba, G. Tomassoni, N. F. Marrouche, C. R. Cole, T. J. Dresing, P. J. Tchou, D. Bash, S. Beheiry, C. Lam, L. Kanagaratnam, and A. Natale, "Percutaneous pericardial instrumentation for endo-epicardial mapping of previously failed ablations," *Circulation,* vol. 108, pp. 1329-35, Sep 16 2003.

[6] J. R. Edgerton, Z. J. Edgerton, M. J. Mack, S. Hoffman, T. M. Dewey, and M. A. Herbert, "Ventricular epicardial lead placement for resynchronization by determination of paced depolarization intervals: technique and rationale," *Ann Thorac Surg,* vol. 83, pp. 89-92; discussion 92, Jan 2007.

[7] A. Puglisi, M. Lunati, A. G. Marullo, S. Bianchi, M. Feccia, F. Sgreccia, I. Vicini, S. Valsecchi, F. Musumeci, and E. Vitali, "Limited thoracotomy as a second choice alternative to transvenous implant for cardiac resynchronisation therapy delivery," *Eur Heart J,* vol. 25, pp. 1063-9, Jun 2004.

[8] E. A. Bacha, S. Daves, J. Hardin, R. I. Abdulla, J. Anderson, M. Kahana, P. Koenig, B. N. Mora, M. Gulecyuz, J. P. Starr, E. Alboliras, S. Sandhu, and Z. M. Hijazi, "Single-ventricle palliation for high-risk neonates: the emergence of an alternative hybrid stage I strategy," *J Thorac Cardiovasc Surg,* vol. 131, pp. 163-171 e2, Jan 2006.

[9] C. Borst, E. W. Jansen, C. A. Tulleken, P. F. Grundeman, H. J. Mansvelt Beck, J. W. van Dongen, K. C. Hodde, and J. J. Bredee, "Coronary artery bypass grafting without cardiopulmonary bypass and without interruption of native coronary flow using a novel anastomosis site restraining device ("Octopus")," *J Am Coll Cardiol,* vol. 27, pp. 1356-64, May 1996.

[10] E. W. Jansen, J. R. Lahpor, C. Borst, P. F. Grundeman, and J. J. Bredee, "Off-pump coronary bypass grafting: how to use the Octopus Tissue Stabilizer," *Ann Thorac Surg,* vol. 66, pp. 576-9, Aug 1998.

[11] V. Falk, A. Diegler, T. Walther, R. Autschbach, and F. W. Mohr, "Developments in robotic cardiac surgery," *Curr Opin Cardiol,* vol. 15, pp. 378-87, Nov 2000.

[12] M. A. Zenati, G. Bonanomi, A. K. Chin, and D. Schwartzman, "Left heart pacing lead implantation using subxiphoid videopericardioscopy," *J Cardiovasc Electrophysiol,* vol. 14, pp. 949-53, Sep 2003.

[13] K. Soejima, G. Couper, J. M. Cooper, J. L. Sapp, L. M. Epstein, and W. G. Stevenson, "Subxiphoid surgical approach for epicardial catheter-based mapping and ablation in patients with prior cardiac surgery or difficult pericardial access," *Circulation,* vol. 110, pp. 1197-201, Sep 7 2004.

[14] T. Ota, N. A. Patronik, C. N. Riviere, and M. A. Zenati, "Minimally invasive epicardial injection using a miniature crawling robotic device through a subxiphoid approach," *Proceeding, The American Heart Association Scientific Sessions,* In press 2007.

[15] T. Ota, N. A. Patronik, D. Schwartzman, C. N. Riviere, and M. A. Zenati, "Subxiphoid epicardial pacing lead implantation using a miniature crawling robotic device," *The Journal of surgical research,* vol. 137, pp. 242-243, 2007 2007.

[16] N. A. Patronik, M. A. Zenati, and C. N. Riviere, "Preliminary evaluation of a mobile robotic device for navigation and intervention on the beating heart," *Comput Aided Surg,* vol. 10, pp. 225-32, Jul 2005.

[17] V. B. Kim, W. H. Chapman, R. J. Albrecht, B. M. Bailey, J. A. Young, L. W. Nifong, and W. R. Chitwood, Jr., "Early experience with telemanipulative robot-assisted laparoscopic cholecystectomy using da Vinci," *Surg Laparosc Endosc Percutan Tech,* vol. 12, pp. 33-40, Feb 2002.

[18] V. Ficarra, S. Cavalleri, G. Novara, M. Aragona, and W. Artibani, "Evidence from robot-assisted laparoscopic radical prostatectomy: a systematic review," *Eur Urol,* vol. 51, pp. 45-55; discussion 56, Jan 2007.

[19] R. Ascione, C. T. Lloyd, M. J. Underwood, A. A. Lotto, A. A. Pitsis, and G. D. Angelini, "Inflammatory response after coronary revascularization with or without cardiopulmonary bypass," *Ann Thorac Surg,* vol. 69, pp. 1198-204, Apr 2000.

[20] M. J. Mack, "Minimally invasive and robotic surgery," *JAMA,* vol. 285, pp. 568-72, Feb 7 2001.

[21] P. Cattin, H. Dave, J. Grunenfelder, G. Szekely, M. Turina, and G. Zund, "Trajectory of coronary motion and its significance in robotic motion cancellation," *Eur J Cardiothorac Surg,* vol. 25, pp. 786-90, May 2004.

[22] T. H. Liem, L. H. Booij, M. A. Hasenbos, and M. J. Gielen, "Coronary artery bypass grafting using two different anesthetic techniques: Part I: Hemodynamic results," *J Cardiothorac Vasc Anesth,* vol. 6, pp. 148-55, Apr 1992.

[23] J. P. Williams, E. A. Sullivan, and H. Ramakrishna, "Effects of thoracic epidural anesthesia on the coagulation system," *Clinical Anesthesia,* vol. 13, pp. 31-56, 1999.

[24] M. F. Newman, J. L. Kirchner, B. Phillips-Bute, V. Gaver, H. Grocott, R. H. Jones, D. B. Mark, J. G. Reves, and J. A. Blumenthal, "Longitudinal assessment of neurocognitive function after coronary-artery bypass surgery," *N Engl J Med,* vol. 344, pp. 395-402, Feb 8 2001.

[25] V. Falk, A. Diegeler, T. Walther, N. Loscher, B. Vogel, C. Ulmann, T. Rauch, and F. W. Mohr, "Endoscopic coronary artery bypass grafting on the beating heart using a computer enhanced telemanipulation system," *Heart Surg Forum,* vol. 2, pp. 199-205, 1999.

[26] P. F. Grundeman, R. Budde, H. M. Beck, W. J. van Boven, and C. Borst, "Endoscopic exposure and stabilization of posterior and inferior branches using the endo-starfish cardiac positioner and the endo-octopus stabilizer for closed-chest beating heart multivessel CABG: hemodynamic changes in the pig," *Circulation,* vol. 108 Suppl 1, pp. II34-8, Sep 9 2003.

[27] R. Dzwonczyk, C. L. del Rio, C. Sai-Sudhakar, J. H. Sirak, R. E. Michler, B. Sun, N. Kelbick, and M. B. Howie, "Vacuum-assisted apical suction devices induce passive electrical changes consistent with myocardial ischemia during off-pump coronary artery bypass graft surgery," *Eur J Cardiothorac Surg,* vol. 30, pp. 873-6, Dec 2006.

[28] S. Kinjo, J. Tokumine, K. Sugahara, M. Kakinohana, K. Iha, H. Matsuda, M. Akasaki, and S. Yamashiro, "Unexpected hemodynamic deterioration and mitral regurgitation due to a tissue stabilizer during left anterior descending coronary anastomosis in off-pump coronary artery bypass graft surgery," *Ann Thorac Cardiovasc Surg,* vol. 11, pp. 324-8, Oct 2005.

[29] M. Lemma, A. Mangini, A. Redaelli, and F. Acocella, "Do cardiac stabilizers really stabilize? Experimental quantitative analysis of mechanical stabilization," *Interact Cardiovasc Thorac Surg,* vol. 4, pp. 222-6, Jun 2005.

[30] M. L. Koransky, M. L. Tavana, A. Yamaguchi, M. H. Kown, D. N. Miniati, W. Nowlin, and R. C. Robbins, "Quantification of mechanical stabilization for the performance of off-pump coronary artery surgery," *Heart Surg Forum,* vol. 6, pp. 224-31, 2003.

[31] O. Bebek and M. C. Cavusoglu, "Intelligent control algorithms for robotic-assisted beating heart surgery," *Robotics, IEEE Transactions on [see also Robotics and Automation, IEEE Transactions on],* vol. 23, pp. 468-480, 2007.

[32] J. Gangloff, R. Ginhoux, M. d. Mathelin, L. Soler, and J. Marescaux, "Model predictive control for compensation of cyclic organ motions in teleoperated laparoscopic surgery," *IEEE transactions on control systems technology : a publication of the IEEE Control Systems Society,* vol. 14, p. 12, 2006 2006.

[33] R. Ginhoux, J. Gangloff, M. de Mathelin, L. Soler, M. M. A. Sanchez, and J. Marescaux, "Active filtering of physiological motion in robotized surgery using predictive control," *IEEE transactions on robotics : a publication of the IEEE Robotics and Automation Society,* vol. 21, pp. 67-79, 2005 2005.

[34] M. Sitti, "Piezoelectrically actuated four-bar mechanism with two flexible links for micromechanical flying insect thorax," *Mechatronics, IEEE/ASME Transactions on,* vol. 8, pp. 26-36, Mar 2003 2003.

[35] T. Mei, Y. Chen, G. Fu, and D. Kong, " Wireless drive and control of a swimming microrobot," *Robotics and Automation, 2002. Proceedings. ICRA '02. IEEE International Conference on,* pp. 1131-1136, 2002.

[36] H. Herr and B. Dennis, "A Swimming Robot Actuated by Living Muscle Tissue," *Journal of NeuroEngineering and Rehabilitation,* 2004.

[37] G. Caprari, T. Estier, and R. Siegwart, "Fascination of Down Scaling - Alice the Sugar Cube Robot," *Workshop Proceedings on Mobile Micro-Robots, IEEE International Conference on Robotics and Automation,* 2000.

[38] G. Yan and Y. Dai, " A novel biomimetic hexapod micro-robot," *Micromechatronics and Human Science, 2002. MHS 2002. Proceedings of 2002 International Symposium on,* pp. 79-84, 2002.

[39] W. Shen, J. Gu, and Y. Shen, "Proposed wall climbing robot with permanent magnetic tracks for inspecting oil tanks," *Mechatronics and Automation, 2005 IEEE International Conference,* vol. 4, pp. 2072-2077, 29 July-Aug 1 2005 2005.

[40] S. Hirose, *Biologically inspired robots : snake-like locomotors and manipulators*. Oxford ; New York: Oxford University Press, 1993.

[41] R. Tummala, R. Mukherjee, N. Xi., D. Aslam, H. Dulimarta, J. Xiao, M. Minor, and G. Dang, "Climbing the walls [robots]," *Robotics & Automation Magazine, IEEE,* vol. 9, pp. 10-19, 2002.

[42] C. Hillenbrand and K. Berns, "A climbing robot based on under pressure adhesion for the inspection of concrete walls.," *35th Internation Symposium on Robotics (ISR),* p. 119, 2004.

[43] S. Kim, A. T. Asbeck, M. R. Cutkosky, and W. R. Provancher, "SpinybotII: climbing hard walls with compliant microspines," *Adcanced Robotics, 2005, ICAR Proceedings, 12th International Conference on,* pp. 601-606, 2005.

[44] G. C. Haynes and A. A. Rizzi, "Gaits and gait transitions for legged robots," *Robotics and Automation, ICRA 2006. Proceedings 2006 IEEE International Conference on,* pp. 1117- 1122, 2006.

[45] M. Menon, A. Shrivastava, and A. Tewari, "Laparoscopic radical prostatectomy: conventional and robotic," *Urology,* vol. 66, pp. 101-4, Nov 2005.

[46] K. A. Daltorio, A. D. Horchler, S. Gorb, R. E. Ritzmann, and R. D. Quinn, "A small wall walking robot with compliant, adhesive feet," *Intelligent Robots and Systems, (IROS 2005). 2005 IEEE/RSJ International Conference on,* pp. 3648- 3653, 2005.

[47] M. Sitti and R. Fearing, "Synthetic gecko foot-hair micro/nano-structures as dry adhesives," *Journal of Adhesion Science and Technology 17, no,* vol. 8, pp. 1055-1073, 2003.

[48] P. Dario, P. Ciarletta, A. Menciassi, and B. Kim, "Modeling and experimental validation of the locomotion of endoscopic robots in the colon," *The International Journal of Robotics Research,* vol. 23, pp. 549-556, 2004 2004.

[49] B. Kim, M. G. Lee, Y. P. Lee, Y. Kim, and G. Lee, "An earthworm-like micro robot using shape memory alloy actuator," *Sensors and actuators. A, Physical,* vol. 125, p. 9, 2006 2006.

[50] J. Kwon, E. Cheung, S. Park, and M. Sitti, "Friction enhancement via micro-patterned wet elastomer adhesives on small intestinal surfaces," *Biomedical Materials,* vol. 1, pp. 216-220, 2006.

[51] G. Iddan, G. Meron, A. Glukhovsky, and P. Swain, "Wireless capsule endoscopy," *Nature,* vol. 405, p. 417, May 25 2000.

[52] Uehara and Hoshina, "Capsule endoscope NORIKA system," *Minim Invasive Ther Allied Technol,* vol. 12, pp. 227-34, Sep 2003.

[53] Y. Kusuda, "A further step beyond wireless capsule endoscopy," *Sensor Review,* vol. 25, pp. 259-260, 2005 2005.

[54] C. Stefanini, A. Menciassi, and P. Dario, "Modeling and experiments on a legged microrobot locomoting in a tubular, compliant and slippery environment," *The International Journal of Robotics Research,* vol. 25, pp. 551-560, 2006 2006.

[55] M. E. Rentschler, J. Dumpert, S. R. Platt, K. Iagnemma, D. Oleynikov, and S. M. Farritor, "Modeling, analysis, and experimental study of in vivo wheeled robotic mobility," *Robotics, IEEE Transactions on [see also Robotics and Automation, IEEE Transactions on],* vol. 22, pp. 308-321, 2006.

[56] K. L. Moore, A. M. R. Agur, K. L. Moore, and A. M. R. Agur, *Essential clinical anatomy*. Baltimore: Williams & Wilkins, 1996.

[57] R. P. Vito, "The role of the pericardium in cardiac mechanics," *J Biomech,* vol. 12, pp. 587-92, 1979.

[58] H. Kubota, C. Sato, M. Ohgushi, T. Haku, K. Sasaki, and K. Yamaguchi, "Fluid Collection in the Pericardial Sinuses and Recesses: Thin-Section Helical Computed Tomography Observations and Hypothesis," *Investigative radiology,* vol. 31, p. 603 (8 pages), 1996.

[59] W. P. Santamore, M. S. Constantinescu, D. Bogen, and W. E. Johnston, "Nonuniform distribution of normal pericardial fluid," *Basic Res Cardiol,* vol. 85, pp. 541-9, Nov-Dec 1990.

[60] G. Shechter, J. R. Resar, and E. R. McVeigh, "Displacement and velocity of the coronary arteries: cardiac and respiratory motion," *IEEE Trans Med Imaging,* vol. 25, pp. 369-75, Mar 2006.

[61] M. Carlsson, A. Rosengren, M. Ugander, U. Ekelund, P. A. Cain, and H. Arheden, "Center of volume and total heart volume variation in healthy subjects and patients before and after coronary bypass surgery," *Clin Physiol Funct Imaging,* vol. 25, pp. 226-33, Jul 2005.

[62] J. V. Tyberg, G. C. Taichman, E. R. Smith, N. W. Douglas, O. A. Smiseth, and W. J. Keon, "The relationship between pericardial pressure and right atrial pressure: an intraoperative study," *Circulation,* vol. 73, pp. 428-32, Mar 1986.

[63] D. R. Hamilton, R. S. Dani, R. A. Semlacher, E. R. Smith, T. M. Kieser, and J. V. Tyberg, "Right atrial and right ventricular transmural pressures in dogs and humans. Effects of the pericardium," *Circulation,* vol. 90, pp. 2492-500, Nov 1994.

[64] J. A. Faehnrich, R. B. Noone, Jr., W. D. White, B. J. Leone, A. K. Hilton, G. M. Sreeram, and J. B. Mark, "Effects of positive-pressure ventilation, pericardial effusion, and cardiac tamponade on respiratory variation in transmitral flow velocities," *J Cardiothorac Vasc Anesth,* vol. 17, pp. 45-50, Feb 2003.

[65] O. A. Smiseth, C. R. Thompson, H. Ling, M. Robinson, and R. T. Miyagishima, "A potential clinical method for calculating transmural left ventricular filling pressure during positive end-expiratory pressure ventilation: an intraoperative study in humans," *J Am Coll Cardiol,* vol. 27, pp. 155-60, Jan 1996.

[66] T. J. Gilhuly, S. E. Salcudean, K. Ashe, S. Lichtenstein, and P. D. Lawrence, "Stabilizer and surgical arm design for cardiac surgery," *Robotics and Automation, Proceedings. 1998 IEEE International Conference on,* vol. 1, pp. 699-704, 1998.

[67] J. D. Humphrey, *Cardiovascular Solid Mechanics: Cells, Tissues, and Organs*. New York: Springer-Verlang, 2002.

[68] J. D. Humphrey, R. K. Strumpf, and F. C. Yin, "Biaxial mechanical behavior of excised ventricular epicardium," *Am J Physiol,* vol. 259, pp. H101-8, Jul 1990.

[69] M. C. Lee, Y. C. Fung, R. Shabetai, and M. M. LeWinter, "Biaxial mechanical properties of human pericardium and canine comparisons," *Am J Physiol,* vol. 253, pp. H75-82, Jul 1987.

[70] J. Shirani, K. Berezowski, and W. C. Roberts, "Quantitative measurement of normal and excessive (cor adiposum) subepicardial adipose tissue, its clinical significance, and its effect on electrocardiographic QRS voltage," *Am J Cardiol,* vol. 76, pp. 414-8, Aug 15 1995.

[71] G. Iacobellis, D. Corradi, and A. M. Sharma, "Epicardial adipose tissue: anatomic, biomolecular and clinical relationships with the heart," *Nat Clin Pract Cardiovasc Med,* vol. 2, pp. 536-43, Oct 2005.

[72] J. M. Marchington, C. A. Mattacks, and C. M. Pond, "Adipose tissue in the mammalian heart and pericardium: structure, foetal development and biochemical properties," *Comp Biochem Physiol B,* vol. 94, pp. 225-32, 1989.

[73] R. K. Li, Z. Q. Jia, R. D. Weisel, F. Merante, and D. A. Mickle, "Smooth muscle cell transplantation into myocardial scar tissue improves heart function," *J Mol Cell Cardiol,* vol. 31, pp. 513-22, Mar 1999.

[74] D. W. Losordo, P. R. Vale, and J. M. Isner, "Gene therapy for myocardial angiogenesis," *Am Heart J,* vol. 138, pp. S132-41, Aug 1999.
[75] J. D. Gleason, K. P. Nguyen, K. V. Kissinger, W. J. Manning, and R. L. Verrier, "Myocardial drug distribution pattern following intrapericardial delivery: an MRI analysis," *J Cardiovasc Magn Reson,* vol. 4, pp. 311-6, 2002.
[76] C. Leclercq and D. A. Kass, "Retiming the failing heart: principles and current clinical status of cardiac resynchronization," *J Am Coll Cardiol,* vol. 39, pp. 194-201, Jan 16 2002.
[77] R. Lee, T. Nitta, R. B. Schuessler, D. C. Johnson, J. P. Boineau, and J. L. Cox, "The closed heart MAZE: a nonbypass surgical technique," *Ann Thorac Surg,* vol. 67, pp. 1696-702, Jun 1999.
[78] P. Boekstegers, P. Raake, R. Al Ghobainy, J. Horstkotte, R. Hinkel, T. Sandner, R. Wichels, F. Meisner, E. Thein, K. March, D. Boehm, and H. Reichenspurner, "Stent-based approach for ventricle-to-coronary artery bypass," *Circulation,* vol. 106, pp. 1000-6, Aug 20 2002.
[79] M. S. Lee, M. Lill, and R. R. Makkar, "Stem cell transplantation in myocardial infarction," *Rev Cardiovasc Med,* vol. 5, pp. 82-98, Spring 2004.
[80] M. L. Buja and G. R. F. Krueger, *Netter's Illustrated Human Pathology*: Saunders, 2004.
[81] M. Grogan, M. M. Redfield, K. R. Bailey, G. S. Reeder, B. J. Gersh, W. D. Edwards, and R. J. Rodeheffer, "Long-term outcome of patients with biopsy-proved myocarditis: comparison with idiopathic dilated cardiomyopathy," *J Am Coll Cardiol,* vol. 26, pp. 80-4, Jul 1995.
[82] G. P. Meyer, K. C. Wollert, J. Lotz, J. Steffens, P. Lippolt, S. Fichtner, H. Hecker, A. Schaefer, L. Arseniev, B. Hertenstein, A. Ganser, and H. Drexler, "Intracoronary bone marrow cell transfer after myocardial infarction: eighteen months' follow-up data from the randomized, controlled BOOST (BOne marrOw transfer to enhance ST-elevation infarct regeneration) trial," *Circulation,* vol. 113, pp. 1287-94, Mar 14 2006.
[83] B. E. Strauer, M. Brehm, T. Zeus, M. Kostering, A. Hernandez, R. V. Sorg, G. Kogler, and P. Wernet, "Repair of infarcted myocardium by autologous intracoronary mononuclear bone marrow cell transplantation in humans," *Circulation,* vol. 106, pp. 1913-8, Oct 8 2002.
[84] A. A. Kocher, M. D. Schuster, M. J. Szabolcs, S. Takuma, D. Burkhoff, J. Wang, S. Homma, N. M. Edwards, and S. Itescu, "Neovascularization of ischemic myocardium by human bone-marrow-derived angioblasts prevents cardiomyocyte apoptosis, reduces remodeling and improves cardiac function," *Nat Med,* vol. 7, pp. 430-6, Apr 2001.
[85] R. G. Trohman, M. H. Kim, and S. L. Pinski, "Cardiac pacing: the state of the art," *Lancet,* vol. 364, pp. 1701-19, Nov 6-12 2004.
[86] M. Rivero-Ayerza, D. A. Theuns, H. M. Garcia-Garcia, E. Boersma, M. Simoons, and L. J. Jordaens, "Effects of cardiac resynchronization therapy on overall mortality and mode of death: a meta-analysis of randomized controlled trials," *Eur Heart J,* vol. 27, pp. 2682-8, Nov 2006.
[87] R. Koos, A. M. Sinha, K. Markus, O. A. Breithardt, K. Mischke, M. Zarse, M. Schmid, R. Autschbach, P. Hanrath, and C. Stellbrink, "Comparison of left ventricular lead placement via the coronary venous approach versus lateral thoracotomy in patients receiving cardiac resynchronization therapy," *Am J Cardiol,* vol. 94, pp. 59-63, Jul 1 2004.
[88] R. H. Helm, M. Byrne, P. A. Helm, S. K. Daya, N. F. Osman, R. Tunin, H. R. Halperin, R. D. Berger, D. A. Kass, and A. C. Lardo, "Three-dimensional mapping of optimal left ventricular pacing site for cardiac resynchronization," *Circulation,* vol. 115, pp. 953-61, Feb 27 2007.
[89] M. Becker, A. Franke, O. A. Breithardt, C. Ocklenburg, T. Kaminski, R. Kramann, C. Knackstedt, C. Stellbrink, P. Hanrath, P. Schauerte, and R. Hoffmann, "Impact of left ventricular lead position on the efficacy of cardiac resynchronisation therapy: a two-dimensional strain echocardiography study," *Heart,* vol. 93, pp. 1197-203, Oct 2007.
[90] C. M. van Campen, F. C. Visser, C. C. de Cock, H. S. Vos, O. Kamp, and C. A. Visser, "Comparison of the haemodynamics of different pacing sites in patients undergoing resynchronisation treatment: need for individualisation of lead localisation," *Heart,* vol. 92, pp. 1795-800, Dec 2006.
[91] T. Thom, N. Haase, W. Rosamond, V. J. Howard, J. Rumsfeld, T. Manolio, Z. J. Zheng, K. Flegal, C. O'Donnell, S. Kittner, D. Lloyd-Jones, D. C. Goff, Jr., Y. Hong, R. Adams, G. Friday, K. Furie, P. Gorelick, B. Kissela, J. Marler, J. Meigs, V. Roger, S. Sidney, P. Sorlie, J. Steinberger, S. Wasserthiel-Smoller, M. Wilson, and P. Wolf, "Heart disease and stroke statistics--2006 update: a

report from the American Heart Association Statistics Committee and Stroke Statistics Subcommittee," *Circulation,* vol. 113, pp. e85-151, Feb 14 2006.

[92] D. E. Singer, "A 60-year-old woman with atrial fibrillation," *JAMA,* vol. 290, pp. 2182-9, Oct 22 2003.

[93] V. Fuster, L. E. Ryden, D. S. Cannom, H. J. Crijns, A. B. Curtis, K. A. Ellenbogen, J. L. Halperin, J. Y. Le Heuzey, G. N. Kay, J. E. Lowe, S. B. Olsson, E. N. Prystowsky, J. L. Tamargo, S. Wann, S. C. Smith, Jr., A. K. Jacobs, C. D. Adams, J. L. Anderson, E. M. Antman, S. A. Hunt, R. Nishimura, J. P. Ornato, R. L. Page, B. Riegel, S. G. Priori, J. J. Blanc, A. Budaj, A. J. Camm, V. Dean, J. W. Deckers, C. Despres, K. Dickstein, J. Lekakis, K. McGregor, M. Metra, J. Morais, A. Osterspey, and J. L. Zamorano, "ACC/AHA/ESC 2006 Guidelines for the Management of Patients with Atrial Fibrillation: a report of the American College of Cardiology/American Heart Association Task Force on Practice Guidelines and the European Society of Cardiology Committee for Practice Guidelines (Writing Committee to Revise the 2001 Guidelines for the Management of Patients With Atrial Fibrillation): developed in collaboration with the European Heart Rhythm Association and the Heart Rhythm Society," *Circulation,* vol. 114, pp. e257-354, Aug 15 2006.

[94] E. J. Benjamin, P. A. Wolf, R. B. D'Agostino, H. Silbershatz, W. B. Kannel, and D. Levy, "Impact of atrial fibrillation on the risk of death: the Framingham Heart Study," *Circulation,* vol. 98, pp. 946-52, Sep 8 1998.

[95] K. P. Phillips, A. Natale, R. Sterba, W. I. Saliba, J. D. Burkhardt, O. Wazni, L. Liberman, and R. A. Schweikert, "Percutaneous Pericardial Instrumentation for Catheter Ablation of Focal Atrial Tachycardias Arising from the Left Atrial Appendage," *J Cardiovasc Electrophysiol,* Nov 20 2007.

[96] P. Maury, B. Leobon, A. Duparc, M. Delay, and M. Galinier, "Epicardial catheter ablation of ventricular tachycardia using surgical subxyphoid approach," *Europace,* vol. 9, pp. 212-5, Apr 2007.

[97] A. P. Mannam, K. K. Ho, D. E. Cultip, J. P. Carrozza, D. J. Cohen, B. H. Lorell, and R. J. Laham, "Safety of subxyphoid pericardial access using a blunt-tip needle," *Am J Cardiol,* vol. 89, pp. 891-3, Apr 1 2002.

[98] N. Becit, Y. Unlu, M. Ceviz, C. U. Kocogullari, H. Kocak, and Y. Gurlertop, "Subxiphoid pericardiostomy in the management of pericardial effusions: case series analysis of 368 patients," *Heart,* vol. 91, pp. 785-90, Jun 2005.

[99] J. E. Molina and D. G. Benditt, "An epicardial subxiphoid implantable defibrillator lead: superior effectiveness after failure of standard implants," *Pacing Clin Electrophysiol,* vol. 27, pp. 1500-6, Nov 2004.

[100] J. W. Kirklin and N. T. Kouchoukos, *Kirklin/Barratt-Boyes cardiac surgery : morphology, diagnostic criteria, natural history, techniques, results, and indications*, 3rd ed. Philadelphia, Pa.: Churchill Livingstone, 2003.

[101] N. A. Patronik, "Development and preliminary testing of a mobile robot for cardiac intervention," *Master's Thesis, Tech. Report CMU-RI-TR-05-08, Robotics Institute, Carnegie Mellon University,* February 2005 2005.

[102] A. K. Geim, S. V. Dubonos, G. I.V., K. S. Novoselov, A. V. Zhokov, and S. Y. Shapoval, "Microfabricated adhesive mimicking gecko foot-hair," *Nature Materials,* vol. 2, pp. 461-463, 2003.

[103] N. A. Patronik, T. Ota, M. A. Zenati, and C. N. Riviere, "Improved traction for a mobile robot traveling on the heart," *Conf Proc IEEE Eng Med Biol Soc,* vol. 1, pp. 339-42, 2006.

[104] N. A. Patronik, M. A. Zenati, and C. N. Riviere, "A miniature cable-driven robot for crawling on the heart," *Conf Proc IEEE Eng Med Biol Soc,* vol. 6, pp. 5771-4, 2005.

[105] I. A. Gravagne, C. D. Rahn, and I. D. Walker, "Large deflection dynamics and control for planar continuum robots," *IEEE/ASME transactions on mechatronics : a joint publication of the IEEE Industrial Electronics Society and the ASME Dynamic Systems and Control Division,* vol. 8, p. 299, 2003 2003.

[106] J. Lessick, S. Sideman, H. Azhari, E. Shapiro, J. L. Weiss, and R. Beyar, "Evaluation of regional load in acute ischemia by three-dimensional curvatures analysis of the left ventricle," *Ann Biomed Eng,* vol. 21, pp. 147-61, Mar-Apr 1993.

[107] M. Schneider and C. Stevens, "Development and testing of a new magnetic-tracking device for image guidance," *Proceedings of SPIE Medical Imaging 2007: Visualization and Image-Guided Procedures,* vol. 6505, p. 65090I, 2007.

[108] T. D. Soper, D. R. Haynor, R. W. Glenny, and E. J. Seibel, "A model of respiratory airway motion for real-time tracking of an ultrathin bronchoscope," *Proceedings of SPIE Medical Imaging 2007: Physiology, Function, and Structure from Medical Images,* vol. 6511, p. 65110M, 2007.

[109] R. S. Estepar, N. Stylopoulos, R. Ellis, E. Samset, C. F. Westin, C. Thompson, and K. Vosburgh, "Towards scarless surgery: An endoscopic ultrasound navigation system for transgastric access procedures," *Comput Aided Surg,* vol. 12, pp. 311-24, Nov 2007.

[110] Y. Sun, S. Kadoury, Y. Li, M. John, J. Resnick, G. Plambeck, R. Liao, F. Sauer, and C. Xu, "Image guidance of intracardiac ultrasound with fusion of pre-operative images," *Med Image Comput Comput Assist Interv Int Conf Med Image Comput Comput Assist Interv,* vol. 10, pp. 60-7, 2007.

[111] T. A. J. Vassiliades, M. E. McConnell, and W. M. Book, "Thorascopic Approach to Epicardial Lead Implantation in Adult Patients with previous Congenital Cardiac Surgery," *9th Annual Meeting for the International Society for Minimally Invasive Cardiothoracic Surgery,* June 7-10 2006 2006.

[112] R. C. Coulter, "Implementation of the pure pursuit path tracking algorithm," *Technical Report CMU-RI-TR-92-01, Robotics Institute, Carnegie Mellon University,* 1992.

[113] O. Amidi, " Integrated mobile robot control," *Technical Report CMU-RI-TR-90-17, Robotics Institute, Carnegie Mellon University,* 1990.

[114] A. Ollero and O. Amidi, "Predictive path tracking of mobile robots," *Proceedings of 5th International Conference on Advanced Robotics, Robots in Unstructured Environments (ICAR '91),* vol. 2, pp. 1081-1086, 1991.

[115] A. Kelly, "A feedforward control approach to the local navigation problem for autonomous vehicles," *Technical Report CMU-RI-TR-94-17, Robotics Institute, Carnegie Mellon University,* 1994.

[116] R. Shabetai, *The pericardium*, [2nd ed. Boston: Kluwer Academic Publishers, 2003.

[117] S. J. Crick, M. N. Sheppard, S. Y. Ho, L. Gebstein, and R. H. Anderson, "Anatomy of the pig heart: comparisons with normal human cardiac structure," *J Anat,* vol. 193 (Pt 1), pp. 105-19, Jul 1998.